THÈSE

Pour obtenir le grade de

DOCTEUR DE L'UNIVERSITÉ GRENOBLE ALPES

École doctorale : I-MEP2 - Ingénierie - Matériaux, Mécanique, Environnement, Energétique, Procédés, Production
Spécialité : MEP : Mécanique des fluides Energétique, Procédés
Unité de recherche : Laboratoire de Physique Subatomique et Cosmologie

SIBYL : Incertitudes en évolution

SIBYL - Scaling Incertitudes BY modeLing

Présentée par :

Davide PORTINARI

Direction de thèse :

Adrien BIDAUD Maitre de Conférences, Université Grenoble Alpes	Directeur de thèse

Rapporteurs :

Sandra DULLA
PROFESSEUR, Politecnico di Torino
Luiz LEAL
INGENIEUR HDR, INSTITUT RADIOPROTECT SURETE NUCLEAIRE

Thèse soutenue publiquement le **23 septembre 2022**, devant le jury composé de :

Adrien BIDAUD PROFESSEUR DES UNIVERSITES, Grenoble INP	Directeur de thèse
Sandra DULLA PROFESSEUR, Politecnico di Torino	Rapporteure
Luiz LEAL INGENIEUR HDR, INSTITUT RADIOPROTECT SURETE NUCLEAIRE	Rapporteur
Pablo RUBIOLO PROFESSEUR DES UNIVERSITES, Grenoble INP	Examinateur
Guy MARLOT PROFESSEUR EMERITE, Polytechnique de Montréal	Examinateur

Invités :

Yoann Calzavara
DOCTEUR EN SCIENCES, ILL
Laurent Chabert
INGENIEUR DOCTEUR, Technicatome

Abstract

The PhD project SIBYL (Scaling Incertitudes BY modeLLing) has the purpose of merging the advances in reactor physics coming from Generalized Perturbation Theory (GPT) with the current conversion efforts taking place at the RHF (High Flux Reactor), for a new LEU (Low Enriched Uranium) fuel element. Perturbation Theory is a powerful mathematical method developed around some nominal configuration, in order to find approximate solutions for the model once its parameters are changed around their nominal values. The ultimate goal of Generalized Perturbation Theory (GPT) is the definition of sensitivity coefficients, allowing for the quantification of relevant uncertainties, without running multiple perturbed calculations. In Monte Carlo codes especially, the time needed for multiple modelling and multiple calculations can quickly become prohibitive, and a very relevant stochastic implementation of GPT to the code SERPENT has been developed in 2015. This work is focused on Depletion Perturbation Theory (DPT), a specific branch of GPT, that allows for the estimation of sensitivity coefficients all along the fuel cycle, meaning that the effect of a perturbation at day 0 (e.g. burnable poison density) can be quantified on some end of life relevant parameter (k, nuclide density). A simplified model of the RHF has been built in order to assess the performance of DPT in an environment that would be fast and intuitive. Uncertainty analysis on multiplication factor and Pu-239 density sensitivities has shown that the LEU conversion will not affect the safety margins.

Résumé

Le projet de thèse SIBYL (Scaling Incertitudes BY modeling) a pour objectif de fusionner les avancées de la physique des réacteurs issues de la Théorie Généralisée des Perturbations (GPT [1]) avec les efforts de conversion en cours au RHF (High Flux Reactor), pour un nouvel élément combustible LEU (Low Enriched Uranium). La théorie des perturbations est une méthode mathématique puissante développée autour d'une configuration nominale, afin de trouver des solutions approximatives pour le modèle une fois que ses paramètres sont modifiés autour de leurs valeurs nominales. Le but ultime de la théorie généralisée des perturbations (GPT) est la définition des coefficients de sensibilité, c'est-à-dire des dérivées normalisées de certaines sorties du modèle par rapport à un paramètre d'entrée, permettant la quantification des incertitudes pertinentes, sans exécuter de multiples calculs perturbés. Dans les codes Monte Carlo notamment, le temps nécessaire à la modélisation multiple et aux calculs multiples peut vite devenir prohibitif, et une implémentation stochastique très efficace de GPT au code SERPENT a été développée en 2015 [2]. Ce travail est axé sur la théorie de la perturbation en evolution [3] [4], une branche spécifique de la GPT, qui permet l'estimation des coefficients de sensibilité tout au long du cycle du combustible, ce qui signifie que l'effet d'une perturbation en debut de vie (BOL), par ex. densité de poison consommable peut être quantifiée sur certains paramètres pertinents en fin de vie (EOL) tels que le facteur de multiplication ou la densité de plutonium. Un modèle simplifié du RHF a été construit afin d'évaluer les performances de la DPT dans un environnement

qui serait rapide et intuitif. L'analyse d'incertitude sur le facteur de multiplicationet les sensibilités à la densité de Pu-239 ont montré que la conversion LEU n'ira pas affecter les marges de sureté.

0.1 Conversion

Le RHF (High Flux Reactor), avec l'ATR du Idaho National Laboratory, fournit le flux de neutrons thermiques le plus intense au monde [5]. Ce flux très intense est produit dans un coeur compact plongé dans un très grand volume d'eau lourde, dont les neutrons sont extraits du réflecteur par 17 tubes faisceaux (Fig. 1, partie gauche). Le réflecteur fournit également la majeure partie de la modération, puisque l'élément combustible lui-même est largement sous-modéré. L'élément combustible comprend un total de 280 plaques combustibles en forme de développante de cercle (Figure 1, côté droit). Cela maximise les fuites de neutrons de l'élément, mais impose également un débit massique très élevé entre les plaques pour refroidir le combustible. Cette densité de puissance élevée, associée aux très petits diamètres hydrauliques des 280 canaux de refroidissement étroits, explique une perte de charge de 10 bars sur seulement 1 mètre de surface chauffée.

Dans le cadre de la conversion en uranium faiblement enrichi, la perte d'enrichissement fissile a été compensée par une augmentation de la densité du combustible (composé (U_3Si_2) et par une augmentation du volume de combustible à l'intérieur des plaques (longueur, largeur et épaisseur). D'autre part, l'augmentation de la matière fertile entraîne une accumulation de Plutonium en fin de cycle, et la nécessité d'évaluer les incertitudes associées. De plus, l'augmentation du volume de combustible dans la conception ne laisse plus de place pour un poison consommable aux extrémités de telles plaques. Dans la configuration HEU du réacteur à haut flux, le poison de bore joue un rôle très important dans l'extinction du pic de puissance aux coins supérieur et inférieur des plaques (Figure 1, côté gauche). Ce pic de puissance est principalement dû à l'effet d'auto-protection de l'élément com-

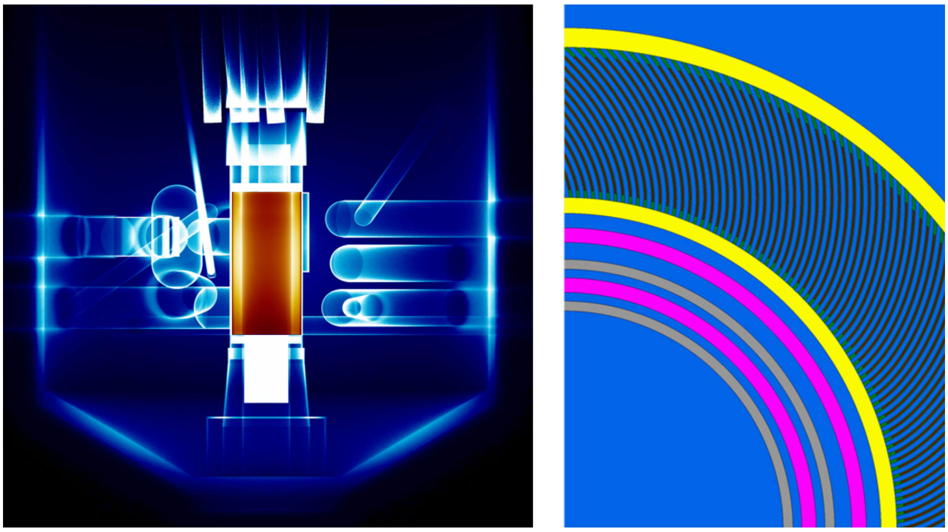

Figure 1: Diagramme des réactions d'absorption RHF (à gauche) et détail du coeur dans SERPENT (à droite)

PUISSANCE	58.35 MWth
COMBUSTIBLE	93% enrichi, U-Al mix
COEUR	element annulaire, 280 plaques
REFLECTEUR	Eau lourde (300K, 4 bar)
REFRIGERANT	Eau lourde (290K, 14 bar)
POISON BRULABLE	Bore aux extrémités de l'element
PILOTAGE	1 barre, dans l'element (Figure 1, en rose)
SHUTDOWN	5 barre, autour de l'element
FLUX	$1.5 \cdot 10^{15} \frac{n}{cm^2 s}$

Table 1: Caractéristiques du RHF

bustible vis-à-vis des neutrons qui ne reviennent au combustible qu'après avoir été modérés dans le réflecteur. Étant donné que l'eau de refroidissement s'écoule vers le bas dans l'élément et entre les plaques de combustible, la plus petite marge d'ébullition nucléée se situe dans la partie inférieure de l'élément, tandis que le pic d'irradiation se situe au sommet de l'élément, justifiant le besoin de poison consommable à la fois au-dessus et au-dessous de l'élément. La solution proposée pour la configuration LEU, place le poison consommable à l'intérieur du tube structurel qui entoure les plaques, formant une ceinture de bore autour et à l'extérieur du canal central (Figure 2, côté droit). De cette façon, le pic de puissance est maîtrisé, mais n'est pas complètement supprimé, comme c'était le cas pour le cas HEU. Le concept de ceinture de bore est donc un exemple de paramètre crucial dans la démarche d'optimisation, devant assurer une marge de sureté en maintenant le pic de puissance en dessous d'une certaine limite, tout en répondant à des critères de neutronique, d'irradiation et de fabrication.

Les procédures d'autorisation standard, requises pour la conversion LEU, impliquent l'utilisation de codes de Monte Carlo pour effectuer de nombreux calculs directs (pour les paramètres neutroniques, le flux de chaleur, les incertitudes, la criticité, la valeur de réactivité. . .) et les calculs d'évolution couplés (densités d'actinides, chaleur de décroissance . . .). Il est clair cependant que certains aspects clés, comme les performances de la ceinture de bore, ont un impact à la fois dans la phase d'optimisation et dans la phase de licence. Par conséquent, le besoin d'un outil qui serait en mesure de fournir des informations utiles sur la sensibilité des paramètres nucléaires aux choix de conception, sans la charge d'effectuer en continu les calculs du rapport de suretè, qui pourraient prendre jusqu'à plusieurs semaines de calcul.

0.2 SIBYL

Un modèle déterministe du RHF a été mis en place et appelé SIBYL, il implique une région homogène de matière fissile, une région de réflecteur et

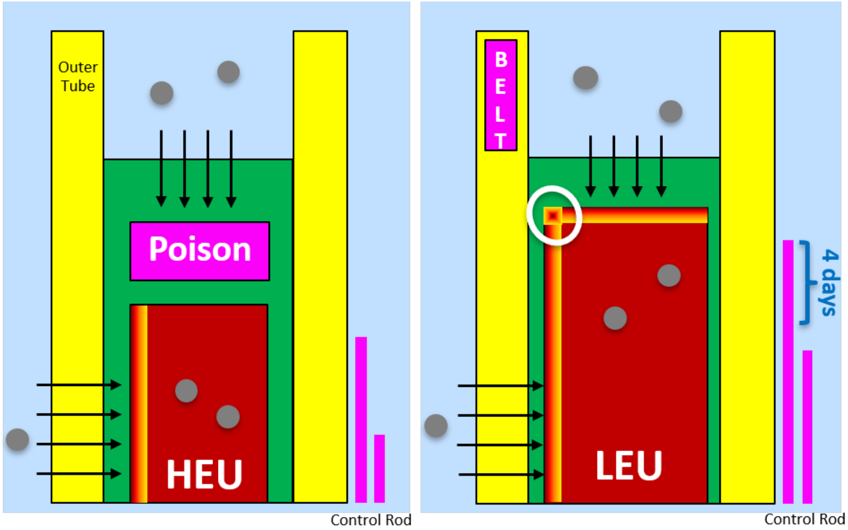

Figure 2: Configurations des plaques de combustible HEU et LEU (le point chaud LEU est encerclé en blanc)

une région de modérateur, où une densité réglable de matériau de barre de commande (Nickel) pourrait entraîner la criticité et permettre un k- reset (réactivité constante). Il comprend 44 groupes énergétiques, 3 régions cylindriques et la carte complète des produits de fission et des actinides. Cette approximation du modèle à 3 régions permet une définition aisée des quantités globales, tout en préservant l'hétérogénéité du modèle. Il peut être très utile pour des applications telles que le réacteur à haut flux, qui comprend des barres de commande et des poisons consommables séparés de la région du combustible. Certains résultats des calculs couplés de Boltzmann-Bateman sont présentés dans la Figure 3. Une description plus détaillée des équations et des hypothèses sous-jacentes à SIBYL est donnée dans le chapitre 3. Contrairement à la version LWR de SIBYL, la région cylindrique interne RHF est occupée par la barre de commande, tandis que les plaques de combustible occupent la deuxième couche (Figure 1, côté droit).

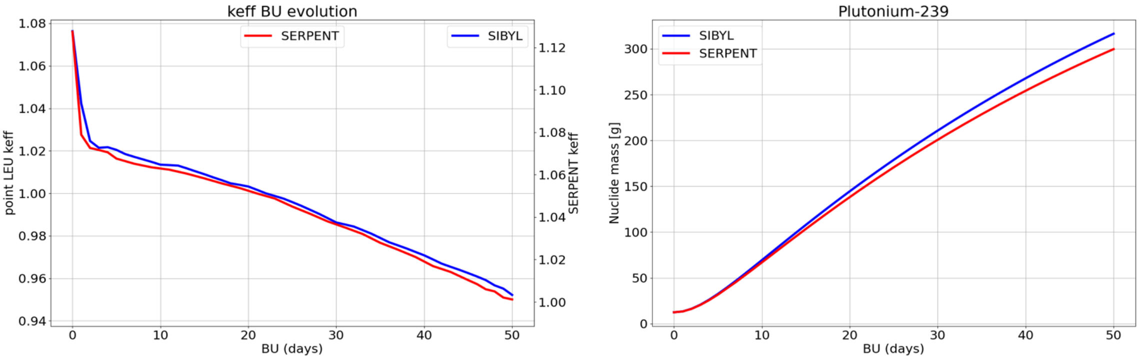

Figure 3: Comparaison des résultats de SIBYL avec SERPENT pour le RHF

0.3 PTERODAx

L’architecture python est illustrée à la Figure 4 : le modèle SERPENT fournit les données nucléaires nécessaires à SIBYL, tandis que l’équation de Bateman est traitée par SALAMECHE [6], une sous-routine du package python open source ONIX. Cette configuration fournit un solveur simplifié mais précis pour l’évolution du combustible, dont le temps de calcul est beaucoup plus court que Monte Carlo, ce qui le rend idéal pour apprendre les rouages de la DPT, qui est résolu dans PTERODAx (Perturbation Theory Engine for Reactor Outputs Depletion Analysis). Les résultats recueillis à partir de plusieurs calculs SIBYL sur la valeur finale de k et de masse de plutonium sont comparés aux exécutions nominales uniques de PTERODAx. L’algorithme de résolution de la théorie des perturbations en evolution (DPT) dans PTERODAx consiste à écrire une équation adjointe en evolution pour le champ de nucléides N^* ainsi que l’équation de transport adjointe plus connue pour Φ^*, en partant de la solution de transport à EOL et en remontant dans le temps pour obtenir la solution perturbée (en remontant le temps avec le même package SALAMECHE). Si la densité finale de Pu-239 est considérée comme une réponse, alors $N_x^*(t)$ représente la probabilité qu’un certain nucléide x au temps t "devienne" Pu-239 à EOL, un peu comme $\Phi^*(E, r)$ peut rendre compte de la probabilité qu’un neutron, à l’énergie E

et à la position r, contribue à un certain comptage du détecteur avant de disparaître. Dans cet exemple, la condition finale pour l'équation adjointe de Bateman sera en fait $N^*_x(t = t_f) = 0$, sauf pour $N^*_{Pu_{239}}(t = t_f) = 1$.

Le cadre théorique conçu par Williams suit une approche variationnelle [3], où de nombreuses contraintes sont imposées sur les quantités adjointes, telles que : normalisation du flux à la contrainte de puissance P^*, solution particulière pour le flux de transport adjoint Γ^* à ajouter au flux adjoint homogène Φ^*, orthogonalité entre Γ^* et la source de fission, etc. Les coefficients de sensibilité DPT, obtenus en fonction de ces quantités adjointes, comprennent différentes contributions directes et indirectes, fournissant un aperçu physique puissant sur les perturbations elles-mêmes. Sans revenir sur toute la théorie, il est encore possible de décomposer les sensibilités en trois termes de Williams [3] :

$$S_\alpha = \sum_i \left(\int_{t_i}^{t_{i+1}} \underbrace{\boldsymbol{N}_i^* \frac{\partial(\boldsymbol{M}_i \boldsymbol{N}_i)}{\partial\alpha}}_{\text{at. evolution}} dt - \underbrace{< \Gamma_i^* | \frac{\partial B_i}{\partial\alpha}\psi_i >}_{\text{flux spectrum}} - \underbrace{< P_i^* | \frac{\partial(\boldsymbol{\sigma}_f \boldsymbol{N}_i)}{\partial\alpha}\phi_i >}_{\text{power level}} \right) \tag{1}$$

• Évolution isotopique : explique la transmutation directe par absorption en Pu-239. La dérivée de l'opérateur de Bateman par rapport au paramètre perturbé est pondérée par N^*.

• Spectre de flux : tient compte des effets indirects sur la forme et le spectre du flux (par exemple, le durcissement), qui ont un impact sur la génération et la disparition de Pu. La dérivée de l'opérateur de Boltzmann par rapport au paramètre perturbé est pondérée par Γ^*.

• Niveau de puissance : tient compte des effets indirects sur la normalisation du flux, selon la contrainte de puissance P^*, qui impactent la génération et la disparition de Pu. La Figure 5 montre la précision de ces coefficients et les décompose en différentes contributions. Une perturbation de 1% de la densité de l'U-235 ou de l'U-238 dans le combustible neuf a différentes manières d'affecter la densité du Pu-239 dans le combustible usé

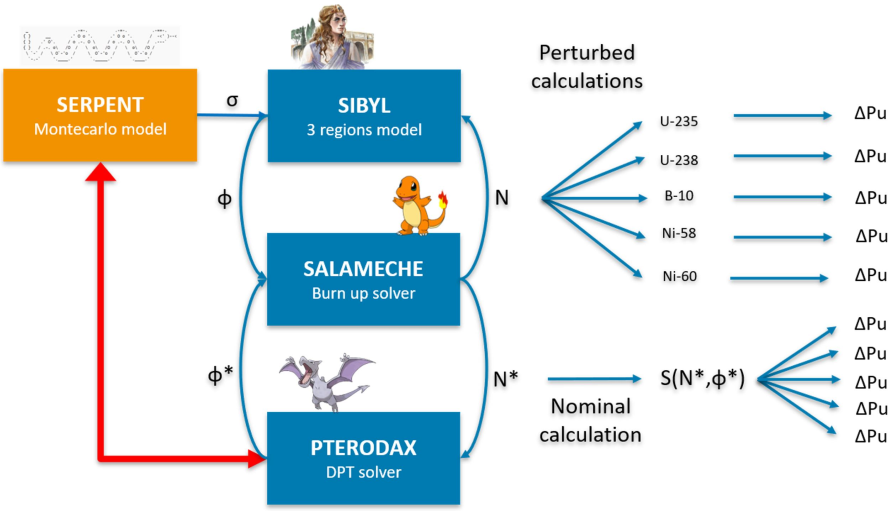

Figure 4: Python architecture

EOL. La barre rouge fait référence aux résultats directs obtenus à partir de différents calculs SIBYL perturbés, tandis que la barre bleue fait référence à l'estimation PTERODAx (sensibilité multipliée par la perturbation de densité relative). Les trois barres colorées restantes représentent les différents contributeurs dans l'éq. 1. L'U-238 a une contribution prépondérante à l'évolution (en vert), puisqu'il peut se transmuter directement en Pu-239 en absorbant un neutron. L'U-235, en revanche, ne peut pas se transmuter directement en Pu-239 et ne contribuera qu'indirectement à la génération de Pu. Par exemple, une augmentation de 1% de la masse de l'U-235 augmentera k, améliorant l'économie de neutrons et entraînant une diminution du flux total pour la même puissance totale fixe, ce qui fait que l'U-238 absorbe moins de neutrons en raison du flux plus faible . C'est pourquoi la barre brune apporte une contribution négative à la sensibilité du Pu à l'U-235. D'autre part, une augmentation de 1% de la masse d'U-235 augmentera également les absorptions thermiques. Par consequence, il y aura un léger décalage du spectre de flux vers la région épithermale, où la section efficace de capture de l'U-238 est plus élevée et moins en concurrence avec les absorptions de l'U-235. Puisque les principaux isotopes perturbés sont tous des absorbeurs

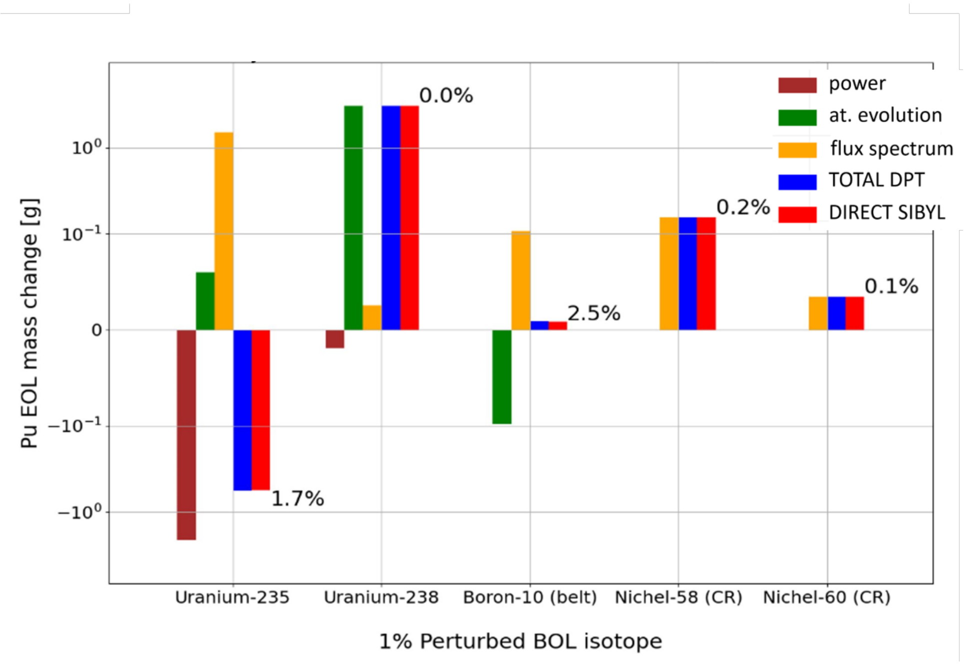

Figure 5: Résultats PTERODAx pour la sensibilité de la masse EOL Pu-239 à différentes perturbations en debut de vie, comparés aux calculs directs SIBYL (l’erreur relative est rapportée en haut des histogrammes)

thermiques, ils ont des contributions indirectes similaires à la forme et au spectre du flux (barres orange positives). La compensation des effets, qui a lieu pour U-235 et B-10, souligne l’importance de cet outil. De plus, la raison pour laquelle certains isotopes ont une "contribution à l’évolution isotopique" pertinente, alors qu’il leur est impossible de se transmuter directement en Pu, réside dans l’algorithme DPT. L’évolution isotopique adjointe N^* est en fait mise à jour à chaque pas de temps de Bateman par PTERODAx, afin de prendre en compte les contributions indirectes. Cette contribution fictive à l’évolution isotopique explique finalement l’épuisement de l’isotope perturbé lors de la combustion. Alors que cela est détecTable pour l’U-235, il est prédominant pour le B-10, qui a une disparition par capture de 100%. En effet, comme cela a été mentionné dans la section 2, la densité de poison consommable a été optimisée afin de reduire le point chaud en début de vie, tout

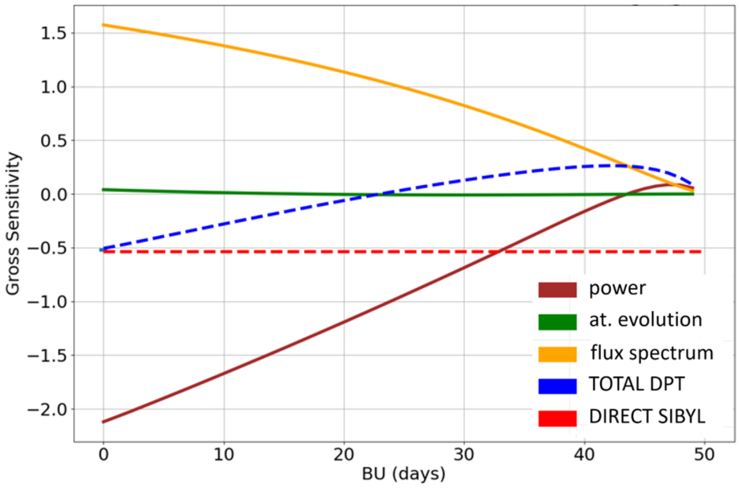

Figure 6: Évolution de la sensibilité de PTERODAx à différents points de combustion pour une réponse EOL de densité de Pu-239 à une perturbation BOL de la densité de U-235.

en minimisant l'impact sur la valeur de réactivité de l'élément combustible et la durée du cycle du réacteur.

Enfin, l'évolution des coefficients de sensibilité du Pu-239 avec le temps est représentée sur la Figure 6 pour une perturbation en U-235. La condition finale fixe N^{*}=0 et avec elle la sensibilité totale. Ensuite, l'équation adjointe de Bateman est résolue et les contributions indirectes empilent les différents termes, y compris celui d'évolution isotopique. Les valeurs au jour 0 sont celles indiquées sur la Figure 5, reliant une perturbation BOL à une sortie EOL telle que la densité de Pu. La ligne rouge "pert" fait référence au calcul SIBYL perturbé.

PTERODAx est également capable d'estimer les sensibilités de k. Ces coefficients peuvent fournir des informations importantes sur la valeur de la réactivité des éléments combustibles et permettre le reset de k dans l'algorithme de PTERODAx. Cela se fait en comparant la contribution de la réactivité de chaque nucléide au poids de la barre de contrôle tout au long du cycle.

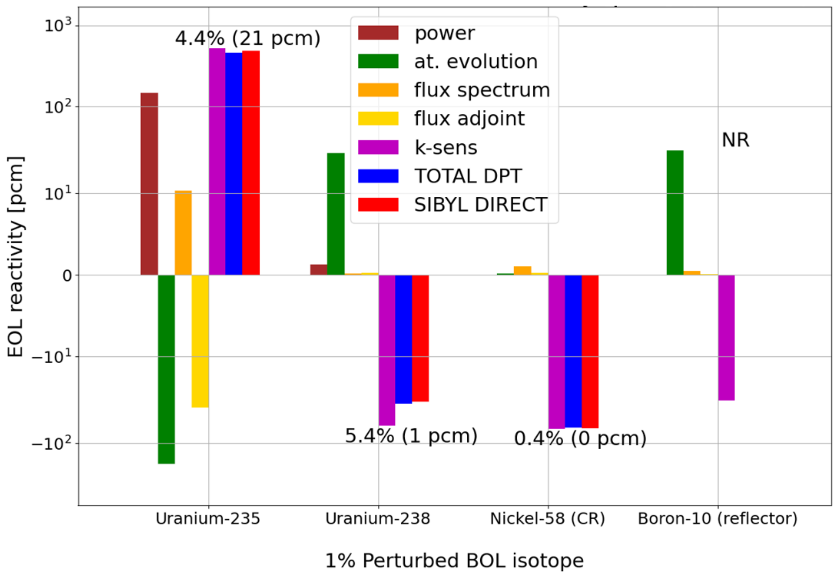

Figure 7: PTERODAx results for EOL k sensitivity to different BOL perturbations, compared with SIBYL direct calculations (the relative error is reported on top of the histograms)

Les résultats de sensibilité k sont présentés sur la Figure 7 : la définition bilinéaire du facteur de multiplication apporte une contribution supplémentaire "spectre de flux adjoint" (barre jaune) à la sensibilité totale. La sensibilité S_k de chaque nucléide en fin de cycle (barre violette) est souvent le principal contributeur à la sensibilité totale. En effet, pour une réponse en facteur de multiplication, la condition finale sur le champ de nucléide adjoint est $N^* = S_k$. Alors que les perturbations B-10 ont eu un faible impact sur la masse EOL Pu-239, l'impact sur EOL k est nul. En effet, même si le bore est complètement brûlé à EOL, le retard de production de Pu causé par la désintégration du Np-239 provoque un effet "backlog" de quelques jours, ce qui n'est pas vrai pour la reactivité.

0.4 Conclusions

La théorie des perturbations en evolution, telle qu'implémentée dans PTERODAx, s'est avérée très précise dans l'estimation des sensibilités à la densité des nucléides. Cette capacité est très certainement enrichie par les informations physiques que ces coefficients peuvent fournir sur les contributeurs physiques à la sortie souhaitée. Cela permets d'élargir l'application de l'analyse de sensibilité de la propagation de l'incertitude à l'optimisation et au raffinement de la conception. Un autre implementation important réside dans la mise en œuvre de k-reset (réactivité constante) au sein de l'algorithme d'evolution, une manière plus standard de faire fonctionner les réacteurs qui mets également en évidence les effets couplés d'evolution et de réactivité, et qui est presenté dans le manuscrit.

List of symbols

Σ	Macroscopic cross section ($\frac{1}{cm}$)
Φ	Direct neutron flux ($\frac{n}{cm^2 s}$)
$\Phi^\dagger$	Adjoint neutron flux (-)
$\hat{B}$	Boltzmann operator
$\hat{B}^\dagger$	Adjoint Boltzmann operator
$\hat{M}$	Bateman operator
f	Transfer function
χ	Neutron emission spectrum
ν	Average number of emitted neutrons (-)
m	Majorant factor (-)
k_{eff}	Effective multiplication factor (-)
λ_{eff}	Effective neutron lifetime (μs)
β_{eff}	Effective delayed neutron fraction (-)
α_v	Void coefficient ($\frac{pcm}{cm^3}$)
α	Present neutron generation (-)
λ	Number of ancestor latent generations (-)
γ	Number of daughter latent generations (-)
ϵ	Number of total geneations (-)
x, α	Generic parameters
S_x^y	Sensitivity of parameter y to a change in x (-)

List of subscripts:

f	Fission
s	Scattering
a	Absorption

List of Figures

List of Tables

Contents

Chapter 1

Introduction

The unseen enemy is always the most fearsome. [7]

In the last decades, scientific computing has become increasingly important in forecasting the behavior of natural phenomena and artificial systems. Scientific computations are frequently built on mathematical models in the form of coupled nonlinear partial differential equations. While advancing dramatically over the years, there is often a gap between these simulations and real-world applications. Even though most simulations are deterministic, engineering applications are fraught with uncertainty due to a variety of factors. As outlined in reference [8], among these factors are often the manufacturing process, materials variability, initial conditions, mechanical wear or damage, and the system's surroundings. Furthermore, due to the model's assumptions as well as the numerical approximations used in simulations, the modelling process itself can introduce a certain amount of uncertainty.

Model validation is usually used to handle the most physical uncertainties, by comparing simulation results to experimental benchmarks, while the verification of code solutions' convergence and stability is used to address the numerical uncertainties. In order to assess the overall uncertainty in a simulation, each of these distinct sources of uncertainty must be calculated and incorporated. Furthermore, knowing the causes of uncertainty is crucial to Figure out how to decrease and manage uncertainty in the most efficient and cost-effective way possible.

1.1 Uncertainty Analysis

Uncertainty analysis gives a quantitative approximation of the range of model outputs produced by model structure or input uncertainty. If the analysis is conducted properly, the probability that this range contains the real value (or values) that the model is attempting to forecast is high. Furthermore, the study can be extended to identify the causes of the majority of the overall uncertainty, so that priorities can be identified in order to reduce the uncertainty. As a result of these considerations, uncertainty analysis is an inherent and critical component of the modelling phase. However, if the uncertainty estimates are to be relevant and useful, they must be conducted in a systematic manner, taking into account the model's goal, the quality of the data, and the application's nature. In this context, the analysis's methodologies and assumptions must be transparently documented.

The two most traditional approaches to uncertainty analysis are analytical [9], [10] and statistical (Monte Carlo) sampling methods [11]. They can both be applied directly to models or combined with other approaches such as response surface replacement and differential analysis [9], [12]). It can be said that the Monte Carlo method is the most versatile and universally applicable, while the analytical methods can be exploited for specific applications.

1.1.1 IAEA guidelines

Uncertainty in model predictions can arise from a number of sources, including specification of the problem, formulation of the conceptual or the computational model, estimation of parameter values, calculation, interpretation and documentation of results. Of these sources, only uncertainties due to estimation of parameter values can be quantified in a straightforward way.

The main steps in a parameter uncertainty analysis are:

i) Identify the parameters that could contribute significantly to the uncertainty in the final model prediction. Care should be exercised here not to discard potentially significant uncertainties without good cause.

ii) For each parameter, assess the tolerance on the input value. Either by its standard deviation, or by producing a full probability density function, in case Monte Carlo propagation is envisaged.

iii) Account for dependencies (correlations) among the parameters.

iv) Propagate the uncertainties through the model to generate a probability density function (PDF) of predicted values.

v) Derive confidence limits and intervals from the PDF of predicted values to provide a quantitative statement about the effect of parameter uncertainty on the model prediction.

Uncertainty should be considered at the beginning of a consequence assessment, when the model is first chosen or developed for the problem in question. It is then possible to match the form of the uncertainty analysis to the answer that the model seeks to address, and to the available data.

Sources of uncertainty

By following the standard thought process behind the conception, and then creation, of a mathematical model, the principal factors affecting the reliability of results from environmental transfer models can be arranged into the following classes:

(1) Specification of the problem and definition of the scenario.

(2) Formulation of the conceptual model.

(3) Formulation of the mathematical model.

(4) Estimation of parameter values.

(5) Formulation of the computer code, and calculation and documentation of results.

Sources (2) and (3) are often called "model structure" uncertainties.

Sensitivity analysis

A common application of uncertainty analysis is to rank model parameters based on their contribution to the overall uncertainty in the model prediction. Once this ranking has been established, it may be used to determine how best to invest more research resources toward reducing overall uncertainty. The uncertainty evaluations of environmental models frequently reveal that a small number of parameters account for the vast majority of variance in model output.

One method of ranking the parameters is to run a series of Monte Carlo simulations where the single parameters get changed one after another, repeating the procedure for all parameters in succession. To determine the ranking, the reduction in the uncertainty of the predictions made by these runs gets compared to the scenario where all parameters were altered. Despite the fact that it is straightforward in principle, this method can be time-consuming and expensive when dealing with increasingly complex models. As a result, methods that allow for ranking without a significant number of Monte Carlo simulations are desired. The achievement of this goal can be accomplished in a variety of ways, depending on the type of model and its level of complexity. A sensitivity analysis can be performed either within the context of classical sensitivity analysis or by employing statistical techniques such as correlation and regression, as well as associated sensitivity measures.

Sensitivity analysis consists in adjusting selected input parameters one at a time over a specified range and noting the changes in model predictions that result as a consequence in input parameters. The critical model parameters are the parameters that cause the greatest relative changes in the predictions, as determined by the regression analysis. Depending on the amount and direction of the fluctuation in the given input parameters, the outcome may be very dependent on the perturbation. In addition to its local nature, the sensitivity approach has the limitation of only being able to calculate sensitivity coefficients at a single location in the parameter space given by the set of nominal (or best estimate) values for the parameters. In fact, if considerable changes in the input parameters are to be handled [9], it is necessary to evaluate sensitivity functions for numerous sets of input parameter values, resulting in additional processing cost.

Since differential sensitivity analysis is dependent on deterministic approaches, it is mostly adequate to mathematical models with mostly linear behavior, such as reactor physics and neutronics. While a statistical technique, such as Monte Carlo, that makes use of the information obtained during the propagation of parameter uncertainties, is the only choice when little or no analytical framework is applicable (for example in thermal-hydraulics). When a statistical study of the link between the values of the input parameters that have been chosen and the values of the model predictions is performed, it provides measures of sensitivity in the form of correlation and regression coefficients between input and output parameters.

1.1.2 French regulatory framework

Among the French regulatory archives provided by the "Autorité de Sûreté Nucléaire" (ASN), Guide 28, addresses the necessary procedure for conceiving a trustworthy computational tool. Inside this guide, chapter 3.4 provides the relevant information for uncertainty quantification in scientific computing tools (OCS):

"The validation should allow, by comparing the results provided by the OCS with those of the case of validation, the assessment of the various uncertainties:

- uncertainties resulting from the validation with separate effects, associated with each physical model elementary;

- uncertainties resulting from the full validation, associated with the prediction by the OCS of the quantities of interest.

The assessment of the uncertainties resulting from the full validation should take into account, if possible, the uncertainties of the elementary physical models resulting from the validation calculations. In order to limit error compensation as much as possible, the different effects on model outputs should be separated during the process. For cases where it would not be possible to compare the results provided with experimental results or results obtained using reference OCS, **the evaluation of uncertainties may, be based on comparisons with other OCSs, on expert judgments as well as sensitivity studies, as long as an appropriate justification is provided**.

Finally, the methods for quantifying the various uncertainties must be described and justified. When the determination of the various uncertainties proves to be particularly complex, an alternative approach called "conservative" can be used: this approach consists in showing that the application of conservative hypotheses (on the initial or boundary conditions, or even on the the physical models) makes it possible to obtain a conservative value of the quantities of interest of the cases of validation."

Uncertainties by design

In nuclear reactor physics, uncertainty analysis used to be carried out a posteriori, as the sensitivities of the main parameters to possible perturbations were assessed after the main calculations. Nevertheless, being sensitivities and uncertainties a key point of the engineering optimization procedure, it is fair to assume that their impact should be included in the project phase, leading to a new approach to reactor design. The field of applications for Monte Carlo neutron transport codes (section 2.2) is growing constantly. Their capacity to simulate virtually any geometry in continuous energy mode are less and less constrained by the statistical uncertainties of their outputs. This is possible thanks to the reduction of computing costs and the developments in implicit transport. New paths of discovery have been recently opened after the inclusion of perturbation theory in Monte Carlo Codes [2] [13] [14].

1.1.3 Perturbation Theory

Perturbation theory was first conceived in the XVIIIth century in order to extend the validity of Newton's gravitational law to three planets systems. Passing through the minds of Lagrange and Laplace to Paul Dirac and "Fermi's Golden Rule", it finally landed in reactor physics as well. During the well known 1955 "Atoms for peace" conference in Geneva, nuclear physicists from all over the world shared their knowledge on reactor physics for the very first time after World War II. Apparently, one of the pieces of information that was exchanged during that conference was the conventional perturbation theory of reactivity changes derived by Usachev. This, along with the work of H.Brooks [15], led to the deterministic definition of k_{eff} sensitivity coefficients, reported in section 2.1.2, and was later generalized by Gandini in 1967 for bi-linear functionals like β_{eff} and λ_{eff} [1]. This allowed to explicitly link the variation of any parameter to a change of the operator that defines them. A practical application of this technique, has been the development of an innovative nuclear data assimilation method in the framework of the prediction of the critical mass of Superphenix [16], the fast reactor experiment that took place in France in the '70s and '80s. Subsequently, "equivalent generalized perturbation theory" EGPT [17], allowed for the perturbation and sensitivity analyses of reactivity coefficients, which means second derivatives of the multiplication factor.

In the last decade, these capabilities were extended to stochastic codes ([18], [2], [19]) thanks to the estimation of importance functions via Iterated Fission Probability (IFP, [20]).

Generalized Perturbation theory (GPT) applied to neutron transport allows for the calculation of neutrons importance, which corresponds to the contribution of each neutron to reactivity or to some reaction rates [1].

In the past, importance weighed functions such as k_{eff} sensitivities used to be calculated by deterministic codes solving adjoint transport equations. Nevertheless, it has been recently shown that Monte Carlo codes [2] can calculate k_{eff} sensitivity coefficients relative to a change in parameter x (S_x^k), by weighing accepted and rejected collisions over the collision history. This is possible also for importance-weighed quantities such as kinetic parameters (effective neutron lifetime, effective delayed neutron fraction, void coefficient [2]). The use of these sensitivities opens innovative possibilities for reactor physics, such as the perturbation of multiphysics models [21] [22] or the uncertainty evaluation of fuel evolution calculations [23].

At present, GPT is used intensively when the uncertainties are given in the form of covariance matrices, in order to estimate the uncertainty coming from nuclear data. The purpose of this study is to assess the strength of GPT in the propagation of "experimental uncertainties" (uncertainties arising from manufacturing tolerances and geometry details) as well.

The present work is then focused mainly on Depletion Perturbation Theory [24], [3], [4], [25], a specific branch of GPT, that allows for the estimation of sensitivity coefficients all along the fuel cycle, meaning that the effect of a perturbation at beginning of life (BOL), e.g. burnable poison density, can be quantified on some end of life (EOL) relevant parameter, such as multiplication factor or nuclide density.

1.1.4 Outline of the work

This project has been carried out in the framework of a PhD at Institut Laue-Langevin, which hosts the High Flux Reactor (Reacteur à Haut Flux, RHF), on which most of the uncertainty and sensitivity analysis has been performed. The industrial partner TechnicAtome and the Laboratoire de Physique Subisotopique et Cosmologie (LPSC) have also contributed significantly to the completion of the project.

The feasibility of the generalized perturbation theory approach in SERPENT has been assessed by verifying, with direct calculations' comparison, the uncertainty results obtained by post-processing of k_{eff} sensitivities. This analysis has shown to be very promising in order to improve uncertainty quantification, especially in study cases like the High Flux Reactor (RHF) [26].

The propagation of experimental uncertainties GPT has been subsequently applied to the accident scenario of a beam flooding in the RHF reflector pool. In this particular case, an EGPT approach has been employed in order to confront the uncertainties arising in the two different flooded and nominal configurations of the RHF.

Once these static uncertainties have been evaluated, the biggest focus of the project has been redirected to the assessment of uncertainties along the fuel cycle. This redirection is justified in the framework of the RHF conversion to Low Enriched Uranium fuel, raising the attention on actinides' buildup along the fuel cycle. During the first year of this PhD, an extensive sensitivity analysis has been performed on the burnable poison of the new LEU fuel, embracing the "uncertainty by design" approach on this crucial parameter for irradiation and thermal-hydraulics margins of the RHF core.

The extensiveness of the burnable poisons engineering study, where almost 6 months were spent iterating configurations and performing simulations spanning several weeks, justified the methodological development of Perturbation Theory. It was believed that opening the access to time-dependent sensitivity coefficients would expedite some design optimization, while also anticipating most results of the uncertainty analysis that is usually performed on the finalized design.

A simplified model of the RHF has been built in Python3 and called SIBYL (Scaling Incertitudes BY modeLIng), in order to assess the performance of Depletion perturbation Theory in an environment that would be fast and intuitive with respect to Monte Carlo codes, where DPT has not been implemented yet. SIBYL proved to be a powerful tool to reproduce the reactivity, flux, and nuclide densities evolution of the RHF cycle, providing a perfect environment for developing PTERODAx: a Perturbation Theory Engine for Reactor Outputs Depletion Analysis. The parallel development of PTERODAx, along with MCNP and SERPENT simulations, has proved to be an important addition to the sensitivity analysis, yielding priceless physical interpretation on the contributors of uncertainties, and confirming the strength of the burnable poison safety analysis results.

Similar studies to the ones performed on the RHF have successively been carried out on the UAM benchmark of OECD, in order to validate the results of the proposed methodology with international participants. In particular, a detailed propagation of nuclear data uncertainties, fully employing DPT, has been successfully compared to Total Monte Carlo methods developed by the other benchmark participants.

1.2 High Flux Reactor

As opposed to power reactors, research reactors carry out mainly two tasks. On one side they provide easier access, with respect to Power Plants, to Nuclear Reactor Physics understanding, allowing for experimental procedures, scientific education, operators training and new components testing. On the other side, they produce neutron fluxes that are exploited for isotope production, medicine and research, ranging from fundamental physics to biology and industrial applications. There are about 250 Research Reactors in the World (compared to 440 power reactors in operation worldwide presently), and while many of them have a design tailored to very specific applications, the biggest ones have a pool type configuration. In these reactors, a compact core is immersed in a tank of either light or heavy water, favoring safety and good moderation since the power produced does not need to be efficiently converted into electricity. The most common Research Reactor type certainly is the TRIGA Mark II, with more than 50 light water pool installations worldwide. Along with the Belgian Reactor 2 (BR2) and HFIR at Oak Ridge National Laboratory, High Flux reactors are the most widely exploited, comprising the Advanced Test Reactor (ATR) of Idaho National Laboratory and the RHF of Institut Laue-Langevin, that share the lead for highest neutron flux in the world of $1.5 \cdot 10^{15} \frac{n}{cm^2 \cdot s}$. They both employ thin HEU fuel plates and heavy water moderation in order to maximize the thermal flux in specific locations. The ATR is designed to host samples inside the core for irradiation testing, while the "Reacteur a Haut Flux" aims to maximize the leaked flux that feeds neutron science experiments.

Institut Laue-Langevin

The Institut Laue-Langevin (ILL) was founded in 1967 when the French Republic and the Federal Republic of Germany signed an agreement that lead to the first criticality of the RHF in 1971. In January 1974 the United Kingdom joined the ILL and became the third Associate Member country. In 1997, the Italian Government signed an agreement with the ILL to join a "Scientific Membership" that today counts 12 countries. In 1995 the reactor vessel was completely replaced, allowing the Institute to reach its 50th anniversary in 2017, and aiming to extend its lifetime with the new LEU design (in compliance with the IAEA safeguards and non-proliferation policy) to the 2040s.

The reactor has only one annular fuel element, which is made of curved plates of highly enriched uranium, and is cooled and moderated by heavy water. One control rod is operated inside the fuel element, and five safety rods are dropped outside the element to shut the reactor down. The RHF operates continuously for 50-day cycles, followed by a shutdown to change the fuel element. In addition, there is a longer shutdown to enable necessary maintenance work. Normally, there are 4 cycles each year, providing about 200 days of thermal neutrons to the over 40 experiments that simultaneously take place at the ILL. The neutrons are extracted from the pile using beam tubes (Figure 1.1) and sent to the ILL instruments for several kinds of scientific experiments like neutron diffraction, small angle neutron scattering, neutron reflectometry and inelastic neutron scattering. Ultra cold neutrons are also obtained via a liquid Deuterium source that is cooled down to 24K. Such low energy neutrons are used to tackle the uncertainty on the average neutron lifetime.

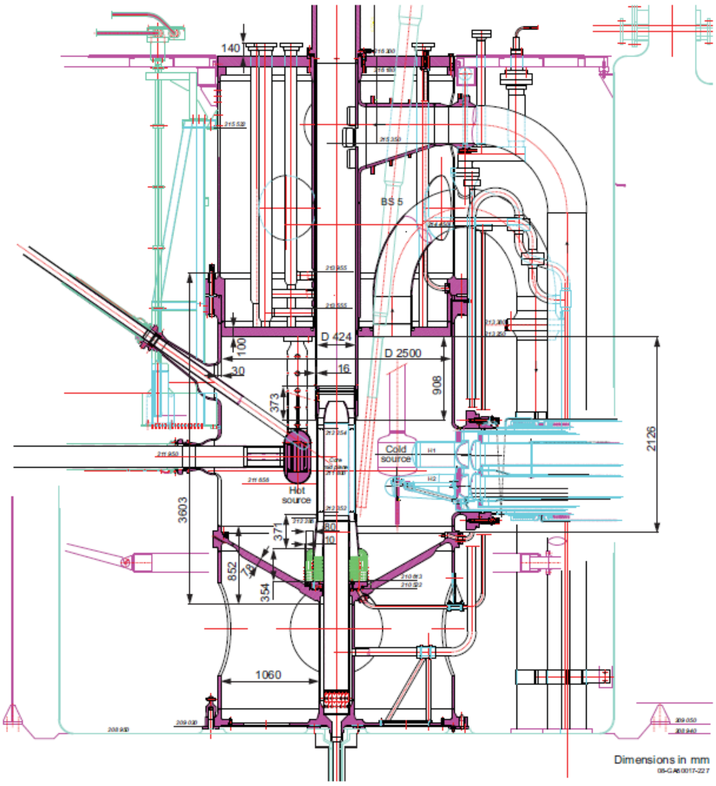

Figure 1.1: Vertical section of reactor pool and beam tubes

After more than 50 years since its foundation, the ILL is still a world leader in neutron science, a fine example of successful co-operation in Europe and a prototype for the European Research Area.

The RHF very bright flux is produced in a compact core immersed in a very large volume of heavy water, from which the neutrons are extracted from the reflector through 17 beam tubes (Fig. 1.2, left side). The reflector also provides most of the moderation, since the fuel element itself is greatly under-moderated. The fuel element comprises a total of 280 involute shaped fuel plates (Figure 1.2, right side). This maximizes the neutron leakages from the element, but also imposes a very high mass flow rate between the plates to cool down the fuel. This high power density, combined with the very small hydraulic diameters of the 280 narrow coolant channels, accounts for a pressure drop of 10 bars in just 1 meter of heated surface.

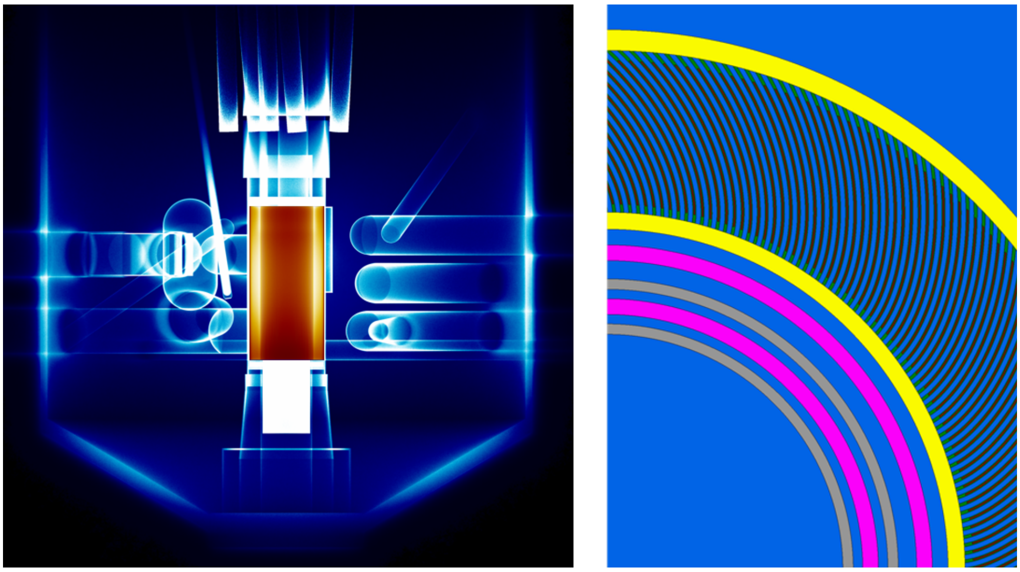

Figure 1.2: RHF absorption reactions mesh plot (left) and core detail in SERPENT (right). The 280 fuel plates are held together by a cylindrical tube (yellow), inside which the control rod is operated (pink)

Table 1.1: RHF characteristics

POWER	58.35 MWth
FUEL PLATE	93% enrichment, U-Al mix
FUEL ELEMENT	Annular assembly, 280 involute plates
REFLECTOR	Heavy Water (300K, 4 bar)
COOLANT	Heavy Water (290K, 14 bar)
BURNABLE POISON	Boron zones at fuel element extremities
CONTROL	1 rod, inside the element (Figure 1.2, in pink)
SAFETY MARGIN	5 rods, around the element
PEAK FLUX	$1.5 \cdot 10^{15} \frac{n}{cm^2 s}$

1.2.1 LEU conversion

The ILL was one of the early callers for change in conversion effort to LEU, and signed in 1998 a memorandum of understanding with the US Government to investigate conversion to a safer grade of uranium. ILL is still deeply involved into the conversion of its reactor, the RHF, into a Low Enriched Uranium (LEU) solution, with uranium enrichment below 20%. The final goal of this project is to remove Highly Enriched Uranium (HEU) fuel from the civil nuclear fuel cycle as far as is reasonable.

Fuel conversion at the ILL requires a high-density LEU fuel that can match the present HEU performance. High-density LEU fuel made of a uranium-molybdenum alloy, at 8g/cm3, is therefore a promising candidate but not qualified yet. Moreover, the high loaded uranium silicide alloy, at 4.8g/cm3 or higher, is an alternative that is considered as a backup for the RHF conversion. Nevertheless, with the higher presence of U-238 and the production of Pu-239 during burn-up, the safety parameters and the neutron sources' characteristics will evolve during the cycle much more than today. Calculating those changes accurately, demonstrating the high level of safety while minimizing the impact for the end user will be a challenge. A new generation of reactor physics simulation tools, which embed more easily uncertainty quantification, is becoming available.

The objective of this project is to grab the opportunities offered by the availability of those new tools and of the flexibility of the reactor that allows some reactor's physics experiment to contribute to the development, the validation and qualification of those tools on reactor's experiments and demonstrate their complementarity with the ones used today for the demonstration of the safe, continued high performance of the RHF.

In the LEU framework, the loss in fissile enrichment has been compensated by an increase in fuel density (U_3Si_2 compound) and by an increase in meat volume inside the plates (length, width and thickness). On the other hand, the increase in fertile material leads to Plutonium build-up at the end of the cycle, and the need to assess the related uncertainties. Furthermore, the fuel volume increase in the design leaves no more space for a burnable poison at the extremities of such plates.

The standard licensing procedures, required for the conversion to LEU, involve the employment of Monte Carlo codes to perform many direct calculations (for neutronic parameters, heat flux, uncertainties, criticality, reactivity worth...) and coupled evolution calculations (actinides densities, decay heat...). It is clear though that some key aspects, like the performance of the burnable poison, have an impact both in the optimization phase and in the licensing phase. Therefore, the need for a tool that would be able to provide useful insights on the sensitivity of nuclear parameters to design choices, without the burden of continuously carrying out the licensing calculations, that might take up to several weeks of computation is evident. For this reason, the parallel development of PTERODAx, along with MCNP and SERPENT simulations, has proven to be an important addition to the sensitivity analysis, yielding priceless physical interpretation on the contributors of uncertainties, and confirming the strength of the burnable poison safety analysis results.

1.3 UAM benchmark

Within the framework of the LWR Uncertainty Analysis in Modelling (UAM) benchmark, which aims to investigate the uncertainty propagation in all modeling stages of the LWRs and guide uncertainty and sensitivity analysis methodology development, many efforts have been devoted to Light Water Reactor (LWR) uncertainty quantification. In 2006, the Nuclear Science Committee of the Organization for Economic Co-operation and Development (OECD) and the Nuclear Energy Agency (NEA) began developing the UAM benchmark (NSC). The principal objective of the project is to "define, co-ordinate, conduct, and report an international benchmark for uncertainty analysis in best-estimate coupled code calculations for design, operation, and safety analysis of LWRs

The neutronics, thermal-hydraulics, and fuel thermal/mechanical behavior domains of nuclear reactor engineering are all covered by the LWR-UAM. The major sources of uncertainty are to be determined from these types of calculations, which may arise from data (nuclear data, geometry, materials), numerical methods, and physical models. The benchmark considers a vast amount of pre-existing benchmarking data and technical experience on LWRs and covers four different types of LWR: PWR, BWR, and VVER. The first phase of the benchmark (Phase I) is dedicated to stand-alone neutronics problems and is divided into three steps, each of which corresponds to a standard LWR simulation approach: cell physics (to generate multi-group microscopic cross-section libraries), lattice physics (to generate multi-group homogenized macroscopic cross-section sets), and core physics (to compute multi-group homogenized macroscopic cross-section sets) (to assess full core performance parameters). This report highlights the results of the comparative examination of neutronics solutions across participants for various reactor types, including PWR, BWR, VVER, and Gen-III reactors, as a conclusion to the work completed for Phase I. Because of the large number of results available, the study focuses on trends in the level of uncertainty caused by nuclear data.

1.3.1 LWR pin model

In order to perform a comparative analysis of the multi-group cross-section, uncertainty data obtained after processing test problems are devised or utilized from the previously defined benchmarks (participants can select which test problem to analyze): For a “cylindrical pin-cell” model, reflective boundary conditions are utilised at the center-line boundary while white boundary conditions are applicable at the peripheries of the cell-model.

1.3.2 Benchmark Chapters and Participants

The participants are asked for a variety of results, and in order to make the report structure clearer, the most important ones for each Exercise are

Table 1.2: UAM benchmark LWR fuel pin characteristics

Unit cell pitch	[mm] 14.427
Fuel pellet diameter	[mm] 9.391
Fuel pellet material	UO2
Fuel density	[g/cm3] 10.283
Fuel enrichment	w/o 4.85
Cladding outside diameter	[mm] 10.928
Cladding thickness	[mm] 0.673
Cladding material	Zircaloy-4
Cladding density	[g/cm3] 6.55
Gap material	He
Moderator material	H20
Reactor power	[MWt] 2.772

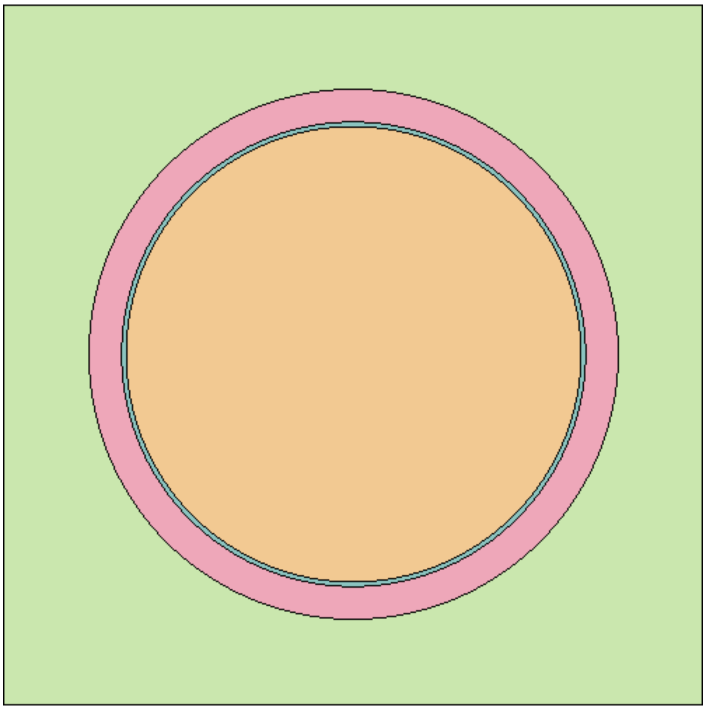

Figure 1.3: UAM benchmark LWR fuel pin 2D model, comprising Fuel (orange), helium gap (blue), cladding (pink) and water (green)

chosen and analysed. We concentrate on the k_{eff} uncertainty and the top five reactions in Exercise I-1. It focuses on the multiplication factor uncertainties, some representative two-group macroscopic cross-sections, the correlation matrices among the two-group cross-sections, and the radial power distribution in Exercise I-2, which is closely related to the conventional two-step LWR uncertainty propagation approach. It concentrates on k uncertainty as well as the radial and axial power distribution in the core in Exercise I-3. There are no requirements in the benchmark for the approach used to rank the five most important neutron-nuclide reactions for the k_{eff}. Because the results do not quantify how important each reaction is, they are qualitative, and participants could use a range of accessible methodologies, such as correlation coefficients [27] or Perturbation Theory sensitivities [28].

Uncertainty types

There are two types of uncertainties in general [8]:

- Stochastic (aleatory) uncertainty: Sources of uncertainty that are regarded irreducible due to natural intrinsic unpredictability. This suggests that the unknown variables will vary stochastically under the same conditions (e.g. temperature of a room). A common approach to model these uncertainties is by considering the variables as random and characterized by their probability density function (pdf), that can be determined through observation.

- Epistemic uncertainty: Uncertainties arising from a lack of knowledge. It's frequently associated with modeling, and it comes from a variety of sources, ranging from numerical approximation to physical models. This uncertainty can be minimized by doing more experiments, improving numerical solutions, and so on to gain a better understanding of the underlying physical events. In a Bayesian setting, if a PDF is used, it correlates to a degree of belief.

Uncertainty propagation

The neutron cross-section data, complemented by the variance-covariance matrices (VCMs), and manufacturing uncertainties in material composition and geometric dimensions are among the sources of input uncertainty evaluated in Phase I exercises. All of these potential sources of uncertainty are regarded as stochastic. The nuclear data are classified as multivariate normal with a corresponding VCM, while the other sources are classified as independent and hence have a marginal PDF. Because few participants included manufacturing concerns in Phase I, the UAM report focuses primarily on nuclear data".

In the present study, A simplified 0.5 dimensional model of the LWR-UAM benchmark has been built and called SIBYL, in order to assess the performance of Depletion Perturbation Theory (DPT) in estimating its end of life (EOL) uncertainties [3] [29]. The purpose of this tool is to calculate time-dependent sensitivity coefficients to different input perturbations, such as cross-sections and nubar, which combined with covariance matrices, can make an estimation of the corresponding nuclear data uncertainty. The appropriate benchmark chapter exercise that carries out this type of analysis is the I-1b, which mostly comprises Total Monte Carlo (TMC) and other sampling approaches by its participants [30], [31], [32]. The simplified model SIBYL is presented in section 3, while the results for EOL uncertainties have been successfully compared to the UAM benchmark in section 4.

Chapter 2

Methods

2.1 Reactor Physics

In this chapter, neutron transport is introduced both in its deterministic (Boltzmann Equation) and stochastic (Monte Carlo codes) characteristics. The depletion of nuclides in the multiplying system is described with the Bateman equation. Conventional Perturbation theory algorithms are exposed for both transport and depletion equations, and then the implementation of Generalized Perturbation Theory in the SERPENT Monte Carlo code is presented.

In particular, the variational approach to Depletion Perturbation Theory, proposed by Williams [33], has been used to unify the general results obtained by Takeda et al. [4] on importance weighed responses, and by the same Williams on criticality reset, under one and only variational formalism.

The final section on GPT in SERPENT retraces the original publication by Aufiero et al. [2], while providing more details on the deterministic equivalence and giving some physical interpretation of the statistical contributions in collision histories.

2.1.1 Boltzmann Transport equation

The transport of neutrons inside the reactor is ruled by the Boltzmann equation. This equation states that in a specific position r, the flux ϕ of neutrons of energy E and flight direction Ω is balanced by a positive contribution arising from fissions and scatterings, and by a negative contribution due to absorptions and leakages from the position r.

The loss operator $\hat{L_a}$ is simply given by the sum of all absorption cross-sections, while the streaming operator $\hat{L_\Omega}$ depends on the direction of the neutrons with respect to the gradient of the flux.

$$\hat{L_a} = -\Sigma_{tot} \tag{2.1}$$

$$\hat{L_\Omega} = -\boldsymbol{\Omega\nabla} \tag{2.2}$$

The scattering operator of this equation is an integral, over all the incoming neutron energies E' and directions Ω', of the macroscopic scattering cross-section σ_x times a transfer function f_x that accounts for the probability of reaching a specific point of the ensemble. Other (n, xn) reactions can be comprised as well to obtain the production operator:

$$\hat{L_s} = \sum_{x \neq f} \int \Sigma_x(\boldsymbol{r}, E') f_x[\boldsymbol{r}; (\boldsymbol{\Omega'}, E') \rightarrow (\boldsymbol{\Omega}, E)] \boldsymbol{d\Omega'} dE' \tag{2.3}$$

Similarly, the fission operator can be written, including the number ν of neutrons produced per fission as a function of the incoming neutron energy E':

$$\hat{F} = \int \Sigma_f(\boldsymbol{r}, E') \nu(E') f_f[\boldsymbol{r}; (\boldsymbol{\Omega'}, E') \rightarrow (\boldsymbol{\Omega}, E)] \boldsymbol{d\Omega'} dE' \tag{2.4}$$

By exploiting the almost perfect isotropy of the fission process, it is possible to also introduce a neutron emission spectrum χ that does not depend on the energy of the incoming neutron:

$$\hat{F} = \int \Sigma_f(\boldsymbol{r}, E') \nu(E') \frac{\chi(E)}{4\pi} \boldsymbol{d\Omega'} dE' \tag{2.5}$$

By summing the first three contributions ito L, the following Boltzmann B operator is defined:

$$B\psi = (L - \lambda F)\psi = 0 \tag{2.6}$$

Where k is the multiplication factor, that, by adjusting the number ν of neutrons emitted per fission, allows to study a stationary equation even when the reactor is far from criticality. While ψ is the shape component of the neutron flux.

$$\hat{B}\psi(\boldsymbol{r}, \boldsymbol{\Omega}, E) = 0 \tag{2.7}$$

In fact, in order to study a static Boltzmann equation, the following quasi-static approximation has been employed on the neutron flux Φ:

$$\Phi(\boldsymbol{r}, \boldsymbol{\Omega}, E, t) = \phi(t)\psi(\boldsymbol{r}, \boldsymbol{\Omega}, E) \tag{2.8}$$

The shape component will follow a unitary normalization:

$$\int\int\int \psi(\boldsymbol{r}, \boldsymbol{\Omega}, E) dr d\Omega dE = 1 \tag{2.9}$$

While the time dependent component will follow the reactor power level for appropriate normalization :

$$\phi(t)\int\int\int C(E)\Sigma_f(\boldsymbol{r}, \boldsymbol{\Omega}, E, t)\psi(\boldsymbol{r}, \boldsymbol{\Omega}, E) dr d\Omega dE = P(t) \tag{2.10}$$

Where C is the average energy per fission, while P is total reactor power.

2.1.2 Bateman Depletion equation

The Bateman equation describes the time dependency of the isotopic number densities. In solid fuel reactors, the space independence of the nuclide field is a major advantage in writing the transmutation balance equation. This balance takes place among three types of contributions: fission yield, neutron absorption, and nuclear decays. The fission yield contribution for nuclide i is given by:

$$G_i(\phi, t) = \sum_j N_j \int\limits_0^\infty \gamma_{ij}(E, t)\sigma_f^j(E, t)\phi(E)\psi(E, t) dE \tag{2.11}$$

Where σ_f^j is the microscopic fission cross-section of nuclide j, while γ_{ij} is the fraction of fissions on nuclide j who yield nuclide i as a result.

The neutron absorption contribution is given by:

$$H_i(\phi, t) = \int_0^\infty \Big[\sigma_c^{i-1}(E,t)N_{i-1} - \sigma_c^i(E,t)N_i\Big]\phi(E)\psi(E,t)dE \tag{2.12}$$

Where positive contribution come from captures on nuclide $i-1$ and negative contributions comprise any absorption $\sigma_a = \sigma_f + \sigma_c$ on nuclide i. Finally, the decay term will just be:

$$D_i(t) = -\lambda_i N_i + \sum_j \lambda_{j,i} N_j \tag{2.13}$$

Where $\lambda_{j,i}$ is the decay constant of nuclide j towards nuclide i. In writing the Bateman balance equation, it is useful to separate the first two contributions $G(\Phi,t) + H(\Phi,t) = R(\Phi,t)$ from the third one, which is independent of the neutron flux. In compact matrix notation, it will be:

$$\frac{d\boldsymbol{N}(t)}{dt} = [R(\Phi,t) + D(t)]\boldsymbol{N} = M(\Phi,t)\boldsymbol{N} \tag{2.14}$$

A generic nuclide source Q can be added to the equation to account for example for external injections of control nuclides (PWR diluted boron concentration) or even fissile materials (CANDU, pebble-bed or liquid reactors).

$$\frac{d\boldsymbol{N}(t)}{dt} = M(\Phi,t)\boldsymbol{N} + \boldsymbol{Q(t)} \tag{2.15}$$

2.2 Perturbation Theory

The goal of Perturbation Theory (GPT) is the definition of sensitivity coefficients, i.e. normalized derivatives of some model output with respect to an input parameter, allowing for the quantification of relevant uncertainties, without running multiple perturbed calculations. In Monte Carlo codes especially, the time needed for multiple modelling and multiple calculations can quickly become prohibitive, and a very relevant stochastic implementation of GPT to the code SERPENT has been developed in 2015 [2]. This work is focused on Depletion Perturbation Theory [3] [4], a specific branch of GPT, that allows for the estimation of sensitivity coefficients all along the fuel cycle, meaning that the effect of a perturbation at BOL (e.g. burnable poison concentration) can be quantified on some EOL relevant parameter such as multiplication factor or plutonium concentration.

2.2.1 Adjoint Equations

In order to develop perturbation theory and obtain sensitivity coefficients, an importance function needs to be defined. This is done by investigating the adjoint problem for the Boltzmann equation. Considered the Hilbert space of measure $\mu = g(\boldsymbol{r}, \boldsymbol{\Omega}, E, t) = g(\hat{\rho}, t)$, the flux is assumed to be a square integrable function, where $\hat{\rho}$ is the phase space:

$$\Phi = f(\hat{\rho}, t), \Phi \in L^2(R^3) \tag{2.16}$$

and the internal product between two functions of this space is defined as:

$$< \Phi | \Psi >= \int \int \Phi(\hat{\rho}, t)\overline{\Psi}(\hat{\rho}, t) d\hat{\rho} dt \tag{2.17}$$

Since the Boltzmann operator $\hat{B}$ is not self-adjoint [34], the adjoint operator $\hat{B}^{\dagger}$ satisfies the following equation:

$$< \hat{B}\Phi | \Phi^{\dagger} >=< \Phi | \hat{B}^{\dagger}\Phi^{\dagger} > \tag{2.18}$$

Where $\hat{B}^{\dagger}\Phi^{\dagger}$=0 is the adjoint Boltzmann equation. The eigenvalues of this equation are symmetrical with respect to the direct equation, suggesting some analogies on the mathematical point of view, but with opposite physical interpretation. What in the direct problem is a source of neutrons or a "creation rate", in the adjoint problem is in fact a reaction rate in a specific location.

For this reason, the adjoint flux can be interpreted as an importance function that tells to which extent a neutron contributes to the detector counts in the "source" location. By handling of the source term and of the initial conditions, the adjoint flux can be made to represent the importance of neutrons in contributing to other parameters like reactor power or the neutron flux itself.

Finally, if equation 2.7 is considered in its matrix form $B\Phi = 0$, then the adjoint Boltzmann matrix B^* takes the form of the transposed Boltzmann matrix $B^* = B^T$. This follows from the fact that the Boltzmann matrix has no complex component [34]. Per il

Bateman adjoint equation

In a similar fashion, we can define a an importance function for the Bateman eqaution. Starting from previously defined time dependent problem:

$$MN(t) = \frac{d}{dt}N(t) - Q \tag{2.19}$$

We derive the adjoint time dependent problem:

$$M^*N^*(t) = -\frac{d}{dt}N^*(t) - Q^* \tag{2.20}$$

Where the nuclide adoint field N^* assumes the meaning of an importance function depending on the type of source and response that are chosen for the problem. It will be shown that, as an example, if a nuclide response such as the final plutonium concentration in the fuel was chosen, N_i^* would be the probability for nuclide i to directly or indirectly transmute into plutonium by the end of the cycle.

2.2.2 Generalized Perturbation Theory

Perturbation theory studies the impact of alterations in some of the available data to the main parameters of the analyzed model. In Reactor Physics, this usually translates into the study of how cross sections and fission spectrum modifications impact the value of the multiplication factor k_{eff}, the delayed neutron fraction β_{eff} or the void coefficient α_v for example. In this section, the deterministic procedure that leads to the definition of k_{eff} sensitivities is presented [34].

A perturbation in the cross sections of the system is introduced:

$$(\Sigma_x f_x)' = \Sigma_x f_x + \Delta(\Sigma_x f_x) \tag{2.21}$$

$$(\Sigma_f \nu)' = \Sigma_f \nu + \Delta(\Sigma_f \nu) \tag{2.22}$$

Subsequently, the flux, the multiplication factor, and the boltzmann operator will be altered as well:

$$k' = k + \Delta k \tag{2.23}$$

$$\Phi' = \Phi + \Delta\Phi \tag{2.24}$$

$$\hat{B}' = \hat{B} + \Delta\hat{B} \tag{2.25}$$

Breaking the Boltzmann operator into the usual four components:

$$\hat{B} = \hat{L_\Omega} + \hat{L_a} + \hat{L_s} + \frac{1}{k}\hat{F} \tag{2.26}$$

We can state that the streaming operator $\hat{L_\Omega} = -\mathbf{\Omega}\mathbf{\nabla}$ is not perturbed since it is purely mathematical. The changes in the other operators are summarized below, with isotropic fission ($($f) subscript) and no dependence of the emission spectrum on the incoming energy E' of the neutron:

$$\Delta\hat{L_a} = -\Sigma^*_{tot} - (-\Sigma_{tot}) = -\Delta\Sigma_{tot} \tag{2.27}$$

$$\Delta\hat{L_s} = \sum_{x \neq f} \int \Delta(\Sigma'_x f'_x) \boldsymbol{d\Omega'} dE' \tag{2.28}$$

$$\Delta\hat{F} = \int \Delta(\nu'\Sigma'_f \frac{\chi}{4\pi}) \boldsymbol{d\Omega'} dE' \tag{2.29}$$

This leads to the following total perturbation of the stationary Boltzmann operator:

$$\Delta\hat{B} = \Delta\hat{L_a} + \Delta\hat{L_s} + \frac{1}{k^*}\hat{L^*_{T_f}} - \frac{1}{k}\hat{F} \tag{2.30}$$

$$\Delta\hat{B} = \Delta\hat{L_a} + \Delta\hat{L_s} + \frac{1}{k^*}\Delta\hat{F} - \frac{\Delta k}{kk^*}\hat{F} \tag{2.31}$$

Writing the stationary form of the Boltzmann equation for the perturbed system and employing the definition of the adjoint operator given in Eq. 2.18, the following identities can be written:

$$< \hat{L}^\dagger\Phi^\dagger > = < \hat{L}'\Phi' > = 0 \tag{2.32}$$

$$< \hat{L}^\dagger\Phi^\dagger|\Phi' > = < \Phi^\dagger|\hat{L}\Phi' > = 0 \tag{2.33}$$

Employing these last two equations, it is possible to state that:

$$< \Phi^\dagger|\hat{L}'\Phi' > = < \Phi^\dagger|\hat{L}\Phi' > + < \Phi^\dagger|\Delta\hat{L}\Phi' > = 0 \tag{2.34}$$

Which can be further reduced by neglecting the second order term:

$$< \Phi^\dagger|\Delta\hat{L}\Phi' > \simeq < \Phi^\dagger|\Delta\hat{L}\Phi > \simeq 0 \tag{2.35}$$

Expanding this last result and isolating the term coming from the multiplication factor k variation to the right-hand side of equation 2.35:

$$< \Phi^\dagger|(\Delta\hat{L_a} + \Delta\hat{L_s} + \frac{1}{k'}\Delta\hat{F})\Phi > = \frac{\Delta k}{kk'} < \Phi^\dagger|\hat{F}\Phi > \tag{2.36}$$

In the framework of a critical reactor where small perturbations are performed ($\Delta k \simeq 0$), the reactivity can be written with the same definition that stems from point reactor kinetics (Appendix A):

$$\frac{k' - 1}{k'} = \frac{< \Delta\hat{L}\Phi|\Phi^\dagger >}{< \hat{F}\Phi|\Phi^\dagger >} \tag{2.37}$$

This result is important because the perturbation in multiplication factor can be retrieved, starting from the direct and adjoint unperturbed fluxes, by performing an integral with the perturbed operator, meaning that only the calculations in the reference case are needed. By normalizing equation 2.37 by the generic parameter x, follows the definition of the first order k_{eff} sensitivity, that has been extended to perturbations outside cross-sections:

$$S_x^{k_{eff}} = \frac{\frac{dk}{k}}{\frac{dx}{x}} = \frac{< \Phi^\dagger | \frac{1}{k} \frac{\delta \hat{F}}{\frac{\delta x}{x}} \Phi > + < \Phi^\dagger | \frac{\delta \hat{L_a}}{\frac{\delta x}{x}} \Phi > + < \Phi^\dagger | \frac{\delta \hat{L_s}}{\frac{\delta x}{x}} \Phi >}{< \Phi^\dagger | \frac{1}{k} \hat{F} \Phi >} \tag{2.38}$$

The sensitivity coefficient is a normalized derivative of the studied parameter with respect to the perturbed one. For example, the k_{eff} sensitivity to a perturbation in the fission cross-section will be: $S_{\Sigma_f}^k = \frac{dk/k}{d\Sigma_f/\Sigma_f}$. And multiplying $S_{\Sigma_f}^k$ by the relative change in fission cross-section, a reactivity change can be readily retrieved.

2.2.3 Variational approach

In order to present an alternative approach to define sensitivity coefficients to a certain response parameter R, we define the following auxiliary functional K:

$$K = R - < Z(AY - Q) > \quad ; \quad \Delta K = \Delta R \tag{2.39}$$

Where $AY = Q$ is a generic system equation ruled by the Y operator, while Z is called a Lagrange multiplier. The analog perturbed system equation will be $A'Y' = Q'$. From this follows the perturbed functional K':

$$K' = K(Z', Y', \alpha') = K + \left\langle \frac{\partial K}{\partial \alpha} \Delta \alpha + \underbrace{\frac{\partial K}{\partial Z} \Delta Z + \frac{\partial K}{\partial Y} \Delta Y}_{\text{functional variations}} \right\rangle \tag{2.40}$$

Where the last two derivatives are called functional variations. The objective of this formalism is to make these variations disappear. In this way K would only vary according to the perturbed parameter α, and the following result would be easily retrievable:

$$\Delta R =< \frac{\partial K}{\partial \alpha}\Delta\alpha >=< \frac{\partial R}{\partial \alpha} - Z\frac{\partial A}{\partial \alpha}Y + Z\frac{\partial Q}{\partial \alpha} > \tag{2.41}$$

Following the rules of calculus of variations [35], the objective is to impose:

$$\frac{\partial K}{\partial Z}\Delta Z =< (AY - Q)\Delta Z >= 0 \tag{2.42}$$

$$\frac{\partial K}{\partial Y}\Delta Y =< (\frac{\partial R}{\partial Y} - ZA)\Delta Y >= 0 \tag{2.43}$$

The first one is already verified, while the second one can be rewritten according to the adjoint properties of a real operator [34]:

$$ZA = A^T Z = A^* Z = \frac{\partial R}{\partial Y} \tag{2.44}$$

Which has the form of the following adjoint problem, by choosing the proper Q^*:

$$A^* Y^* = Q^* = \frac{\partial R}{\partial Y} \tag{2.45}$$

It follows that $Z = Y^*$:

$$\Delta R =< \frac{\partial R}{\partial \alpha} - Y^*\frac{\partial A}{\partial \alpha}Y + Y^*\frac{\partial Q}{\partial \alpha} > \tag{2.46}$$

Which is identical to the solution derived from the differential approach. The auxiliary functional takes the form:

$$K = R - < Y^*(AY - Q) - \sum_i C_i^*(C_i - S_i) > \tag{2.47}$$

Where any additional constraint can be taken in consideration in the form of:

$$C_i(Y, \alpha) = S_i \tag{2.48}$$

Yielding a variation in the response always of the same form:

$$\Delta R =< \frac{\partial R}{\partial \alpha} - Y^*\frac{\partial A}{\partial \alpha}Y + Y^*\frac{\partial Q}{\partial \alpha} - C^*\frac{\partial C}{\partial \alpha} + C^*\frac{\partial S}{\partial \alpha} > \tag{2.49}$$

2.2.4 Depletion Perturbation Theory

In order to define the time dependent equivalent of the generalized perturbation theory sensitivity coefficient, the variational approach will be employed on the adjoint Bateman equation. Following the adjoint source definition in Eq. 2.45, and if we only consider delta function responses at $t = t_f$, it follows that equation 2.20 becomes:

$$M^* N^* = -\frac{\partial}{\partial t} N^* \tag{2.50}$$

With:

$$N^*(t_f) = \frac{\partial R}{\partial N} \tag{2.51}$$

We now proceed to define the auxiliary functional for this kind of responses, by appending equations 2.19, 2.6, 2.9, 2.10 to equation 2.47. From now on, the square brackets notation will imply integration over the phase space $([g(\hat{\rho})]_{\hat{\rho}} = \int g(\hat{\rho}) d\hat{\rho})$.

$$\begin{aligned} K(\hat{\rho}) = K(N, \psi, \phi, \alpha, \lambda) = R(N, \psi, \phi) + \sum_i \int_t \left[N^*(r,t)(M - \frac{\partial}{\partial t}) N(r,t) \right]_V dt \quad + \\ - \sum_i \left[\Gamma_i^*(\hat{\rho}) \Big(L(N_i) - \lambda_i F(N_i) \Big) \psi_i(\hat{\rho}) \right]_{\Omega,E,V} + \\ - \sum_i P_i^* \left([\psi_i \sigma_f N_i]_{\Omega,E,V} \, \phi_i - P_i \right) - \sum_i a_i^* \left([\psi_i]_{\Omega,E,V} - 1 \right) \end{aligned} \tag{2.52}$$

Much like equations 2.42 and 2.43 in the previous section, now the functional variations of K' must be set to zero, one by one.

$$\Delta K = \left\langle \frac{\partial K}{\partial \alpha} \Delta \alpha + \underbrace{\frac{\partial K}{\partial \phi} \Delta \phi + \frac{\partial K}{\partial \psi} \Delta \psi + \frac{\partial K}{\partial N} \Delta N}_{\text{functional variations}} \right\rangle \tag{2.53}$$

Starting from the flux normalization component $\frac{\partial K}{\partial \phi_i}$ (the Boltzmann terms in Eq. 2.52 don't depend on ϕ):

$$\frac{\partial K}{\partial \phi_i} = \frac{\partial R}{\partial \phi_i} + \int_t \left[N^*(t) (\frac{\partial M}{\partial \phi_i}) N(t) \right]_V dt - P_i^* \, [\psi_i \sigma_f N_i]_{\Omega,E,V} \tag{2.54}$$

Which yields a definition for P_i^*:

$$P_i^* = \frac{\int_t \left[N^*(t) \frac{\partial M}{\partial \phi_i} N(t) \right]_V dt + \frac{\partial R}{\partial \phi_i}}{[\psi_i \sigma_f N_i]_{\Omega,E,V}} \tag{2.55}$$

Examining now the flux spectrum component $\frac{\partial K}{\partial \psi_i}$, which is a vector derivative:

$$\frac{\partial K}{\partial \psi_i} = \frac{\partial R}{\partial \psi_i} - \Gamma_i^*[L(N_i) - \lambda_i F(N_i)] - P_i^* \sigma_f N_i \phi_i - a + \phi_i \int_t N^*(t) \frac{\partial M}{\partial \psi_i} N(t) dt \tag{2.56}$$

In order for this term to vanish, the following adjoint problem must be solved for Γ^*:

$$[L^*(N_i) - \lambda_i F^*(N_i)]\Gamma_i^* = W^* = \frac{\partial R}{\partial \psi_i} - P_i^* \sigma_f N_i \phi_i - a + \phi_i \int_t N^*(t) \frac{\partial M}{\partial \psi_i} N(t) dt \tag{2.57}$$

An additional constraint needs to be applied on Γ^*, and it is discussed in the next section.

The functional variation with respect to N has to take into account differentiation under the integral sign. Analysing the open interval $(t_i^+; t_{i+1}^-)$:

$$\frac{\partial}{\partial N} \int_{t_i^+}^{t_{i+1}^-} N^*(t)(M - \frac{\partial}{\partial t}) N(t) dt = \left| N^* M N \frac{\partial t}{\partial N} - N^* \frac{\partial N}{\partial t} \frac{\partial t}{\partial N} \right|_{t_i^+}^{t_{i+1}^-} + \\ + \int_{t_i^+}^{t_{i+1}^-} N^*(t)(M - \frac{\partial}{\partial t}) \cdot 1 dt \tag{2.58}$$

Where we accounted for discontinuities in N^* at every t_i. If we approximate $\frac{\partial t}{\partial N} \approx 0$, the total functional variation will be:

$$\frac{\partial K}{\partial N} = \frac{\partial R}{\partial N} + \sum_i \int_t \left[(M^* + \frac{\partial}{\partial t}) N^*(r,t) \right]_V dt - \sum_i \left[N_{i+1}^{*-} - N_i^{*+} \right]_V + \\ - \sum_i \left[\Gamma_i^* \frac{\partial}{\partial N} \Big(L(N_i) - \lambda_i F(N_i) \Big) \psi_i \right]_{\Omega,E,V} - \sum_i P_i^* \phi_i \left[\psi_i \sigma_f \right]_{\Omega,E,V} \tag{2.59}$$

The first two terms disappear following the adjoint problem posed in equations 2.50 and 2.51, where $N^*(t_f)$ appears within the expansion of the third, fourth and fifth term over all time steps:

$$\frac{\partial R}{\partial N} + \Bigg[N_0^{*+} + \Big[\Gamma_i^* \frac{\partial}{\partial N}\Big(L(N_0) - \lambda_i F(N_0)\Big)\psi_0 - P_0^* \phi_0 \psi_0 \sigma_f\Big]_{\Omega,E} + \quad \dots$$
$$\dots \quad + (N_i^{*+} - N_i^{*-}) + \Big[\Gamma_i^* \frac{\partial}{\partial N}\Big(L(N_i) - \lambda_i F(N_i)\Big)\psi_i - P_i^* \phi_i \psi_i \sigma_f\Big]_{\Omega,E} +$$
$$\dots \quad + \quad N_f^{*-} \Bigg]_V = 0 \qquad (2.60)$$

From this, follows that the adjoint nuclide field $N^*(t)$ effectively requires a discontinuity at every t_i in order for K to satisfy the independence from this functional variation. The discontinuity jump is therefore defined as follows:

$$N_i^{*+} - N_i^{*-} = \Big[\Gamma_i^* \frac{\partial}{\partial N}\Big(L(N_i) - \lambda_i F(N_i)\Big)\psi_i - P_i^* \phi_i \psi_i \sigma_f\Big]_{\Omega,E} = \Big[\Gamma_i^* \beta_i - P_i^* \Pi_i\Big]_{\Omega,E} \qquad (2.61)$$

Where the two quantities β and Π were introduced to denote the contribution coming from flux spectrum and power normalization perturbations.

Once all the involved parameters satisfy the required conditions, it is possible to define a sensitivity coefficient for the response R to the perturbed parameter α. Which we imposed to have the same dependency to the derivative of k.

$$S(\hat{\rho}) = \frac{\alpha}{R}\left(\frac{\partial K}{\partial a}\right) \qquad (2.62)$$

It follows that:

$$S(\hat{\rho}) = \frac{\partial R}{\partial \alpha} + \sum_i \int_t N^*(r,t) \frac{\partial}{\partial \alpha} M N(r,t) dt -$$
$$\sum_i \Big[\Gamma_i^*(\hat{\rho}) \frac{\partial B_i}{\partial \alpha} \psi_i(\hat{\rho})\Big]_\Omega - \sum_i P_i^* \phi_i \left[\psi_i(\hat{\rho}) \sigma_f N(r)\right]_\Omega \qquad (2.63)$$

Adjoint Flux orthogonality constraint

Considering the forward and adjoint Boltzmann equations:

$$B\psi = 0 \qquad ; \qquad B^*\Gamma^* = Q^* \qquad (2.64)$$

And in particular, considering the definition of the adjoint problem:

$$< \Gamma^* | B\psi > = < \psi | B^* \Gamma^* > = 0 \quad ; \quad < \psi | Q^* > = 0 \tag{2.65}$$

It follows that the adjoint source must be chosen perpendicular to the direct neutron field distribution.

This imposes that a_i in equation 2.52 to satisfy:

$$\psi_i \frac{\partial R}{\partial \psi_i} - \phi_i \frac{\partial R}{\partial \phi_i} = a_i \tag{2.66}$$

Which is already verified for most responses of practical interest, such as nuclide concentrations.

Importance weighed responses

In cases in which the response function is not merely a nuclide concentration or some other model constituent, but it is a mathematically defined parameter, such as the multiplication factor, the functional variation to any considered importance function needs to be taken into account. For the homogeneous adjoint flux, for example, we append the homogeneous adjoint Boltzmann equation to K:

$$K = R - < Z(\phi^* B^* - 0) > \tag{2.67}$$

From equation 2.44 follows that $Z = \psi$, and the functional variation will be:

$$\frac{\partial K}{\partial \phi_i^*} = \frac{\partial R}{\partial \phi_i^*} - \psi[L^*(N_i) + \lambda_i F^*(N_i)] \tag{2.68}$$

Which is perfectly similar to equation 2.56, and will in fact add a spectrum contribution to the sensitivity that mirrors the one already defined:

$$\begin{aligned} S(\hat{\rho}) = \frac{\partial R}{\partial \alpha} + \sum_i \int_t N^*(r,t) \frac{\partial}{\partial \alpha} M N(r,t) dt - \sum_i \left[\Gamma_i^*(\hat{\rho}) \frac{\partial B_i}{\partial \alpha} \psi_i(\hat{\rho}) \right]_\Omega \\ - \sum_i \left[\psi_i(\hat{\rho}) \frac{\partial B_i^*}{\partial \alpha} \phi_i^*(\hat{\rho}) \right]_\Omega - \sum_i P_i^* \phi_i \left[\psi_i(\hat{\rho}) \sigma_f N(r) \right]_\Omega \end{aligned} \tag{2.69}$$

Where:

$$\beta^* = \frac{\partial}{\partial \alpha} [L^*(N_i) + \lambda_i F^*(N_i)] \tag{2.70}$$

Criticality condition

As the forward equations demand an external condition, such as the power normalization equation, the same is required by the adjoint equation. Otherwise, the linear system of differential equations would be indeterminate, since the multiplication factor is purposely chosen to yield a singular matrix.

The choice of normalization equation depends on the treatment of the multiplication factor along the burnup steps. A different condition needs to be imposed on K depending on whether the reactor is kept critical by some control nuclide or whether it is evolving freely to a progressively less reactive condition.

In case of free evolution, the proper criticality condition will be:

$$< \Gamma^* | \frac{\partial}{\partial \lambda}(L - \lambda F)\psi > \quad = \quad < \Gamma^* | F\psi > \quad = \quad 0 \tag{2.71}$$

While the proper condition in case of k-reset, operated through some control nuclide N_c, will be:

$$< \Gamma^* | \frac{\partial}{\partial N_c}(L - \lambda F)\psi > \quad = \quad 0 \tag{2.72}$$

Which can either replace one of the equations inside the singular B^* matrix, or it can explicitly incorporate some homogeneous component in the form $\Gamma^* = \Gamma_p^* + b\phi^*$. Where Γ_p^* is any particular solution of the adjoint equation, and hence orthogonal to the adjoint solution ϕ^*. The linear combination coefficient b will then take the form:

$$b = \frac{\left[\Gamma^* \frac{\partial}{\partial N_c}(L - \lambda F)\psi\right]_{\Omega,E,V}}{\left[\phi^* \frac{\partial}{\partial N_c}(L - \lambda F)\psi\right]_{\Omega,E,V}} \tag{2.73}$$

The physical advantage gained from these conditions is the independence of the adjoint function Γ^* from the evolving fission source or control nuclide concentration.

Criticality reset

If a k-reset is operated at each burn up step, a new constraint is imposed on the system in the form of an additional term to the sensitivity. Let's introduce this criticality constraint into the variational approach formalism by first rewriting the Bateman depletion equation:

$$\frac{\partial}{\partial t}N = MN - \left(I_c^T \frac{\partial k}{\partial t}\frac{\partial}{\partial k} \right) N = (M - P)N \tag{2.74}$$

Where the new operator P transforms any reactivity change into the nuclide composition that yields back a critical system, acting only on the chosen control nuclide through the versor I_c. Since this is already a differential operator, we can neglect its functional variations with respect to ϕ and ψ, under the hypotheses of first order perturbation theory. It follows that the response variation related to P will follow the same variation of the Bateman operator:

$$\Delta R = \frac{\partial R}{\partial \alpha} + \sum_i \int_t N^* \frac{\partial}{\partial \alpha} MNdt - \sum_i \int_t N^* \frac{\partial}{\partial \alpha} PNdt \tag{2.75}$$

Incorporating the α derivative into the definition of P, it is possible to explicitly refer to this term as a sensitivity ratio:

$$\sum_i \int_t N_c^* \frac{\partial}{\partial \alpha} \left(\frac{\partial k}{\partial t}\frac{\partial}{\partial k} \right) N_c dt = \sum_i \int_t \frac{\partial}{\partial t} \left(N_c^* \frac{\partial k}{\partial \alpha}\frac{\partial N_c}{\partial k} \right) dt \tag{2.76}$$

The additional criticality reset term therefore accounts for the reactivity weighed contribution of the perturbed nuclide, with respect to the control one, towards the response function.

$$S_{reset} = \sum_i N_c^* \frac{S_\alpha^k}{S_{N_c}^k} \tag{2.77}$$

As such, the extra term can be appended to the other terms in equation 2.63, where both k sensitivities can be obtained from equation 2.38

2.2.5 Covariance Matrices

Once energy dependent sensitivity vectors S_x are calculated, they can be used to assess the uncertainty related to a particular parameter x if the covariance matrix COV_x is available. In this matrix, the uncertainty on the parameter value is stored on the diagonal, while all the cross dependencies between energies, that lie for example in the cross-section models, fill the rest. A few examples of covariance matrices for the most relevant actinide cross-sections are presented in Figure 2.1. The k_{eff} uncertainty (or any other parameters') related to nuclear data can then be calculated by the equation below: [36].

$$\sigma_x^k = \sqrt{S_x^k \times COV_x \times \overline{S_x^{k'}}} \tag{2.78}$$

Other than providing a tool for quick uncertainty quantification, these sensitivities can also provide useful insights of physical phenomena inside the reactor. As an example, the k_{eff} sensitivity to a perturbation in heavy water (light blue) around and inside the control rod of the RHF is shown in Figure 2.2. In this case, it is clear how the increase of total cross-section for high energy neutrons brings to an increase in k_{eff}, while increasing the cross-section seen by low energy neutrons leads to a decrease in reactivity. This is because high energy neutrons have enough energy to overcome the control rod and cause fission, while the lower energy neutrons are basically being moderated to prepare an absorption by the Nickel in the control rod (pink).

2.3 Monte Carlo codes

A Monte Carlo Code for Fission Reactor Physics is based on the simulation of a large amount of neutron histories. Each material contributes to the neutron histories by means of its cross section, that provides the probability of interaction of the material with each neutron. The neutron path in between reactions with surrounding nuclides is sampled via these probabilities and each reaction is scored in an appropriate tally. By handling of all

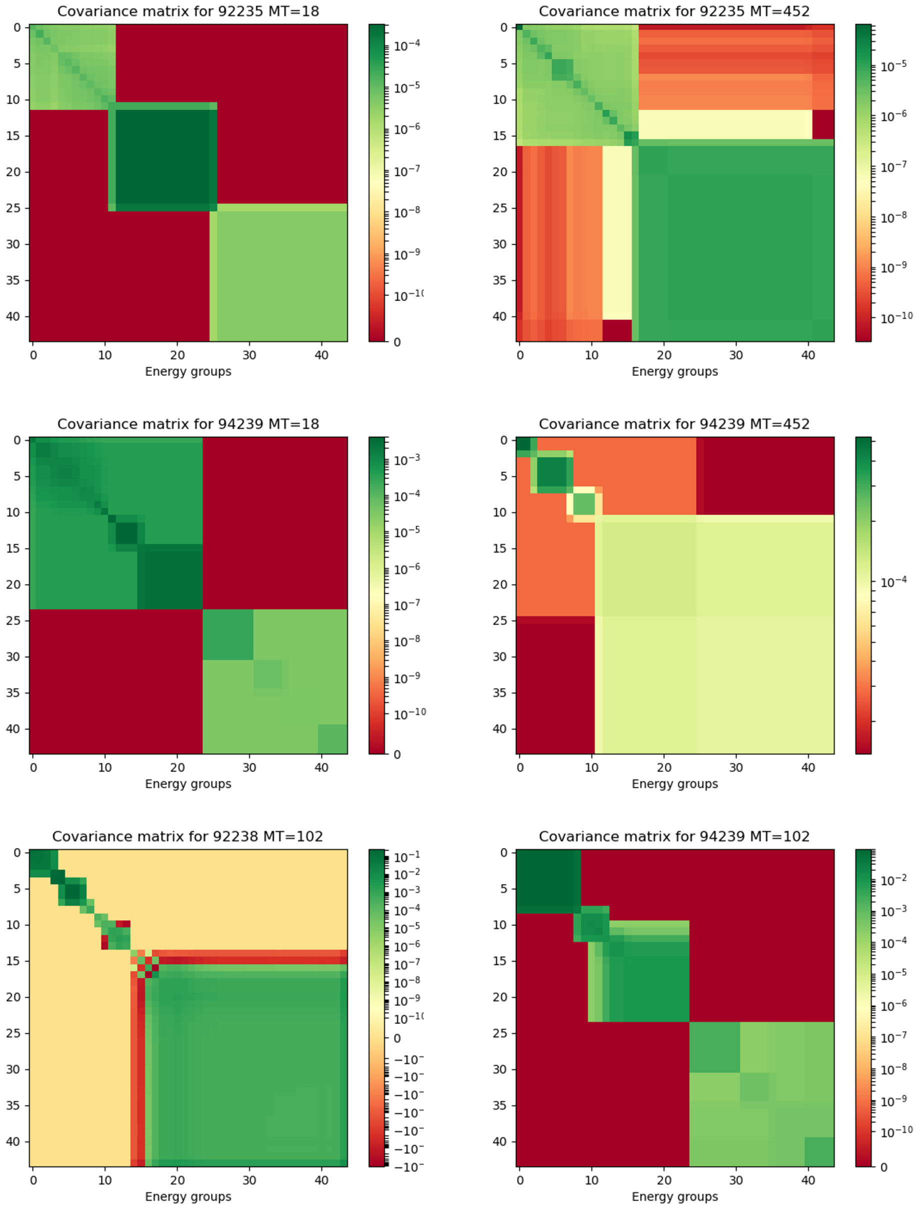

Figure 2.1: Covariance matrices for fission (MT=18), capture (MT=102) and nubar (MT=452) nuclear data. ENDF-B-VI library, 44 energy groups V6COV matrices.

[H]

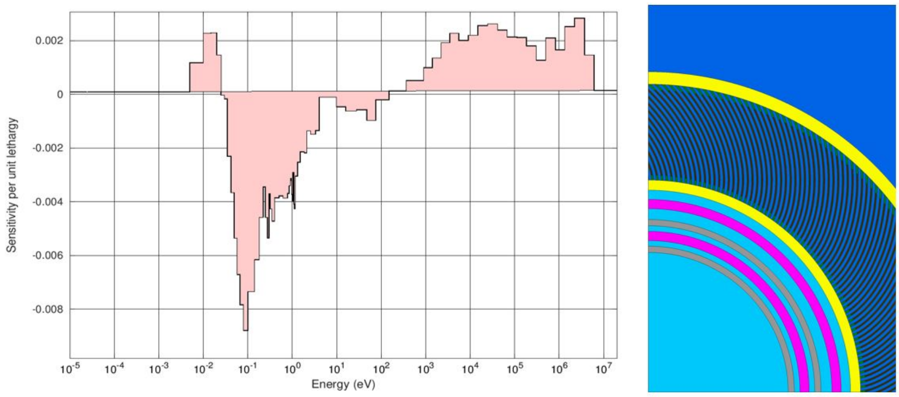

Figure 2.2: Energy dependent k_{eff} sensitivity to a perturbation in water (light blue) surrounding the RHF control rod (pink)

the tallies, this intrinsically stochastic process provides an estimation of the reactor parameters.

2.3.1 Non-analog transport

The Monte Carlo code is a very accurate tool for calculating the flux, the multiplication factor, the delayed neutron fraction and many other parameters related to reactor physics. This accuracy clearly stems from the high computational cost. For this reason, during its over 50 years of improvement, many techniques have been developed in order to bias the statistics towards tailored objectives. Introducing a weight w for each neutron that increases a tally, the analog transport sampling probabilities $\boldsymbol{p}$ can be modified without affecting the estimation of the parameters, as long as the following rule is followed:

$$w^0 \boldsymbol{p}_{unbiased} = w^* \boldsymbol{p}_{biased} \tag{2.79}$$

Where w^* is the neutron weight after the manipulation. Some of the most important "non-analog games" are summarized below [37]:

- Absorption and leakage replacement by weight reduction: the neutron can survive after an absorption or a leakage by adjusting its weight as follows:

$$w_i = w_{i-1}\frac{\sigma_{tot} - \sigma_a}{\sigma_{tot}} \tag{2.80}$$

$$w_i = w_{i-1}(1 - \boldsymbol{p}_{leak}) \tag{2.81}$$

Where the neutrons probability of escaping from a certain region, being R the distance to its boundary, is:

$$\boldsymbol{p}_{leak} = e^{-\int\limits_0^R \sigma(r)dr} \tag{2.82}$$

- Multiplication replacement by weight increase: only one neutron with a weight increased by ν survives, instead of sampling collisions for a number of neutrons and simulate different histories.

- Russian Roulette: for neutrons in low importance regions that have gone through several absorption replacements, the initial weight w^0 can be restored if it survives a sampling with this probability:

$$\boldsymbol{p}_{RR} = \frac{w}{w^0} \tag{2.83}$$

- Splitting: for neutrons in high importance regions, an increase in histories may be statistically advantageous, hence a branching in N daughters can be performed following a weight correction:

$$w_{split} = \frac{w^0}{N} \tag{2.84}$$

2.3.2 Stochastic Perturbation Theory

Another useful way of exploiting the neutron weights can be found in perturbation theory. In fact, several Monte Carlo codes have been recently employed for sensitivity/perturbation calculations, complementing the performance of deterministic codes [18], [2]. In this scenario, perturbations by a factor m in parameters like cross sections or transport distributions lead to altered sampling probabilities. To restore fair transport, the collisions are accepted with a probability $\boldsymbol{p}_a = \frac{1}{m}$, muck like in delta-tracking algorithms [38]. If both accepted and rejected collisions are scored and the neutron is allowed to continue its history with a modified weight, some information on the perturbed system can be retrieved. The distribution of the particles will in fact be equal between the two systems, but the modified weight distribution provides an unbiased estimator of the perturbed system flux.

A majorant cross section is defined as $\Sigma_M = m \cdot \Sigma$, while the cross section of the perturbed system is $\Sigma^* = \Sigma + d\Sigma$. When a neutron undergoes a collision after a sampling of Σ_M, the probability of accepting the collision is imposed by the unperturbed system: $\boldsymbol{p_a} = \frac{\Sigma}{\Sigma_M}$. From the perturbed system point of view, in order to retrieve the weight of the neutron after an accepted collision, Eq. 2.79 is employed. The biased probability is represented by $\boldsymbol{p_a}$ and the unbiased one is $\boldsymbol{p_a^*} = \frac{\Sigma^*}{\Sigma_M}$. It follows that for positive perturbations:

$$w^* = w^0 \cdot \frac{\boldsymbol{p_a^*}}{\boldsymbol{p_a}} = w^0(1 + \frac{d\Sigma}{\Sigma}) \tag{2.85}$$

While for negative perturbations it will be: $w^* = w^0(1 - \frac{d\Sigma}{\Sigma})$. In this frame of mind, the weight of a neutron n can be expressed as a function of the weight of its ancestors (Figure 2.3). If the majorant factor is chosen to be $m = 2$, then positive and negative contributions will arise in the same proportion from accepted and rejected collisions respectively:

$$\boldsymbol{w_n^*} \simeq \boldsymbol{w_n^0} \cdot \left(1 + \frac{d\Sigma_{n,2n}}{\Sigma_{n,2n}}\right) \cdot \left(1 + \frac{d\Sigma_s}{\Sigma_s}\right) \cdot \left(1 - \frac{d\Sigma_f}{\Sigma_f}\right) \cdot \left(1 + \frac{d\Sigma_s}{\Sigma_s}\right) \cdot \left(1 - \frac{d\Sigma_c}{\Sigma_c}\right) \cdot \\ \cdot \left(1 + \frac{d\Sigma_f}{\Sigma_f}\right) \cdot \left(1 + \frac{d\Sigma_s}{\Sigma_s}\right) \cdot \left(1 - \frac{d\Sigma_c}{\Sigma_c}\right) \cdot \left(1 + \frac{d\Sigma_f}{\Sigma_f}\right) \cdot \ldots$$

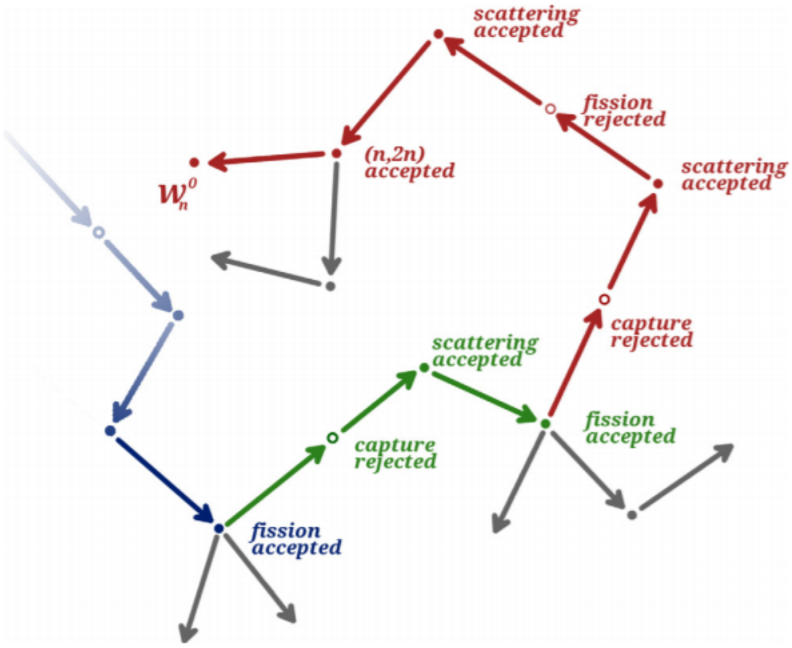

Figure 2.3: Accepted and rejected collisions in the history of a neutron, with different colours highlighting different generations

By first order expansion it follows that:

$$\frac{w_n^* - w_n^0}{w_n^0} \simeq \frac{d\Sigma_{n,2n}}{\Sigma_{n,2n}} + \frac{d\Sigma_s}{\Sigma_s} - \frac{d\Sigma_f}{\Sigma_f} + \frac{d\Sigma_s}{\Sigma_s} - \frac{d\Sigma_c}{\Sigma_c} + \frac{d\Sigma_f}{\Sigma_f} + \frac{d\Sigma_s}{\Sigma_s} - \frac{d\Sigma_c}{\Sigma_c} + \frac{d\Sigma_f}{\Sigma_f} \dots \tag{2.86}$$

Dividing this by the relative change in cross section, only an algebraic sum of accepted and rejected collisions is left on the right hand side of equation 2.86. In this way, it is possible to estimate the relative change of the neutron n weight due to a perturbation in parameter x, by taking into account the collision history of all the parent neutrons between its own generation α and an ancestor generation $(\alpha - \lambda)$:

$$\frac{\partial w_n / w_n}{\partial x / x} = \sum_{g=(\alpha-\lambda)}^{\alpha} \left({}^{(n,g)}ACC_x - {}^{(n,g)}REJ_x \right) \tag{2.87}$$

This is a very elegant solution that is based on the assumption that if a parameter perturbation brings an increase in weight to some neutrons, then the neutrons with higher weight must have a net gain in accepted collisions in their history with respect to rejected ones. While if a neutron weight is negatively affected by parameter x, then higher weight neutrons will be the ones that rejected those collisions in their history.

2.3.3 Iterated Fission Probability

Iterated fission probability (IFP) is a purely stochastic method that provides an unbiased estimator of neutron importance [39]. If a neutron n is considered in generation α, after a certain number of generations γ, the progeny associated to n will attain a certain level. The value of this asymptotic population is the definition of iterated fission probability [40]. Accounting for implicit transport, the IFP estimator will consist on the sum over the daughter population $d_n^{(\gamma)}$ of the neutron weights, divided by the ancestor neutron weight w_n:

$$I^{(\gamma)} = \frac{1}{q' w_n} \sum_{k \in d_n^{\gamma}} w_k \tag{2.88}$$

Where the coefficient q' takes into account the source normalization between generations, that artificially manipulates the number of neutrons produced per fission in order to simulate the same number of histories per cycle:

$$q' = \prod_{j=\alpha}^{\alpha+\gamma-1} k_{eff}^{j} \tag{2.89}$$

The IFP estimator is employed to calculate adjoint weighed quantities as sensitivity coefficients and most importantly kinetics parameters (the deterministic definition is given in Appendix A). The IFP implementation in SERPENT associates two vectors to each neutron where the lifetime and delayed fraction of its ancestors are stored. These vectors are passed along between generations with the newest information replacing the γ^{th} preceding one. In the following sections, the implementation of IFP for the calculation of λ_{eff} and β_{eff} is shown.

Effective neutron lifetime

A stochastic definition of λ_{eff} is the average of all the neutrons lifetimes ℓ_n in a generation α weighed on the iterated fission probability after γ generations, and then normalized by k_{eff}:

$$\lambda_{eff} = \frac{1}{k_{eff}} \frac{\sum\limits_{n \in \alpha} w_n \cdot \ell_n \cdot I_n^{(\gamma)}}{\sum\limits_{n \in \alpha} w_n \cdot I_n^{(\gamma)}} \tag{2.90}$$

Employing equation 2.88, we can see that q' is the same for both numerator and denominator and the dependence on w_n is lost:

$$\lambda_{eff} = \frac{1}{k_{eff}} \frac{\sum\limits_{n \in \alpha} w_n \cdot \ell_n \cdot \left(\frac{1}{q' w_n} \sum\limits_{k \in d_n^\gamma} w_k \right)}{\sum\limits_{n \in \alpha} w_n \cdot \left(\frac{1}{q' w_n} \sum\limits_{k \in d_n^\gamma} w_k \right)} = \frac{1}{k_{eff}} \frac{\sum\limits_{n \in \alpha} \ell_n \cdot \left(\sum\limits_{k \in d_n^\gamma} w_k \right)}{\sum\limits_{n \in \alpha} \left(\sum\limits_{k \in d_n^\gamma} w_k \right)} \tag{2.91}$$

Since all the neutrons in generation γ have one and only ancestor in generation α, the first sum can be omitted. This is done by including ℓ_n in the second sum and calling it $\ell_k^{(-\gamma)}$, as the lifetime of the one α ancestor of neutron k in generation $(\alpha + \gamma)$:

$$\lambda_{eff} = \frac{1}{k_{eff}} \frac{\sum\limits_{k \in (\alpha+\gamma)} w_k \cdot \ell_k^{(-\gamma)}}{\sum\limits_{k \in (\alpha+\gamma)} w_k} \tag{2.92}$$

The estimator is the average neutron lifetime of the γ^{th} ancestor of the population normalized by k_{eff}. It will provide unbiased results as long as the convergence of the fission source has been reached and enough latent generations have been recorded. Even though only the lifetime of the oldest ancestor is used, the intermediate ones are stored in a vector in order have the chance to calculate λ_{eff} for the following generations.

Delayed neutron fraction

A stochastic definition of $\beta_{eff,j}$ is given by the IFP weighed sum of neutrons emitted from the j_{th} group with respect to the total production rate:

$$\beta_{eff,j} = \frac{\sum\limits_{n \in \alpha} w_n \cdot \delta_{j,g_n} \cdot I_n^{(\gamma)}}{\sum\limits_{n \in \alpha} w_n \cdot I_n^{(\gamma)}} \tag{2.93}$$

Where the Kronecker delta allows the sum only if the neutron group g_n is equal to j. As explained in the previous section, the summation can be focused on the daughter neutron k in generation $\alpha + \gamma$ by replacing g_n with $g_k^{(-\gamma)}$:

$$\beta_{eff} = \frac{1}{k_{eff}} \frac{\sum\limits_{k \in (\alpha+\gamma)} w_k \cdot \delta_{j,g_k^{(-\gamma)}}}{\sum\limits_{k \in (\alpha+\gamma)} w_k} \tag{2.94}$$

The algorithm can be simplified to obtain the total fraction simply by considering all delayed neutrons with a $\delta_n = 1$ and prompt neutrons with a $\delta_n = 0$.

Latent Generations

From now on, the index γ will be used to express the number of latent generations associated to the estimation of the adjoint flux with Eq. 2.88, while λ will be the generations employed to estimate weight derivatives via Eq. 2.87.

$$\lambda \xleftarrow{\quad \Phi \quad} \alpha \xrightarrow{\quad \Phi^\dagger \quad} \gamma$$

Being α always the generation where the quantities are being estimated, ancestor generations provide information on the forward flux through the derivatives of neutron weights, while daughter generations provide information on the adjoint flux, as the symmetry of the problem suggests. The total span of latent generations that are being followed will then be $\epsilon = \lambda + \gamma$.

2.3.4 GPT in SERPENT

Until now, classical perturbation theory was followed, leading to the definition of k_{eff} sensitivities. In the work of Gandini [1], we find one of the first "western" explanations of classical perturbation theory of nuclear reactor parameters, but most importantly, its extension to bilinear functionals. In his work, he arrives at a comprehensive definition of sensitivity coefficients by treating all the parameters as a ratio between two adjoint weighed quantities, which means allowing for perturbations in kinetics parameters (Appendix A) or the void coefficient. In order to underline the crucial steps and assumptions of this method, reaction rate ratios sensitivities are presented, allowing for better understanding of bilinear functionals.

k_{eff} **sensitivity coefficients**

As explained in the introduction, stochastic methods have joined deterministic ones in the calculation of sensitivity coefficients, following the collision history in the same way as the iterated fission probability (IFP) algorithm [20]. In order to present S_x^k estimation with stochastic methods, it is useful to split the numerator of Eq. 2.38 (reported below) into its three components and to analyze them one by one.

$$S_x^{k_{eff}} = \frac{\frac{dk}{k}}{\frac{dx}{x}} = \frac{< \Phi^{\dagger} | \frac{1}{k} \frac{\delta \hat{F}}{\frac{\delta x}{x}} \Phi > + < \Phi^{\dagger} | \frac{\delta \hat{L_a}}{\frac{\delta x}{x}} \Phi > + < \Phi^{\dagger} | \frac{\delta \hat{L_s}}{\frac{\delta x}{x}} \Phi >}{< \Phi^{\dagger} | \frac{1}{k} \hat{F} \Phi >}$$

The first term is related to fission events, and only perturbations in parameters x related to fission will contribute to its estimation. Analyzing the fission operator in section 2.1, it is clear that while it generates fission neutrons, it does not make the initiating neutrons disappear like the fission sampling does. For this reason, bearing in mind Eq. 2.87, only accepted collisions will help addressing the derivative of the fission operator, while the IFP (Eq. 2.88) accounts for the adjoint flux:

$$< \Phi^\dagger | \frac{1}{k} \frac{\delta \hat{F}}{\frac{\delta x}{x}} \Phi > = \left(\frac{1}{q' w_n} \sum_{k \in d_n^\gamma} w_k \right) \left(\frac{w_n}{q} \sum_{n \in \alpha} \sum_{g=(\alpha-\lambda)}^{\alpha} ({}^{(n,-g)}ACC_x) \right) \tag{2.95}$$

$$< \Phi^\dagger | \frac{\delta \hat{L}}{\frac{\delta x}{x}} \Phi > = \left(\frac{1}{q' w_n} \sum_{k \in d_n^\gamma} w_k \right) \left(w_n \sum_{n \in \alpha} \sum_{g=(\alpha-\lambda)}^{\alpha} ({}^{(n,-g)}ACC_x - {}^{(n,-g)} REJ_x) \right) \tag{2.96}$$

Much like in section 2.3.1, the two sums can be focused on the daughter generation $(\alpha + \gamma)$, and ${}^{(k,-\epsilon)}ACC_x$ is the number of collisions accepted by the $\lambda + \gamma$ ancestors of neutron k. The source normalization factor $1/qq'$ disappears since it is found in the denominator as well:

$$< \Phi^\dagger | \frac{1}{k} \frac{\delta \hat{F}}{\frac{\delta x}{x}} \Phi > = \sum_{k \in (\alpha+\gamma)} w_k ({}^{(k,-\epsilon)}ACC_x) \tag{2.97}$$

Rejected fission collisions don't affect the fission process and can rather be seen as rejected absorptions, so it is more appropriate to stack them in the second component. The loss term will in fact comprise only rejected collisions, since an accepted collision completely cuts the neutron history.

$$< \Phi^\dagger | \frac{\delta \hat{L_a}}{\frac{\delta x}{x}} \Phi > = \sum_{k \in (\alpha+\gamma)} w_k (-{}^{(k,-\epsilon)}REJ_x) \tag{2.98}$$

Since the scattering term does not comprise creations nor absorptions, following equation 2.87, both accepted and rejected collisions contribute to the estimation:

$$< \Phi^\dagger | \frac{\delta \hat{L_s}}{\frac{\delta x}{x}} \Phi > = \sum_{k \in (\alpha+\gamma)} w_k ({}^{(k,-\epsilon)}ACC_x - {}^{(k,-\epsilon)} REJ_x) \tag{2.99}$$

If a scattering reaction has a positive impact on reactivity, then accepting these collisions will lead to higher weights in daughters generations with respect to rejecting them.

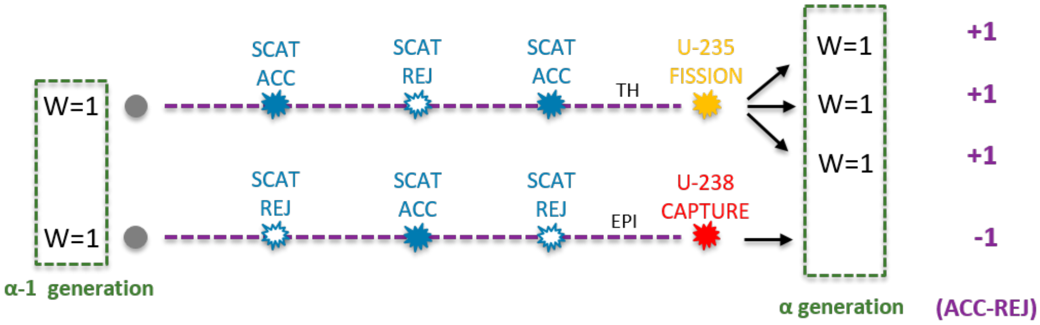

Figure 2.4: Collision history examples for 2 different neutrons

Finally, the denominator of equation 2.38 is the total neutron population that is born during the ϵ latent generations [18]:

$$< \Phi^{\dagger}|\frac{1}{k}\hat{F}\Phi >= \sum_{k\in(\alpha+\gamma)} w_k \tag{2.100}$$

This means that the k_{eff} sensitivity coefficient estimator is merely the expected value over the whole neutron population of the net gain rate of accepted and rejected collisions:

$$S_x^k = E[^{(-\gamma)}ACC_x -^{(-\gamma)} REJ_x] \tag{2.101}$$

By recording in an appropriate buffer the number of accepted and rejected collisions in a neutron history, the k_{eff} sensitivity coefficient can be retrieved by the simple weighted sum of these net gain rates.

In order to have a better physical understanding of this result, two examples of possible collision history paths have been traced in Figure 2.4. The two neutrons are born in generation α with a weight $w = 1$, and they both sample three scattering collisions in their initial path. Let's assume the first one only rejects one of the three scattering collisions, while the second one rejects two of them. we can imagine this would lead to the first neutron being more moderated with respect to the second one. The first neutron will therefore be more likely to cause a thermal fission on U-235, while the second one might be more likely to undergo an epi-thermal capture by U-238. In this way, the fission neutrons in generation α will contribute a net gain rate of $+1$, while the -1 contribution of the second neutron history has not made it into the next generation. From this we can retain the physical explanation for positive sensitivity of fission to scattering perturbations coming from the weight averaging of the net gain rate.

Chapter 3

Tools

This chapter presents all the computational tools specifically developed for the purpose of the present work. An available MCNP model of the RHF reactor has been accurately translated to SERPENT, in order to exploit the development of the SERPENT GPT routine [2]. Subsequently, the focus shifted to depletion perturbation theory. Since no DPT implementation is available in SERPENT, a simple deterministic transport code was developed from scratch in Python and called SIBYL. This allowed for a fast implementation of a DPT algorithm, named PTERODAx, to be coupled with SIBYL. The hypotheses behind these different tools, as well as their performance, are presented in the following sections.

3.1 SERPENT Model

The SERPENT model has been mainly developed with reactor elements as described in [5]. A detailed description of the RHF, as well as its MCNP and SERPENT models, has already been given in Section 1.2. This section focuses on the model's validation and uncertainty analysis.

The High Flux Reactor (RHF) at the Institut Laue-Langevin (Grenoble, France) produces, along with the Material Test Reactor at Idaho National Laboratory (US), the most intense thermal neutron flux in the world: $1.5 \cdot$

$10^{15}\frac{n}{cm^2 s}$, with a thermal power of 58.3MW. The reactor has only one fuel element, which is made of bent plates of highly enriched uranium, based on the Oak Ridge National Laboratory High Flux Isotope Reactor (HFIR) design, and is cooled and moderated by heavy water. It operates continuously for 50-day cycles, followed by a shutdown to change the fuel element. The neutrons are extracted from the pile using beam tubes and sent to instruments performing several kinds of scientific experiments ranging from physics to biology and medicine. The RHF is composed of three concentric regions. The heavy water tank has a diameter of 2.50 m and contains the fuel element. It is surrounded by a light water pool which has a diameter of 6 m and a height of 14 m. This pool is at the center of a 60 m wide containment building. The reactor is mainly used for fundamental research, employing 13 horizontal and up to 4 inclined beam tubes which extract neutrons. Hot and cold neutrons are produced by graphite and liquid deuterium volumes that are linked to particular beam tubes in order to provide a tailored energy flux to the instruments at the other end. In Figure 3.1, a reaction mesh plot highlights the structural materials surrounding the core. The SERPENT model has been mainly developed with reactor elements as described in [5]. The geometry involves beam tubes, sources and the heterogeneous core. Where some curved surfaces were not explicitly defined, or too cumbersome to implement, the principle of mass conservation was followed. This was especially true for the H5 beam and source, the hot source, and the vertical beam tubes tips. The heterogeneous core is modelled following a segment discretization of the involutes, but instead of polyhedrons, the volumes are made by annular sectors. This allowed to define 64 surfaces less and introduced a smaller error on the fuel volume (0.015% as opposed to 0.072%), but a bigger error on cladding and water volumes. The volumes were estimated through Monte Carlo simulation with relative uncertainty $<$1E-5.

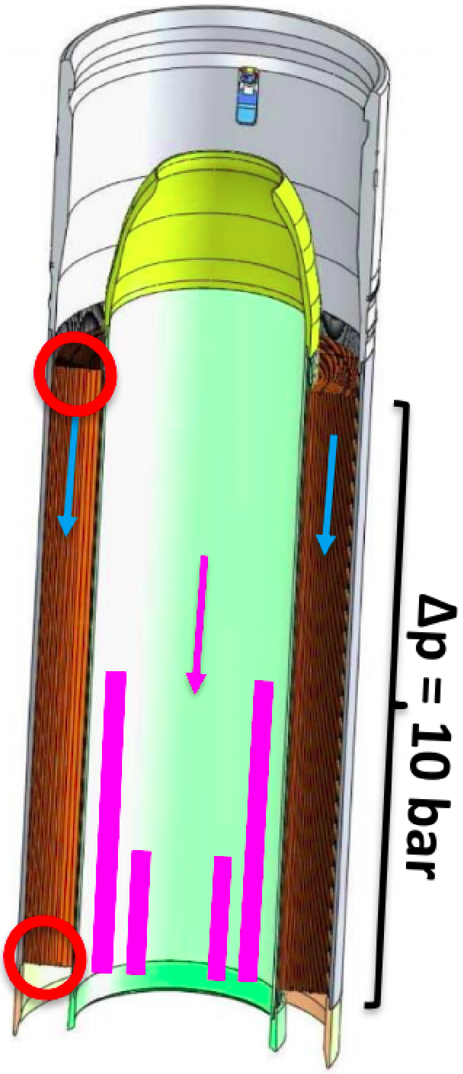

Figure 3.1: Fuel element vertical section. The control rod (pink) is extracted downwards and causes two hotspots (red) at the fuel extremities

Fuel

The RHF has only one fuel element which is made of 280 curved plates welded to two concentric aluminium tubes. Its internal and external diameters are 26.08 cm and 41.36 cm, respectively. The CERCA, ("Compagnie pour l'Etude et la Réalisation de Combustibles isotopiques", AREVA group) is the manufacturer of all the fuel plates and elements. All of the curved plates have been bent into an involute shape with a radius of 13.681 cm. The undoubted advantage of the involute shape is to maintain a constant distance between the plates and thus ease the thermo-hydraulic aspects related to non homogeneous cooling (Figure 3.2). The distance between two fuel plates is 1.8 mm.

Each fuel plate has a total height of 90.3 cm. The fissile part of the plates is made of a 93% enrichment U-Al-x powder. The nominal height of the meat is 80 cm. The manufacturing process (hot rolling) brings a non negligible uncertainty of 1.3cm on the meat height. Because the hot rolling is made in one direction, the margins are different at the top (0.95 cm) and at the bottom (0.35 cm) of the meat. This asymmetry is compensated by the chosen position of the meat inside the plate. As a result the meat mid plane is strictly the core mid plane: The nominal meat distribution is thus 40 cm above and 40 cm below the core mid plane. The meat is limited by two borated caps at both ends, as shown in pink in Figure 3.2.

The borated caps have a burnable poison role at the beginning of the cycle but also allow for a better control of the control rod. Each plate is composed of a 0.51 mm thick meat and of an Al-Fe-Ni cladding thickness of 0.38 mm on both sides of the plate. The overall fuel plate thickness is 1.27 mm before bending. However, once the plates are bent and assembled in the fuel element, the water channel thickness may vary by 0.3 mm locally and by 0.25 mm on average. These values are manufactring specifications that are controlled with very high accuracy by CERCA.

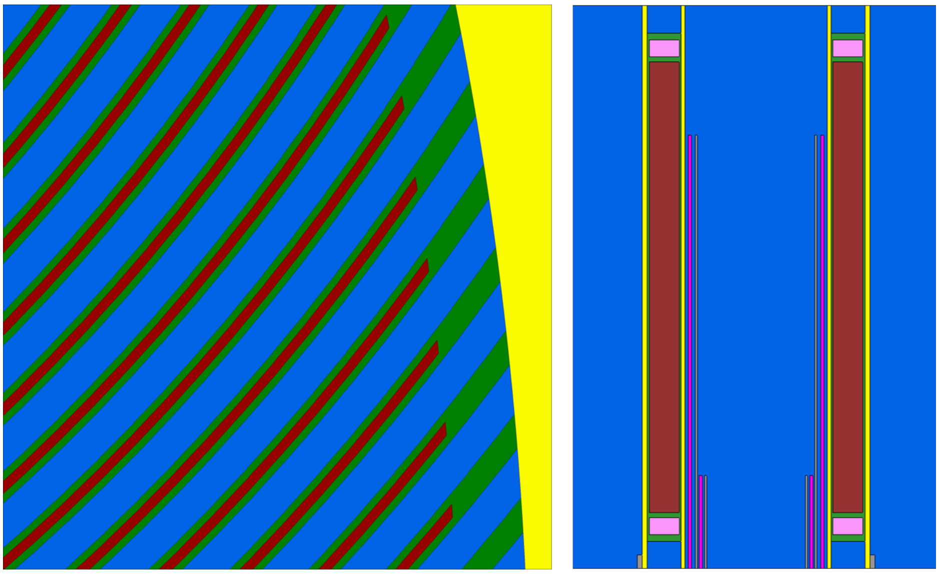

Figure 3.2: Fuel plates detail and vertical core section

Control Rod

The reactor is controlled by the motion of an absorbing cylindrical control rod (CR) placed in the fuel element ring (Figure 3.3, left picture in pink). This control rod is made of two pairs of tubes, each one has an outer absorbing tube of Nickel and an inner Aluminium tube. The first pair has a height of 105.5 cm, the second one has a height of 45 cm. The thickness of the Nickel tubes is 6 mm, while the Aluminium one is 4 mm. The smallest control rod provides a reactivity margin of 2000 pcm imposed by the safety authority. The moving mechanisms are set up below the fuel element.

The starting position of the control rod was chosen to be fully inserted into the fuel element, in order to facilitate its replacement. At the end of a cycle the whole control rod is out of the fuel element and below it, the thermal spike that this originates at BOC is balanced by the cold leg being positioned above the core. During the cycle both control rods move down together, at the same rate. The calibration of both control rods was carried out during the FOEHN experiment [41].

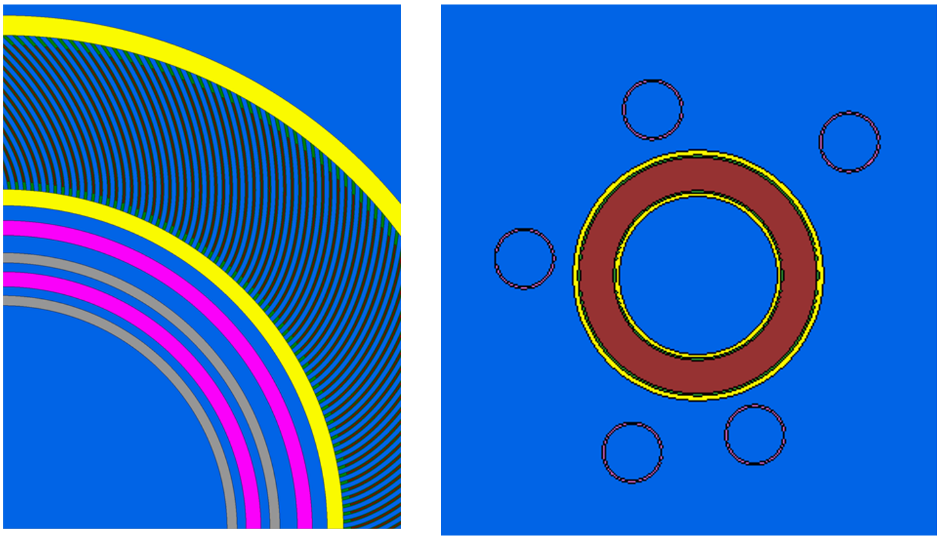

Figure 3.3: Control rod and safety rods inserted position

Safety rods

Five safety rods (SR) surrounding the core can shutdown the reactor at any time. These safety rods are made of a AIC alloy (Ag-In-Cd) tube. Each rod has a specific angle and position around the core (Figure 3.3, right picture). When fully inserted their bottoms lie at 40 cm below the reactor mid plane. When they are extracted their bottoms are 80 cm above the reactor median plane, with the same angle (Figure 3.1).

Sources

The aim of having a hot source in the reflector is to increase the thermal neutron flux between 0.15 and 1 eV in several beam tubes. It is made of a graphite cylinder (diameter 20 cm and height 30 cm) surrounded by a zircaloy wall (Figure 3.4, left picture). It could be heated by reactor radiation up to about 2400K, depending on the experiment. The hot source is set at a distance of 52cm from the fuel element axis, and its center is at 15 cm above the reactor median plane. There is no cooler for this source.
The two cold neutron sources (vertical and horizontal) aim to increase the

cold neutron fluxes (below 0.005 eV) in several beam tubes. They are reflectors made of liquid deuterium at 24 K. The temperature is controlled by deuterium vapour pressure. Liquid deuterium was chosen for its high thermalizing power and low neutron absorption. In both cold sources, the liquid deuterium is contained in an Al shell which is isolated from the heavy water pool by a zircaloy vessel under vacuum (Figure 3.4, right picture). The main role of these vacuum volumes is to act as thermal insulators.

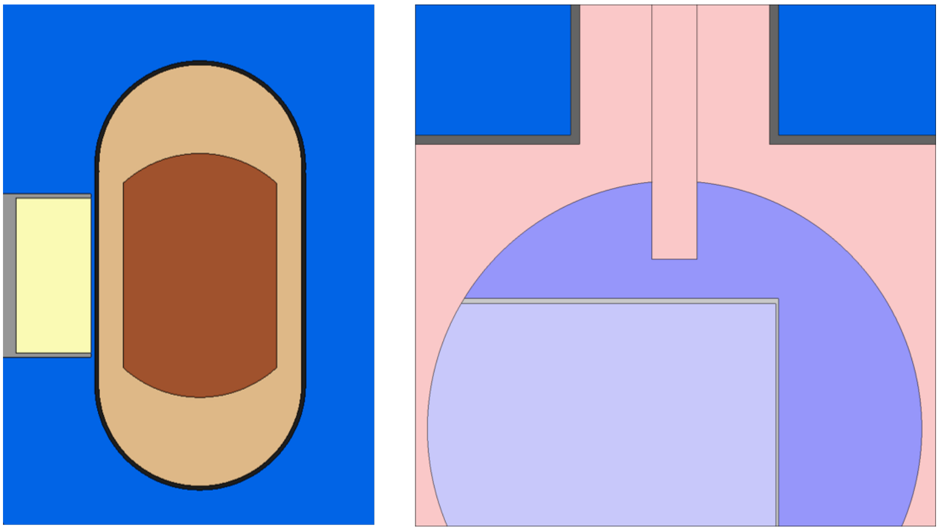

Figure 3.4: Vertical hot and cold source detail

Beam tubes

The 17 beam tubes are divided in three categories: the horizontal beam tubes ranging from H1 to H13, the inclined IH3 and IH4 beam tubes and the experimental canals V4 and V7. H10 is the only beam lying on the reactor midplane and the one whose flooding is considered in the core safety studies. H1 is the most involved in the vertical cold source thermalization, and along with H2, feeds the majority of the experiments taking place at the ILL. The hot source feeds simultaneously H3, H4 and H8, while the horizontal cold source lies inside H5. Due to their very close position to the core, both V4 and V7 are internally cooled by water. An horizontal mesh plot is reported

Figure 3.5: Horizontal capture reactions mesh plot

in Figure 3.5 to show the entanglement of the neutron extraction process.

Thermal-Hydraulics

The 2006 experiment that validates the model is conducted in a zero power regime (about 9W), at a temperature of 294K. The pump is operating at its nominal power, providing a coolant velocity over 17 m/s. The feed water pipe is situated above the core. The downwards flow of the cooling water helps to balance the power asymmetry in the axial direction caused by the progressive downwards extraction of the Control Rod. The heavy water is discretized into 5 regions in order to account for the pressure gradient (Table 3.1). The huge pressure loss over the coolant channel is a combined effect of the very high coolant velocity, that needs to cope with more than 50MWth produced by the HEU in less than 1 meter, and the big hydraulic diameter given by the very thin section of the coolant channel.

Region	Pressure
Reflector	4 bar
Above core	14.5 bar
Coolant Channel (average)	9.25 bar
Below core	4 bar
Control rod channel	4 bar

Table 3.1: Heavy water pressure in the five modeled regions

3.1.1 Validation

The validation was carried out by means of the 2006 experimental framework. Seven critical calculations were performed with different safety rods inserted and the control rod positioned to assure criticality. Both MCNP and SERPENT ran 5000 histories of 30000 neutrons. The uncertainty on Monte Carlo calculations is of 8 pcm (Table 3.2).

Since the overall k_{eff} uncertainty due to the experimental data was estimated to be around 200 pcm (Table 3.3), almost all results are within a 3σ interval, while the SERPENT k_{eff} seems to be about 150 pcm below the MCNP one.

An unexpected 400 pcm mismatch is recorded for the SR4 inserted configuration, which shields the region occupied by the vertical cold source, H1 and H2. The libraries for the 24K cross-sections are not used in this work, but it is difficult to say whether they could explain this outlier.

3.1.2 Uncertainty analysis with GPT

The main experimental uncertainties for the RHF (Table 3.3) have been evaluated at the ILL with the MCNP6 benchmark model, validated with the 2006 and 2008 experiments [5]. In this frame of mind, the uncertainties

Configuration	CR position (cm)	MCNP k_{eff}	SERPENT k_{eff}
All SR withdrawn	-22.94	0.99427	0.99287
SR1 inserted	-52.06	0.99904	0.99790
SR2 inserted	-48.2	0.99697	0.99552
SR3 inserted	-48.88	0.99721	0.99499
SR4 inserted	-49.93	0.99944	0.99540
SR5 inserted	-45.73	0.99793	0.99729
SR1+SR2 inserted	-67.95	0.99808	0.99653
SR1+SR5 inserted	-87.05	0.99866	0.99800
SR1+SR4 inserted	No criticality	-	-

Table 3.2: SERPENT model validation with 2006 experimental data and MCNP benchmark

estimated with GPT in the code SERPENT 2.1.29. [2] have been compared with SERPENT and MCNP direct calculations. Some examples are shown in this section, where the stochastic uncertainty in the GPT scoring algorithm is below 15 pcm, while for direct calculations it is always of 8 pcm.

Tolerances	SERPENT GPT	SERPENT direct	MCNP direct
D_2O composition	127	114	122
CR Thickness	104	105	97
Al-fe-ni density	101	95	110
Coolant thickness	56	64	65
Others	34	30	23
Total	**197**	**195**	**203**

Table 3.3: Main k_{eff} uncertainties related to experimental data

The GPT tool provides a satisfactory estimation of uncertainties for most tolerances of practical interest for the High Flux Reactor. This important result, gathered during the master thesis [26], will be exploited in Chapter 4 in order to perform a preliminary uncertainty analysis on two different RHF special configurations

3.2 SIBYL

SIBYL (Scaling Incertitudes BY modeLing) is a 3 regions neutronic model, that has been refined over time in order to provide a fast and intuitive framework for learning the ropes of Depletion Perturbation Theory.

Starting from a 0 dimensional model that would reproduce the results from Williams [3], the study evolved into a 3 regions model to allow for perturbations coming from outside the fuel (Figure 3.6). This can be very useful for such applications as the High Flux Reactor (RHF), which comprises control rods and burnable poisons that are separated from the fuel region. The same cylindrical framework has then been adapted to the LWR-UAM fuel pin benchmark for algorithm validation and comparison.

3.2.1 Mathematical framework

In order to underline the equations behind the SIBYL model, the steady-state transport equation for the flux $\Phi(r, E, \Omega)$ is reported from the previous chapter, with reaction type subscripts that have been moved to superscripts:

$$\begin{split}\Sigma^{tot}\Phi + \mathbf{\Omega}\mathbf{\nabla}\Phi - \int\int \Sigma^{s}(\boldsymbol{r};[E',\Omega'] \rightarrow [E,\Omega])\Phi(E',\Omega')dE'd\Omega' + \\ -\frac{1}{k}\int \Sigma^{f}(\boldsymbol{r},E')\nu(E')\frac{\chi(E)}{4\pi}\Phi(E')dE' = 0 \quad (3.1)\end{split}$$

Where the isotropic fission hypotheses has been employed. Now the equation can be integrated over the phase space, and weighed over the flux:

$$\begin{split}\int\int\int\Bigg[\Sigma^{tot}\Phi + \mathbf{\Omega}\mathbf{\nabla}\Phi - \int\int \Sigma^{s}(\boldsymbol{r};[E',\Omega'] \rightarrow [E,\Omega])\Phi(E')dE'd\Omega' + \\ -\frac{1}{k}\int \Sigma^{f}(\boldsymbol{r},E')\nu(E')\frac{\chi(E)}{4\pi}\Phi(E')dE'\Bigg] dVdEd\Omega\cdot = 0 \quad (3.2)\end{split}$$

At this point, some sort of discretization is usually carried out. For this specific problem, the following number of regions and energy groups has been chosen:

- 3 homogenized regions with indexes i,h = 1,2,3
- 44 energy groups with indexes j,k = 1,2,...,44

Three regions are the minimum amount required to capture the physics of the RHF as described in Chapter 1, while 44 energy groups are the minimum amount required to access internationally accepted covariance data.

In this way, Eq. 3.1 has its numerical representation in matrix form: $B_{ijhk}\Phi_{ij} = 0$, with $\Phi_{ij} = \int\int \Phi(r, E)dV_i dE_j$. The neutron balance for region V_i and energy E_j satisfies:

$$(\Sigma^{c}+\Sigma^{f})_{ij}\Phi_{ij}+\sum_{h=1}^{3}(\Sigma^{c}_{hi,j}\Phi_{hj}-\Sigma^{RC}_{ih,j}\Phi_{ij})-\sum_{k=1}^{44}(\Sigma^{s}_{i,kj}\Phi_{ik}-\Sigma^{s}_{i,jk}\Phi_{ij})-\frac{1}{k}\sum_{k=1}^{44}(\Sigma^{f}\Phi\nu)_{ik}\chi_{ij} = 0 \quad (3.3)$$

And each term has the following definition:

$$\int_{V_i}\int_{E_j}\Sigma^{tot}\Phi(r,E)dVdE = (\Sigma^c+\Sigma^f)_{ij}\Phi_{ij} \tag{3.4}$$

$$\int_{V_i}\int_{E_j}\int_{4\pi}\boldsymbol{\Omega}\boldsymbol{\nabla}\Phi(r,E)dVdEd\Omega = \sum_{h=1}^{3}(\Sigma^c_{hi,j}\Phi_{hj}-\Sigma^{RC}_{ih,j}\Phi_{ij}) \tag{3.5}$$

$$\int_{V_i}\int_{E}\int_{E_k}\Sigma^s(\boldsymbol{r};E'\rightarrow E)dE'dVdE = \sum_{k=1}^{44}(\Sigma^s_{i,kj}\Phi_{ik}-\Sigma^s_{i,jk}\Phi_{ij}) \tag{3.6}$$

$$\int_{V_i}\int_{E}\int_{E_k}\Sigma^f(\boldsymbol{r},E')\nu(E')\frac{\chi(E)}{4\pi}\Phi(E')dE'dVdE = \sum_{k=1}^{44}(\Sigma^f\Phi\nu)_{ik}\chi_{ij} \tag{3.7}$$

Where Σ^c_{ij} and Σ^f_{ij} are respectively the averaged capture and fission cross-sections in region V_i and energy E_j; $\Sigma^s_{i,kj}$ is the scattering-matrix probability for a neutron in region V_i to move from any energy E_k to E_j, while ν_{ij} and χ_{ij} are respectively the average emitted neutrons and emission spectrum in region V_i at energy E_j.

Region crossing parameter

The peculiarity of this approximation lies in the leakage term, that can be treated as a neutron current, where inwards and outwards contributions are kept as separate integrals:

$$\int_{4\pi}\int_{V}\boldsymbol{\Omega}\boldsymbol{\nabla}\Phi dVd\Omega = \int_{4\pi}\int_{A}\Phi\boldsymbol{\Omega}\cdot\boldsymbol{dA}d\Omega = \int_{4\pi^+}\int_{A}\Phi\boldsymbol{\Omega}\cdot\boldsymbol{dA}d\Omega - \int_{4\pi^-}\int_{A}\Phi\boldsymbol{\Omega}\cdot\boldsymbol{dA}d\Omega \tag{3.8}$$

A "region crossing" parameter $\Sigma^{RC}_{ih,j}$ is defined as the neutron current, within the energy group E_j, flowing through the surface A_{ih}, that separates the regions V_i and V_h, all normalized by Φ_{ij} (Eq. 3.9). The integral that appears in the numerator of the region crossing parameter definition, can be calculated by SERPENT (using a surface detector "ds" with inwards and outwards current separation), as any other homogenized cross-section in the model. Unfortunately, SERPENT does not allow an axial discretization of this surface detector, preventing the definition of finer meshes with this method.

It must be noted that while $A_{ih} = A_{hi}$, $\Sigma^{RC}_{ih,j}$ and $\Sigma^{RC}_{hi,j}$ have different values and opposite direction. Since the gradient of the flux is zero except at the region boundary, the net current flowing from one region to the other accounts for the leakage term (Eq. 3.5). It is convenient to separate inwards and outwards currents in Eq. 3.8 (instead of just using the net current), in order to keep the dependency on the averaged fluxes of the two communicating regions. This bears the hypothesis that the neutron current in the outgoing direction is dependent only on the average flux of the starting region.

$$\Sigma^{RC}_{ih,j} = \frac{\int_{4\pi^+}\int_{E_j}\int_{A_{ih}} \Phi(\boldsymbol{r},E,\boldsymbol{\Omega})\boldsymbol{\Omega}\cdot \boldsymbol{dA} dE d\Omega}{\int_{4\pi}\int_{E_j}\int_{V_i} \Phi(\boldsymbol{r},E,\boldsymbol{\Omega}) dV dE d\Omega} \tag{3.9}$$

While this approach might intuitively resemble diffusion discontinuity factors [42], response matrices [43], a collision probability formalism [44], and the interface current method in particular [45], the final result is different. In this region crossing parameter definition, all angular and space dependencies are lost, meaning that the three regions are treated as independent, with no shape or orientation towards each other, only connected by a single current, like a "neutron tube" for each energy group.

Transport Matrix

The Matrix B_{ijhk} is shown in Fig.3.6 in 2D format for a LWR fuel pin. The equations follow a region-wise order, with decreasing energy within the three blocks. The main diagonal comprises the absorption term in Eq. 3.4, the out-scattering term in Eq. 3.6, and the region leaking term in Eq. 3.5, while the region entry terms of the same equation appear in the smaller diagonals. The blurry cloud around the main diagonal are down scattering terms (above) and up-scattering terms (below). The fission spectrum terms occupy the upper left part of the matrix. These 3 regions model allows for an easy definition of lumped quantities in Monte Carlo, while preserving the heterogeneity of the model.

For a maximum agreement with the full 3D model SERPENT simulations, a homogenized cross-section correction can be switched on in order

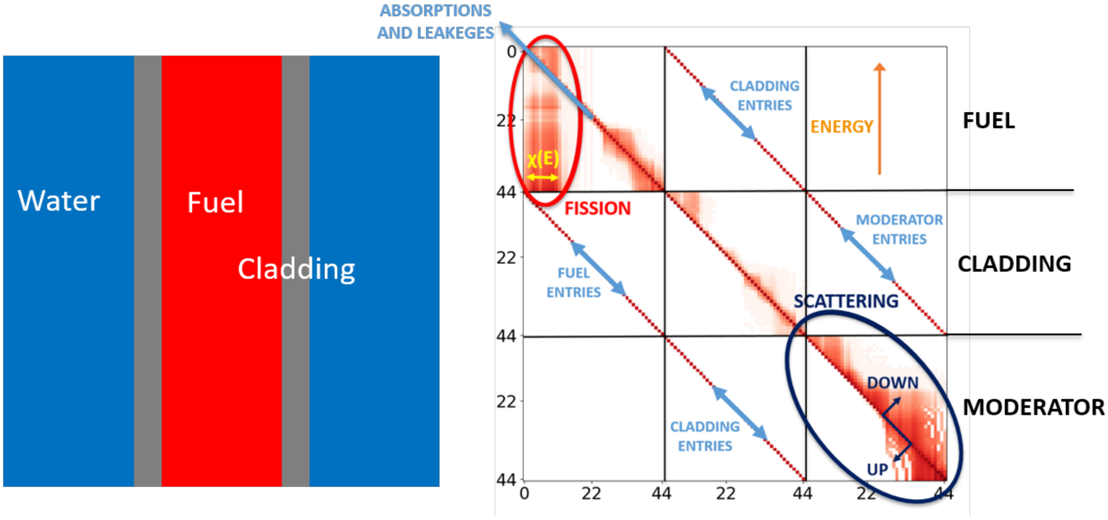

Figure 3.6: Transport matrix for a LWR fuel pin model with 3 regions and 44 energy groups

to compensate for nuclear data evolution and heterogeneities (for example burnable poisons, control rods, or other absorbers with strong self-shielding). The results are in Figure 3.18 underline the accuracy of SIBYL in reproducing the flux, the multiplication factor evolution, and the burnup of the main nuclides contributing to reactivity.

3.2.2 Python architecture

A flow chart showing the different blocks around the SIBYL algorithm is shown in Figure 3.7. The SERPENT calculation yields all the necessary data for: nuclide concentrations, homogenized cross-sections, scattering matrices, region crossing probabilities. The open source package SERPENT-Tools is used to extract the data [46]. The script *nucData.py* handles all the data from SERPENT and builds an object-oriented structure for all the nuclides included in the calculation, and a cross-section dictionary that is fed to SIBYL. An additional script called *SERPENT.py* is used to easily switch between different pre-defined SIBYL models and to account for different model peculiarities. For example, different subsets of nuclides can be used for different models approximations by entering a 10-15 line "card" for each SIBYL model that is to be paired to a SERPENT calculation.

Once all the data is gathered from SERPENT, the SIBYL algorithm gets into the main depletion loop inside *step.py*. For each of the n time steps, *sibyl.py* handles transport equation and flux normalization, while the open source package *SALAMECHE* is employed to build the full Depletion matrix, carrying all decay ancestors and daughters, and to solve the Bateman equation employing a CRAM implementation [6]. SALAMECHE coupled with SIBYL can track over 1400 nuclides for comparison and validation of depletion results with SERPENT, but for most DPT applications, a shortlist of 20 fission products is enough to grant accurate results on the most important perturbations. The disagreement in Samarium density probably comes from different handling of the Promethium decay chain between SERPENT and SALAMECHE, which has not been resolved yet. All along the cycle, the relevant results are made available for post-treatment and for coupling with PTERODAx.

Configuration inputs

The different input parameters for a SIBYL direct calculation are listed in Table 3.4, and they are entered in a specific *configfile* by the SIBYL user. The possible inputs comprise two energy grids, arbitrary time step and cycle lengths and three different kinds of discretization schemes, which will be discussed in section 4.3. The "Model" input allows switching between models in *SERPENT.py*, as previously mentioned. Additional features can be switched on and off before the calculations: one for switching between a user-defined short-list of nuclides to the full 1000+ depletion matrix comprising all fission products, one for correcting the cross-section of some specific nuclides who are misrepresented by the homogeneous approximation, and one for employing a criticality reset at each time step. The criticality reset is a feature that pertains to the RHF model, not the UAM benchmark (section 2.4). SALAMECHE coupled with SIBYL can track over 1400 nuclides

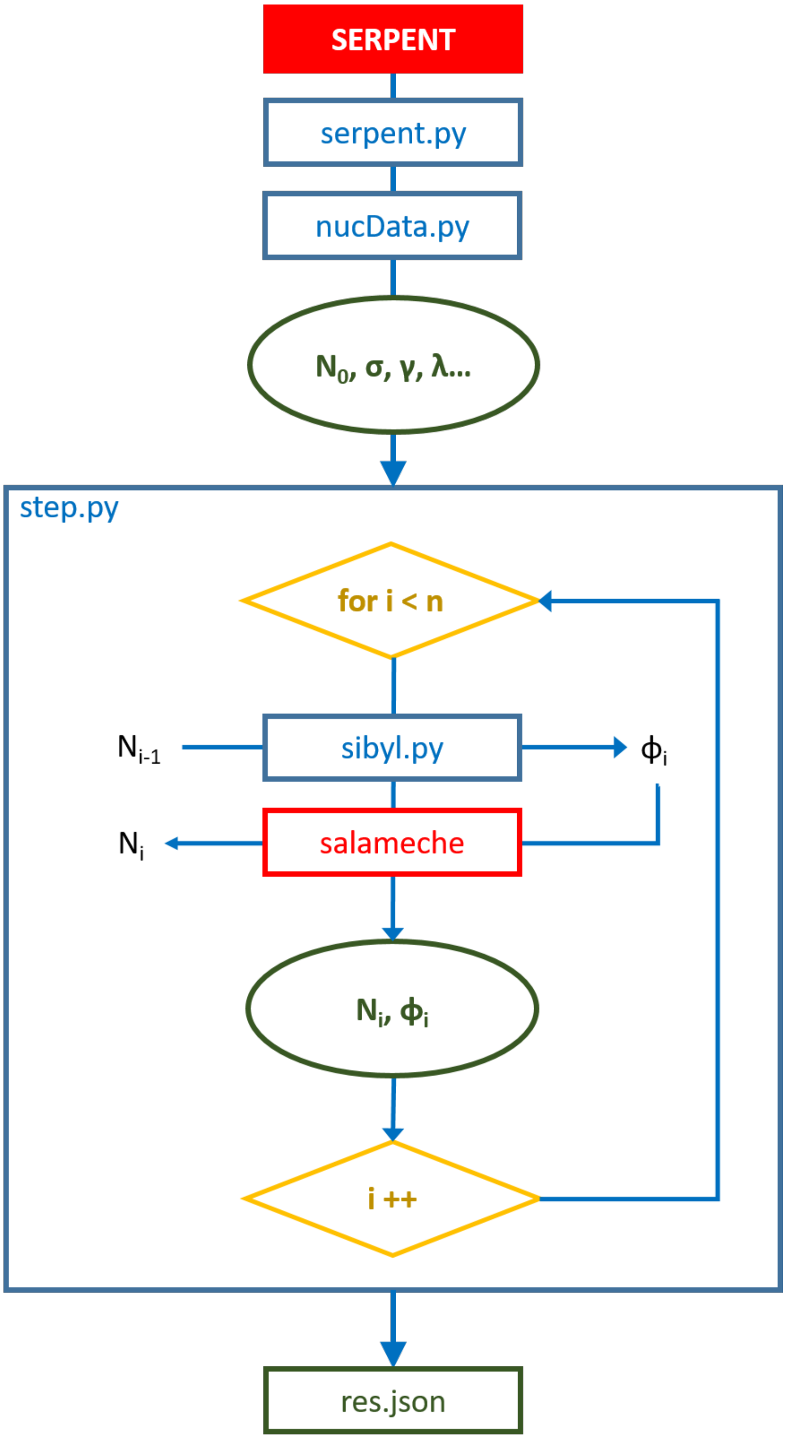

Figure 3.7: Python architecture

for comparison and validation of depletion results with SERPENT, but for most DPT applications, a shortlist of 20 fission products is enough to grant accurate results on the most important perturbations.

Input parameter	Variable	Entries
Model	String	RHF-HEU, RHF-LEU, UAM
Energy groups	Int	2, 44
Time discretization	Int	0, 1, 2
Time step length [days]	Float	(RHF: 1, UAM: 25)
Full FP matrix	Flag	0, 1
Flux correction (boron)	Flag	0, 1
Criticality reset	Flag	0, 1

Table 3.4: SIBYL configuration input parameters

3.2.3 High Flux Reactor

The results shown in Figures 3.10 to 3.12 underline the accuracy of SIBYL in reproducing the flux, the multiplication factor evolution and the burnup of the main nuclides contributing to reactivity.

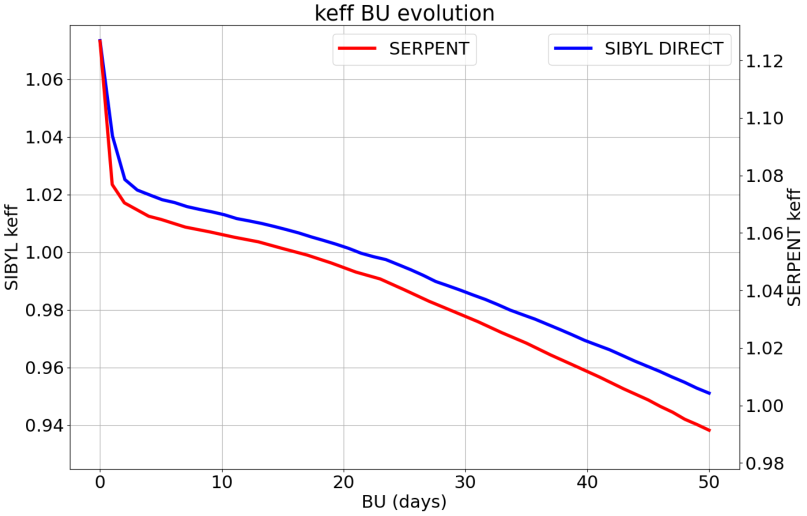

Figure 3.8: SIBYL results comparison with SERPENT: LEU multiplication factor evolution

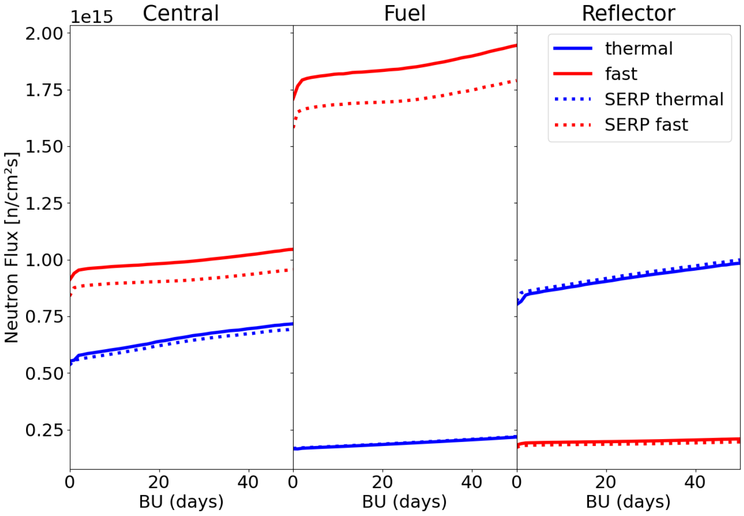

Figure 3.9: SIBYL results comparison with SERPENT: LEU 2 groups Neutron Flux evolution in the 3 regions

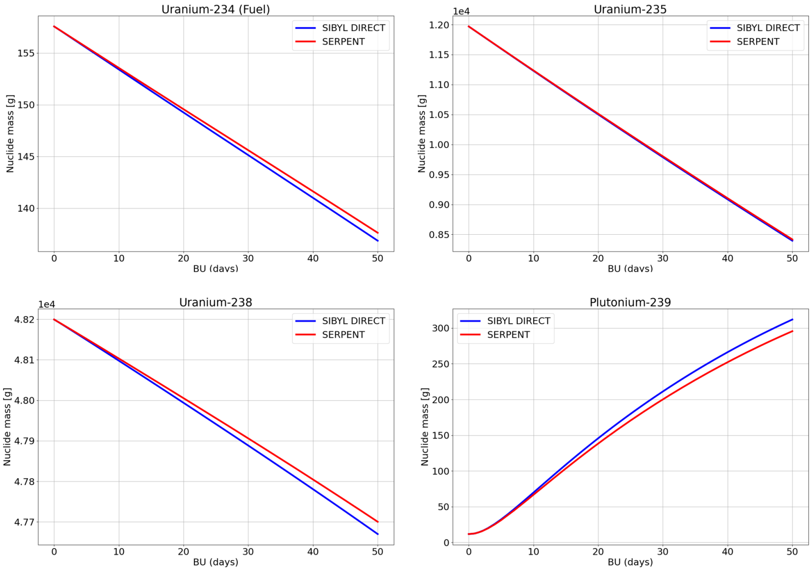

Figure 3.10: SIBYL results comparison with SERPENT: LEU actinides evolution

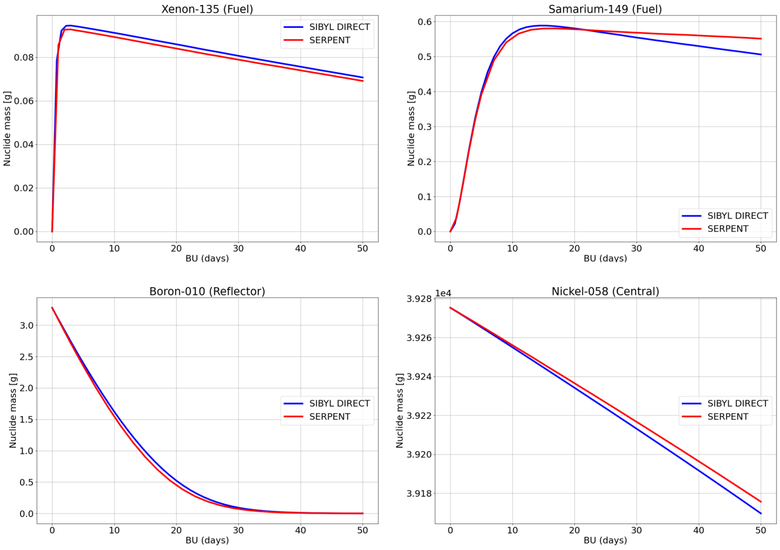

Figure 3.11: SIBYL results comparison with SERPENT: LEU absorbers evolution

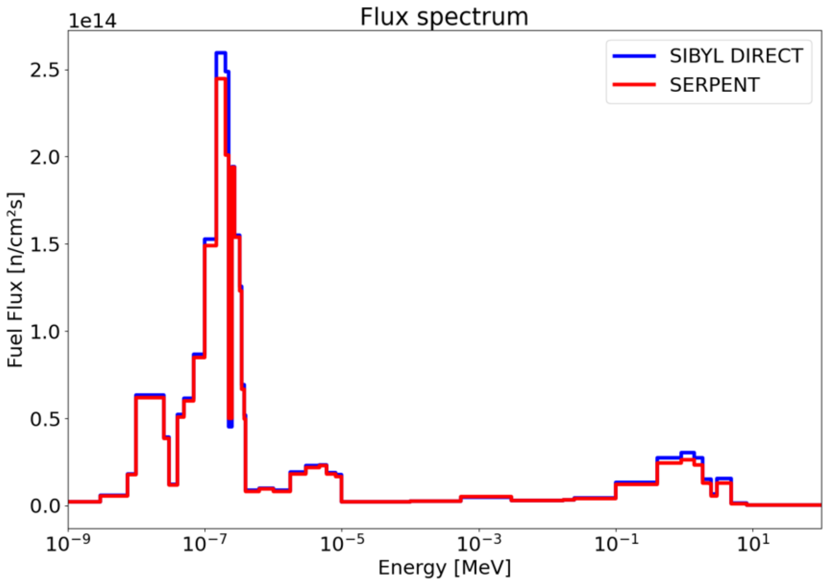

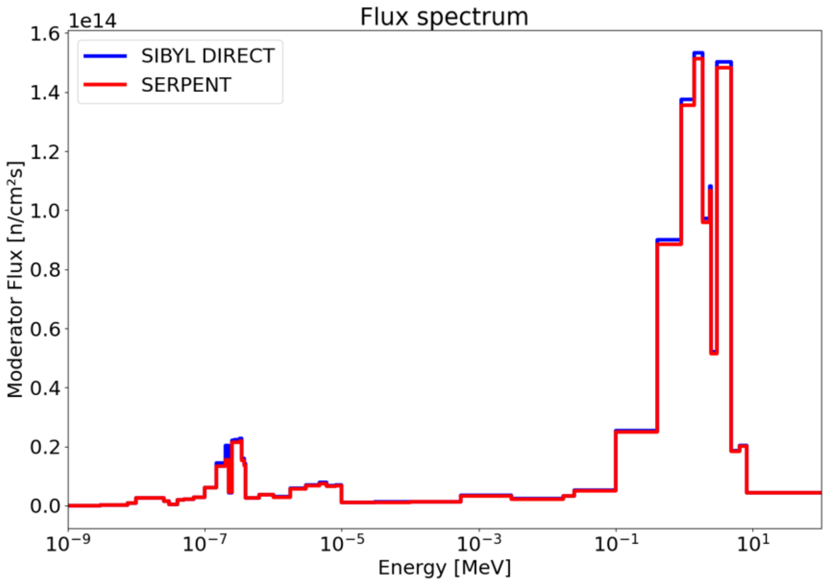

Figure 3.12: SIBYL results comparison with SERPENT: LEU 44 group flux per unit lethargy in the Fuel (top) and the Moderator (bottom)

Criticality reset

The three regions model has been specifically conceived to perform an easy criticality reset on the RHF model. The only Nickel control rod is extracted downwards during the cycle, until it completely exits the multiplication region and its differential reactivity per centimeter drops to zero. In SIBYL, The Nickel coming from the control rod is dispersed in the central homogenized region, and by adjusting its concentration at each step of the forward calculation, a constant multiplication factor is enforced. The resulting Nickel concentration is plotted in Figure 3.13, along with the critical control rod position coming from a SERPENT depletion calculation. The xenon jump at BOC takes most of the control rod margin, with a similar shape to the multiplication factor evolution in Figure 3.8. The Nickel concentration, on the other hand, shows a less pronounced Xenon jump, followed by a much higher degradation of the differential reactivity along the cycle. This difference is not surprising since the homogenized cross-section of the Nickel control rod shows a time evolution along with the extraction.

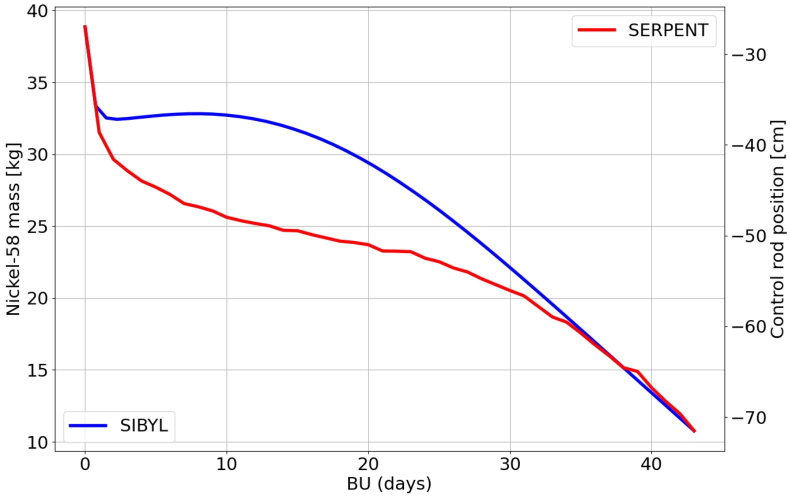

Figure 3.13: Criticality control with SIBYL and SERPENT

3.2.4 UAM benchmark

The results shown in Figures 3.14 to 3.17 underline the accuracy of SIBYL in reproducing the flux, the multiplication factor evolution and the burnup of the main nuclides contributing to reactivity. The disagreement in Samarium density is more pronounced with respect to the RHF due to the longer burnup.

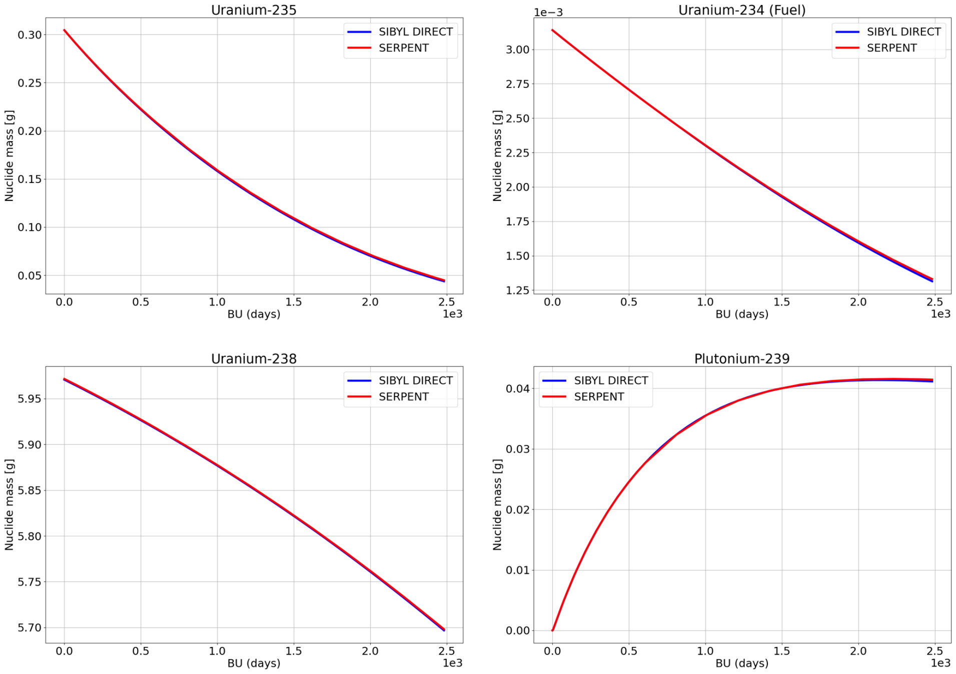

Figure 3.14: SIBYL results comparison with SERPENT: UAM actinides evolution

3.3 PTERODAx

The Depletion perturbation Theory solver is called PTERODAx (Perturbation Theory Engine for Reactor Outputs Depletion Analysis). Its algorithm involves writing an adjoint equation for the nuclide field N^* along with the more known adjoint transport equation for $\Phi*$, starting from the

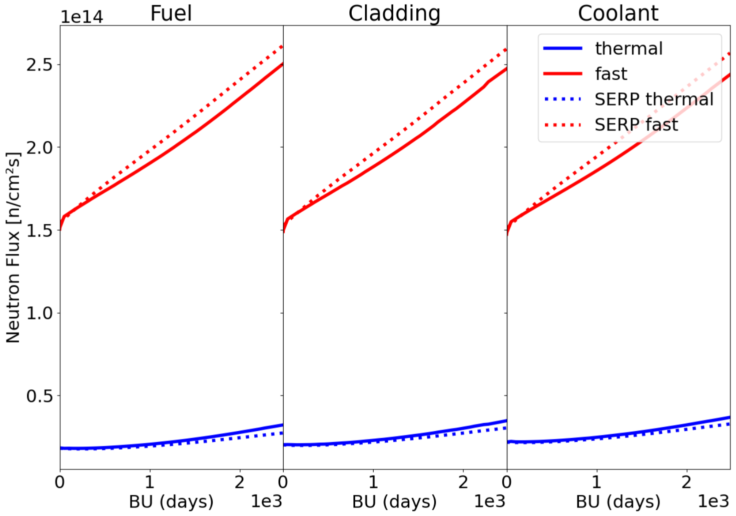

Figure 3.15: SIBYL results comparison with SERPENT: UAM 2 groups Neutron Flux evolution in the 3 regions

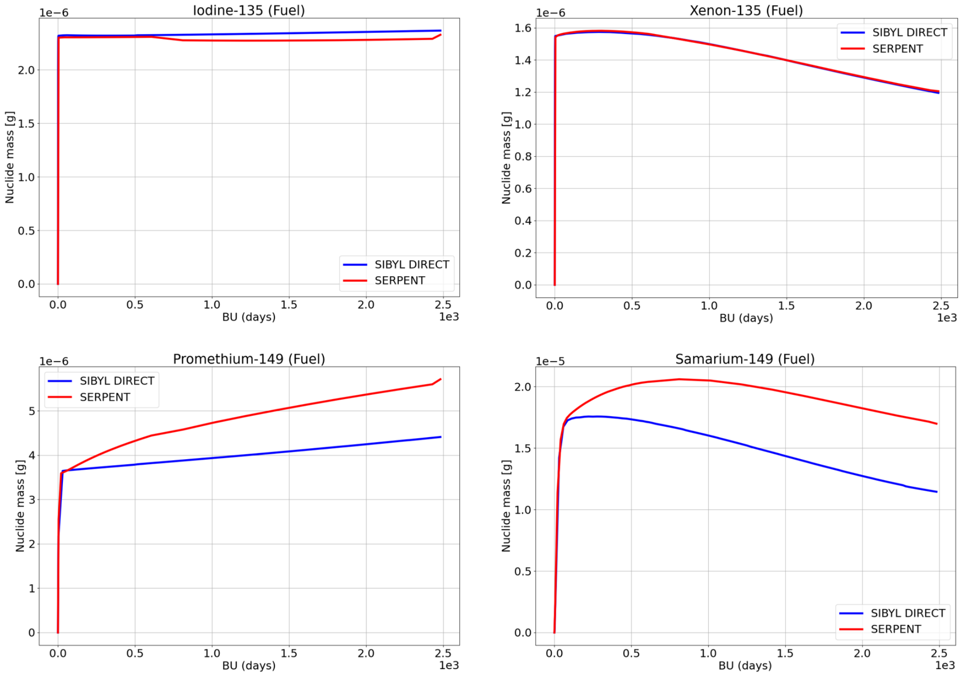

Figure 3.16: SIBYL results comparison with SERPENT: UAM fission products evolution

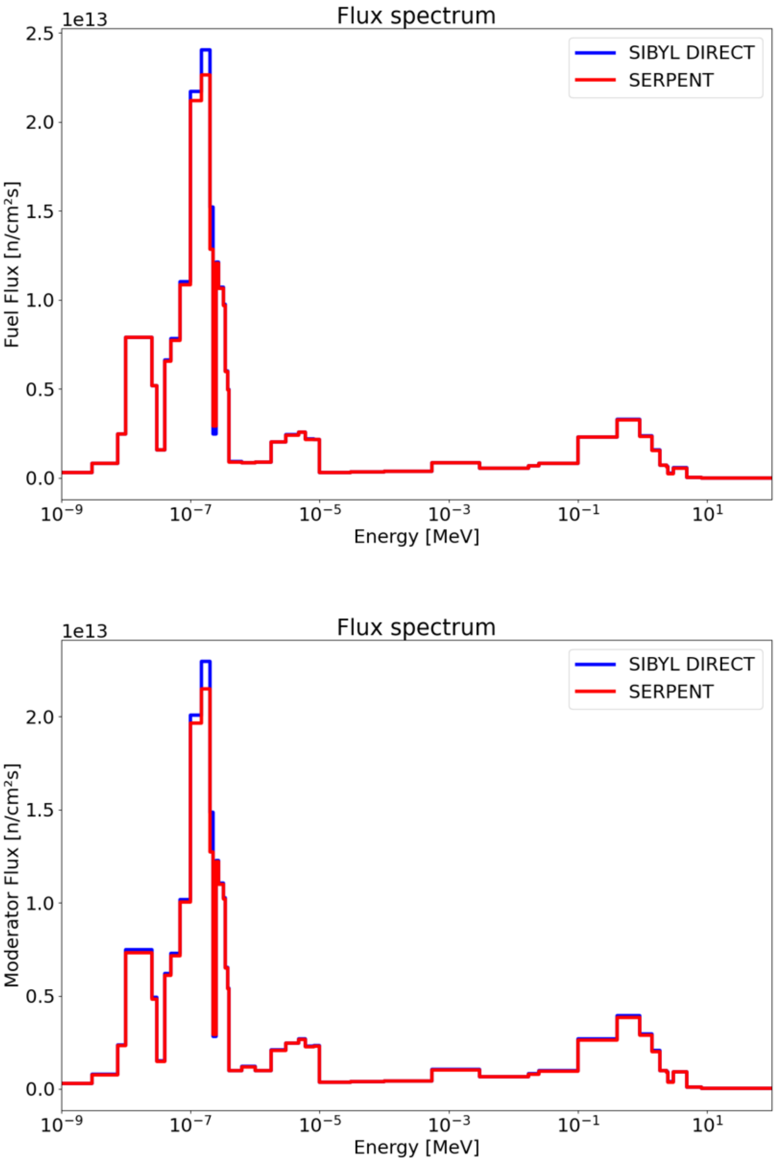

Figure 3.17: SIBYL results comparison with SERPENT: UAM 44 group flux per unit lethargy in the Fuel (top) and the Moderator (bottom)

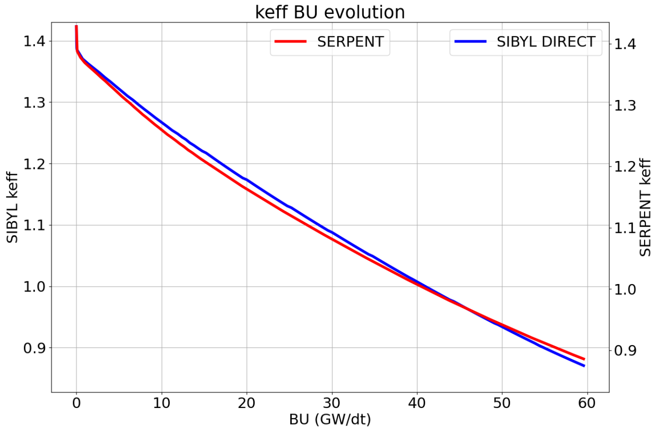

Figure 3.18: SIBYL results comparison with SERPENT: UAM multiplication factor evolution

transport solution at end-of-cycle and solving backwards in time to obtain the perturbed solution, as extensively shown in section 2.

3.3.1 Python architecture

The python architecture is shown in Figure 3.19. A PTERODAx calculation always needs to be based on a SIBYL forward calculation, since many direct quantities are also involved in the estimation of adjoint quantities. Once the desired response function is chosen, the final condition on the nuclide field N^* at $t = t_f$ is imposed by equation 2.50. The adjoint Bateman equation can easily be solved backwards by *SALAMECHE* again, once the direct depletion matrix is recovered from the *res.json* database and transposed into the adjoint one. The Lagrange multipliers stemming from DPT, such as P^*, Γ^*, are computed by *pterodax.py*. These multipliers, together with the depleted vector N_i^*+, will be used to enforce the jump condition on the updated value of N_i^*. Once the full cycle has been retraced backwards in time, the sensitivities coefficients of the selected response to the desired perturbed quantities can be computed. A typical PTERODAx result is shown in the next section, with a comparison to the direct SIBYL calculations.

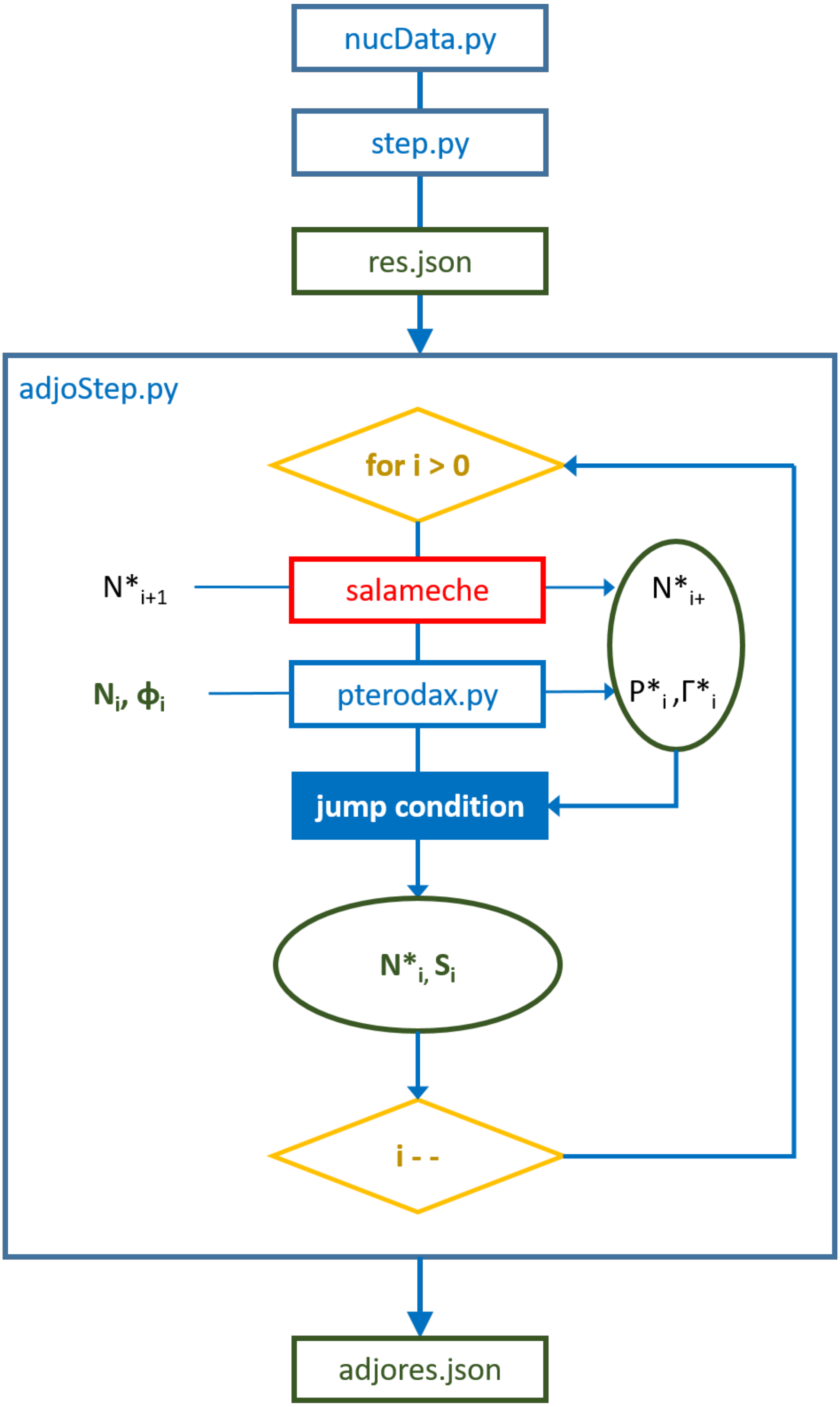

Figure 3.19: Python architecture

Configuration inputs

The different input parameters for a PTERODAx calculation are listed in Table 3.5, and they are entered in a specific *configfile* by the PTERODAx user. The user can choose between calculating a sensitivity coefficient to k_{eff} or to a nuclide density, specifying which nuclide has been selected. A list of most important perturbed nuclides can be entered in order to expedite the post-processing of sensitivities and various plots, but DPT will intrinsically calculate the necessary quantities for assessing all the nuclides involved in the SIBYL model. The perturbation can also involve the full energy spectrum of the sensitivity coefficients, instead of just the total nuclide density. In this case, the MT of the desired cross section to be perturbed also needs to be specified. If the user wishes to perform a set of direct perturbed calculations in order to verify the performance of PTERODAx by comparison, the perturbation magnitude for the direct calculations needs to be included. Finally, the PTERODAx sensitivities to cross-section perturbations can be exploited along with covariance matrices for uncertainty propagation, employing Eq. 2.78.

3.3.2 SIBYL comparison

The python architecture is shown in Figure 3.20: the SERPENT model feeds the necessary nuclear data to SIBYL, while the Bateman equations (direct and adjoint) are treated by SALAMECHE [6], a sub-routine of the open-source python package ONIX. This setup provides a small but accurate solver for the reactor burnup, whose calculation time is much shorter than Monte Carlo, making it ideal for learning the ropes of DPT. One PTERODAx backward calculation usually requires 2 to 5 times the amount of time used by the same single forward SIBYL calculation, which can range from a few seconds up to a few minutes (depending mainly on the number of steps, nuclides, and energy groups). This extra time factor is related to the computation of DPT contributions such as integrals, adjoint fluxes, or nu-

Input parameter	Variable	Entries
Response	String	None, keff, nuclide
Response nuclide	String	(nuclide ZAI)
Perturbed nuclide	List	(nuclide ZAI)
Cross-section perturbation	Flag	0, 1
Perturbed MT	String	18, 102, 402
SIBYL comparison	Flag	0, 1
Perturbation magnitude	Float	(1.01 default)
Uncertainty propagation (COVX)	Flag	0, 1

Table 3.5: PTERODAx configuration input parameters

merical derivatives (especially from multigroup calculations). While it might already be possible to reduce this difference by code optimization, it likely becomes less relevant whenever the depletion algorithm is coupled with more sophisticated transport codes.

In the Chapter 4, in order to test the performance of PTERODAx, multiple SIBYL direct calculations, in which some parameter α is perturbed, are used to obtain EOL plutonium densities, which are then compared with the sensitivities coming from a single nominal PTERODAx run.

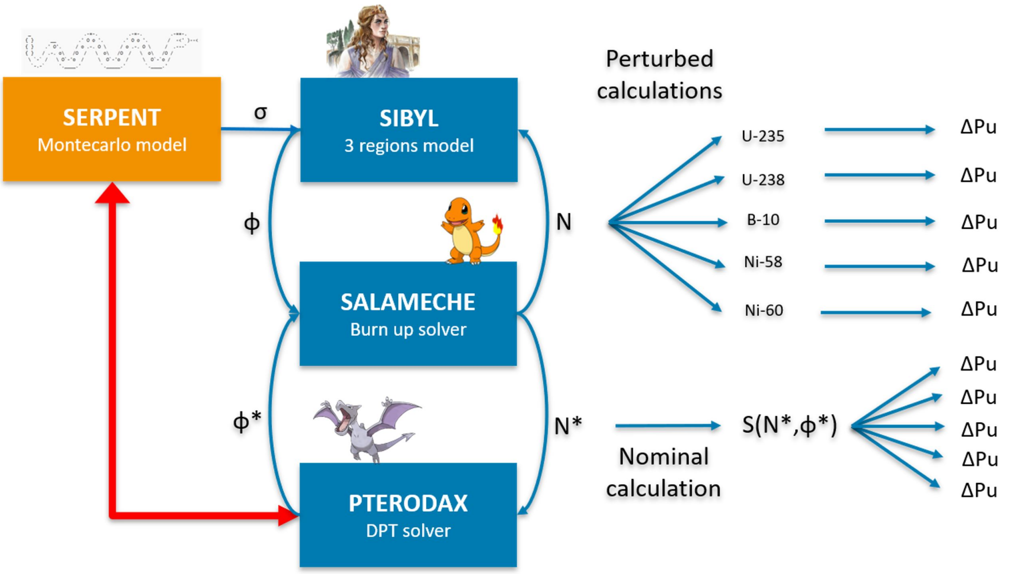

Figure 3.20: Python architecture

Chapter 4

Results

In this chapter, the strength of the generalized perturbation theory approach in SERPENT has been assessed by verifying, with direct calculations' comparison, the uncertainty results obtained with SERPENT. This analysis has shown to be very promising to improve uncertainty quantification, especially in study cases like the High Flux Reactor (RHF) [26].

The propagation of experimental uncertainties GPT has been subsequently applied to the accident scenario of a beam tube flooding in the RHF reflector pool. In this particular case, an EGPT approach has been employed in order to confront the uncertainties arising in the two different flooded and nominal configurations of the RHF.

Once this static uncertainties have been evaluated, the biggest focus of the project has been redirected to the assessment of uncertainties along the fuel cycle. This redirection is justified in the framework of the RHF conversion to Low Erniched Uranium fuel, raising the attention on actinides' buildup along the fuel cycle. During the first year of the PhD, an extensive sensitivity analysis has been performed on the burnable poison of the new LEU fuel, embracing the "uncertainty by design" approach on a crucial parameter for irradiation and thermal-hydraulics margins of the RHF core.

The extensiveness of the burnable poison engineering study, where almost 6 months were spent iterating configurations and performing simulations spanning several weeks, justified the methodological development of Perturbation Theory. It was believed that opening the access to time-dependent sensitivity coefficients would expedite some design optimization, while also anticipating most results of the uncertainty analysis that is usually performed on the finalized design.

Results on multiplication factor and Pu-239 density sensitivities are shown as the most relevant for this particular application, but the same results could be gathered for any other nuclide density. Similar studies to the ones performed on the RHF have successively been carried out on the UAM benchmark of OECD, in order to be compared with international participants' multiplication factor uncertainties

4.1 EGPT Uncertainty analysis

Equivalent generalized perturbation theory has been employed with the purpose of assessing the solidity of the RHF uncertainties. By comparing the estimation of k_{eff} model uncertainties obtained by GPT in different model configurations, it is possible to understand whether reactivity changes can be properly assessed by confronting different Monte Carlo simulations.

4.1.1 Beam flooding accident

The beam tube flooding reactivity worth is an interesting parameter in terms of the reactor safety, because for the neutron beam tube that lies on the reactor mid-plane (H10), it can account for an increase in reactivity over 500 pcm (direct calculation, [47]). Since this result is a comparison of k_{eff} Monte Carlo calculations, it is rather difficult to assess this scenario without addressing the contributors to the uncertainty.

GPT and EGPT [17] have been employed to investigate the sensitivity of heavy water inside the beam tube. The task appears to be computationally expensive (due to the small volume involved) and strongly dependent on the number ϵ of latent neutron generations employed. Results are further com-

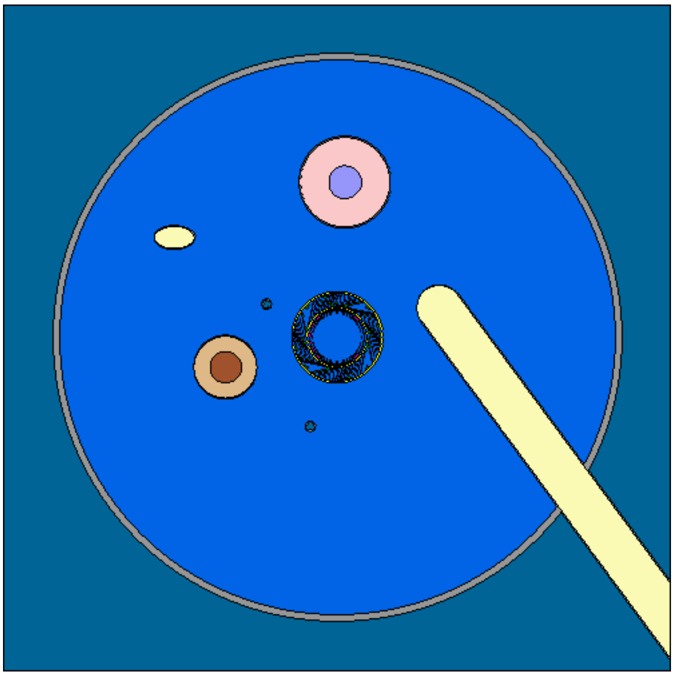

Figure 4.1: RHF median section H10 beam tube, cold source and hot source

plicated by the intrinsically non-linear behaviour of the reactivity worth with the level of beam tube flooding. This means that any sensitivity to the water inside the beam tube can not be used, on its own, to obtain the reactivity worth because of the linear assumptions made in Generalized Perturbation Theory. Since the differences in the uncertainties shown in Table 4.1 are always below 5 pcm with respect to the nominal values, we can affirm that the uncertainty on the reactivity change must be considerably lower than the experimental uncertainty and can not exceed a few tens of pcm. The sensitivity differences are so small to be comparable, in some cases, with the uncertainty on the single calculation, meaning that the study is not yet strongly conclusive but also that the differences must be indeed very little. This can be physically explained by the large amount of heavy water that characterizes this design, making the reflector not sensitive to smaller perturbations. These calculations were carried out during the master thesis, and then reprocessed along with the results presented in the following sections.

Material	**Perturbed Nuclide**	**Void**	**Flooded**	**std dev.**
D_2O (ref)	H-1	129	126	4%
D_2O (ref)	H-2	6	6	0.5 %
D_2O (CC)	H-2	56	55	0.5 %
Fuel	U-235	130*	133*	0.1%
Fuel	U-238	4*	4*	0.5%
Cladding	Al-27	101	102	2 %
Control Rod	Ni-58	90	89	0.3%
Boron caps	B-10	94*	94*	0.1%
	Total	**197**	**197**	

Table 4.1: Comparison of k_{eff} sensitivities between flooded and void H10 beam tube configuration

4.1.2 LEU Fuel

The EGPT study performed on the H-10 beam flooding scenario has been replicated on the RHF converted design. The uncertainties propagated via GPT computed sensitivities from SERPENT have been compared between the nominal HEU configuration and LEU converted configuration of the High Flux Reactor.

The results shown in Tables 4.2 and 4.3 refer to the reactivity uncertainties (in pcm) associated to the main fabrication tolerances of the two configurations. The uncertainties marked with an asterisk refer to a perturbation in single fuel plate fabrication tolerances. The independence of the manufacturing process for these plates allows for the normalization of their uncertainties by the square root of the total number of perturbed plates, $\sqrt{280}$ in this case, as by directives of the NEA [48]. This means that most uncertainties related to actinide masses, while significant in a singles plate analysis, get averaged out on the whole fuel element.

Material	**Nuclide**	**LEU**	**HEU**	**std dev.**
Fuel	Uranium-235	139^*	140^*	0 %
Fuel	Uranium-238	-48^*	-4^*	1 %
Fuel	Plutonium-239	0^*	0^*	28 %
Cladding	Aluminum-27	110	101	2 %
Reflector	Deuterium-2	7	8	4 %
Reflector	Hydrogen-1	-129	-126	23 %
Poison	Boron-10	-56	-94^*	0 %
Coolant	Deuterium-2	17	30	4 %
Coolant	Hydrogen-1	0	0	42 %
Control Rod	Nickel-58	-90	-98	1 %
	Total	**204**	**197**	

Table 4.2: k_{eff} uncertainties at day 0 [pcm]

The main difference between the two configurations comes from the displacement of the burnable poison from inside the plates to the outer tube, meaning that the normalization factor related to plate independence can no longer be employed for the LEU fuel. While the same tolerance HEU boron tolerance has been employed to perturb the new LEU burnable poison in Table 4.2, it is imaginable that the bigger mass employed in the burnable poison will bring CERCA to decrease the relative manufacturing tolerance on the component. Furthermore, the 50 pcm related uncertainty is only modestly contributing to the total result, because of the quadratic sum of the uncertainties.

Material	**Nuclide**	**LEU**	**HEU**	**std dev.**
Fuel	Uranium-235	183^*	209^*	0 %
Fuel	Uranium-238	-4^*	-4^*	1 %
Fuel	Plutonium-239	8^*	0^*	2 %
Cladding	Aluminum-27	101	110	2 %
Reflector	Deuterium-2	6	7	5 %
Reflector	Hydrogen-1	-127	-126	22 %
Poison	Boron-10	-1	-4^*	3 %
Coolant	Deuterium-2	15	27	4 %
Coolant	Hydrogen-1	0	0	75 %
Control Rod	Nickel-58	-13	-21	4 %
	Total	**163**	**163**	

Table 4.3: k_{eff} uncertainties at day 45 [pcm]

Shifting the attention towards the static uncertainties at the end of the RHF cycle in Table 4.3, it is clear how neither boron nor plutonium have any significant contribution. The boron poison has been designed to completely disappear along the cycle, while plutonium buildup stays fairly low for the RHF fuel, amounting to roughly 300g compared to an initial mass of 10 kg of U-235 with a burnup around 35%.

Since the integral sensitivity coefficients remain fairly constant for the RHF, it can be deduced that the uncertainties related to nuclear data will also remain virtually unchanged both along the cycle, and between HEU and LEU fuels. Table 4.4 shows the main uncertainties coming from cross-section data for the HEU fuel at the beginning of the cycle. This goes to show that the uncertainty related to Deuterium overcomes the one related to the average number of produced neutrons ν because of a more relevant covariance matrix.

Nuclear Data	Sensitivity coefficient	k_{eff} Uncertainty
U-235 ν	0.9997	277 pcm
U-235 fission	0.3009	177 pcm
U-235 capture	-0.1528	96 pcm
H-2 scattering	0.2895	477 pcm
O-16 scattering	0.1142	110 pcm
Total		597 pcm

Table 4.4: Main k_{eff} uncertainties related to nuclear data

4.2 RHF conversion

In the framework of the ILL conversion to a Low Enriched Uranium (LEU) fuel, the loss in fertile material has been compensated by an increase in fuel density (U_3Si_2 compound) and by an increase in meat dimensions inside the plates (length, width and thickness). This latter modification in the design leaves no space for a burnable poison at the extremities of the plates. In the HEU configuration, the boron poison performs a very important role in quenching the power peak at the top and bottom corners of the plates (Figure 4.2). This power peak is due to the self shielding effect of the fuel element with respect to the neutrons that come back to the fuel element only after being moderated in the reflector. The solution adopted in the LEU configuration, places the burnable poison inside the structural tube that surrounds the plates, forming a boron belt around and outside the central channel (Figure 1, right side). In this way, the power peak is kept under control, but is not completely removed, as it was true for the HEU case. The boron belt concept is therefore a crucial parameter in the optimization procedure, having to ensure a safety margin by keeping the power peak below 400 W/cm [47], while meeting neutronics, irradiation and manufacturing

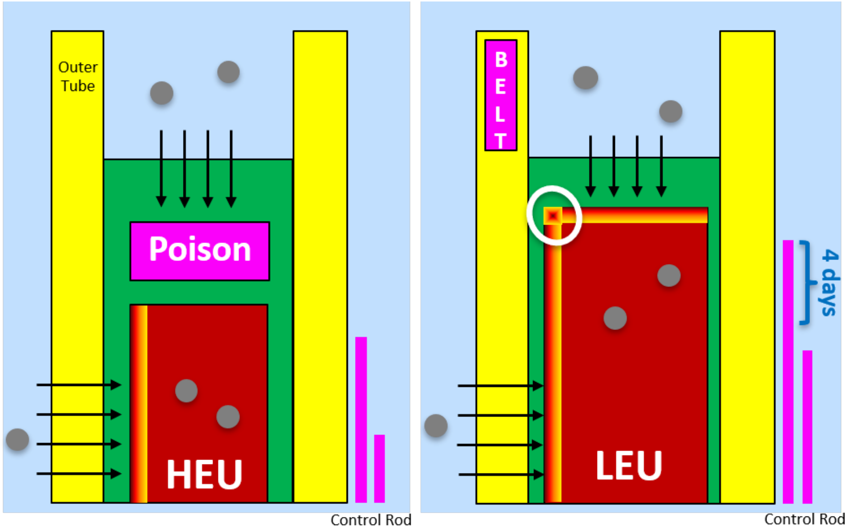

Figure 4.2: HEU and LEU fuel plate configurations (LEU hotspot is circled in white, green=cladding, brown=fuel

criteria.

4.2.1 Boron belt design

As of December 2019, the established features of the boron belt were the following: 1mm thickness, 2cm height, 3.7% B10 atomic fraction, and 0.5cm axial distance from the plates. This was enough to ensure a maximum surface power below 400 W/cm, where the irradiation tests in the European collaborations [49] were conducted at 470 W/cm, leaving enough margin compared to the uncertainties in the model. Since most of the benchmarking in the previous years has been conducted in this configuration, we will refer to it as the “nominal case”. Since December 2019, two major modifications are being taken in serious consideration for the LEU design. The U_3Si_2 fuel density of 5.3 g/cc will be put aside in favour of a 4.8 g/cc density, which despite leading to a higher meat thickness (0.59mm opposed to 0.66mm), allows for a more malleable manufacturing and therefore improved tolerances on the cladding thickness. Furthermore, the mechanical treatment of the fuel

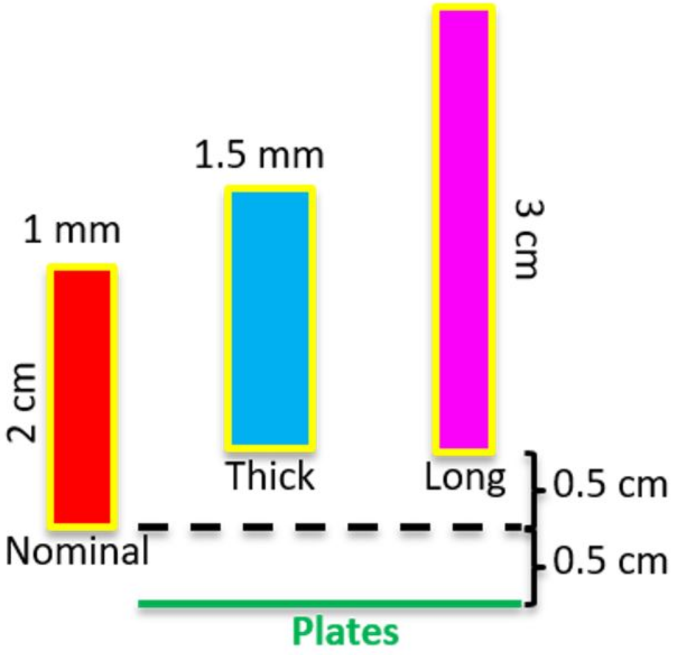

Figure 4.3: Boron belt key configurations

element demands that the boron belt stays at least 1cm away from the plates. For all these reasons, the design of the boron belt needs to be adapted to the new model, while keeping the same performance of the nominal case.

Sensitivity analysis

In order to obtain a sensitivity analysis of the power peak with respect to perturbations in the boron belt, over one hundred Monte Carlo direct calculations where performed with the code SERPENT for a matrix of the following parameters (4.8 g/cc fuel density, short control rod): - Thickness: 0.1, 0.15, 0.2 mm - Length: 2, 3, 4 cm - B10 atomic fraction: 1.8, 2.4, 3.7, 7.5, 10 - Axial distance from the plates: 0.5, 1, 1.5 cm

Out of this bunch of results, two configurations are particularly instructive for a comparison with the nominal one (Figure 4.3). These configurations all carry the same total mass of boron 10, in particular the nominal one has

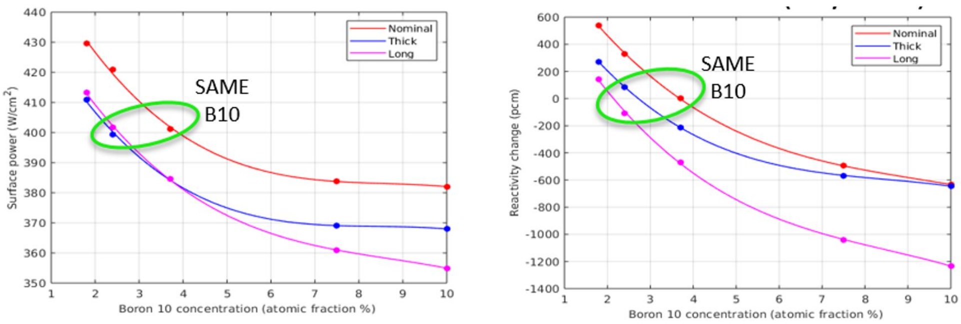

Figure 4.4: Power peak (left) and reactivity (right) for different boron belts configurations

a B-10 atomic fraction of 3.7%, while the thicker and longer one contain a fraction of 2.4%. Furthermore, these latter ones leave a 1cm gap from the plates, allowing for a more suiTable manufacturing margin.

In Figure 4.4, it's possible to see how the proposed configurations can grant the same safety performance while being kept further away from the meat, and hovering around the same reactivity at day zero. The difference between a more or less slender design lies in the self-shielding effect. Since the thicker belt has a lower surface to volume ratio, the bulk material is more shielded and will perform fewer captures at day 0. This effect becomes important for increasing boron 10 concentration.

Length of the cycle

As much as the reactivity at day zero can suggest how a boron belt performs from a neutronic stand, enough non-linearities can arise during the evolution of the cycle to express the need for a full burn up calculation. Following the examples from Figure 4.3 again, it is possible to see another consequence of self-shielding. In Figure 4.5 it is clear that the more slender boron belt promotes captures at the beginning of the fuel element life, burning faster with respect to the thicker one. This can be seen as an asset of the slender design, since the hot spot is stronger at day zero. Furthermore, the boron mass eventually disappears completely from every design after 40

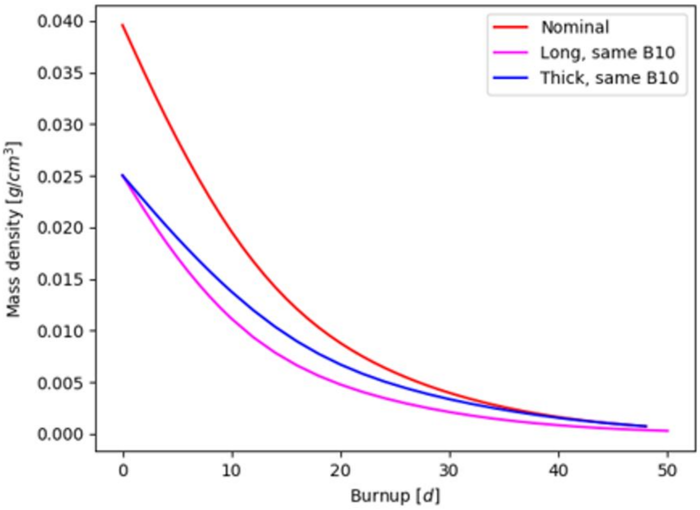

Figure 4.5: Boron concentration evolution with burnup

days, meaning that a long term control of reactivity is performed without excessively affecting the overall neutronics performance of the fuel element.

VESTA evolution

After a preliminary sensitivity study performed with the code SERPENT, the following analysis has been continued with the code VESTA [50], an IRSN software that performs burn up calculations with MCNP. The VESTA model is able to study different configurations with an algorithm that moves the control rod in order to attain criticality at each burn up step. The position of the control rod has a direct influence on the flux distribution and therefore on the hot spot, making this expensive calculation a fundamental step of the design optimization. After some initial refinement in the model, the information gathered can be presented by comparing 4 boron belt configurations on full cycle simulation:

- 3 cm length, 1mm thickness, 1.8% B10 at. fraction, 30000x300 neutron histories (Config. 3_18)

- 4 cm length, 1mm thickness, 1.8% B10 at. fraction, 5000x200 neutron histories (Config. 4_18)

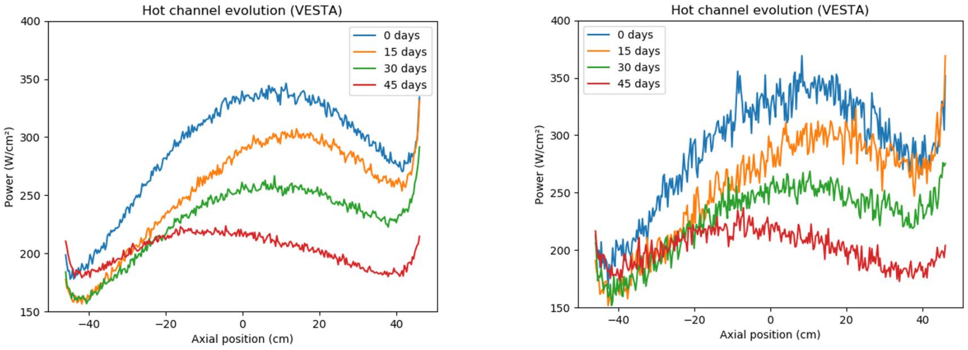

Figure 4.6: TUM (left) and 4_18 (right) hot channel heat flux

- 4 cm length, 1mm thickness, 2.4% B10 at. fraction, 5000x200 neutron histories (Config. 4_24)

- 4 cm length, 2mm thickness, 1.8% B10 at. fraction, 30000x300 neutron histories (Config. TUM)

The last configuration has been considered as a manufacturing starting point, since it has the same dimensions as the one employed in the FRM2 reactor of the Technische Universität München (TUM, [51]). TUM and configuration 3_18 were considered in principle to provide an upper and lower bound for the belt impact on the length of the cycle, while 4_18 and 4_24 would cover the grey area in between, hence the inferior statistical precision demanded to the long calculations. The heat flux acting on the hot channel is presented in Figure 4.6 for TUM and 4_18 configuration

Unfortunately, the *.xml* output files provided by VESTA did not comprise an estimation of the statistical uncertainty associated to the heat flux tally. Yet, the different statistical regimes are quite evident, as it is the maximum heat flux at the top of the element. In this batch of simulations, slender designs were chosen in order to contain the hot spot at the beginning of the cycle. In Figure 4.7, the evolution of the hot spot in the four different configurations is related to the maximum heat flux allowed. It is quite clear how the maximum quickly drops after the 400 W/cm of day zero, causing even the most conservative TUM configuration to overcome the threshold

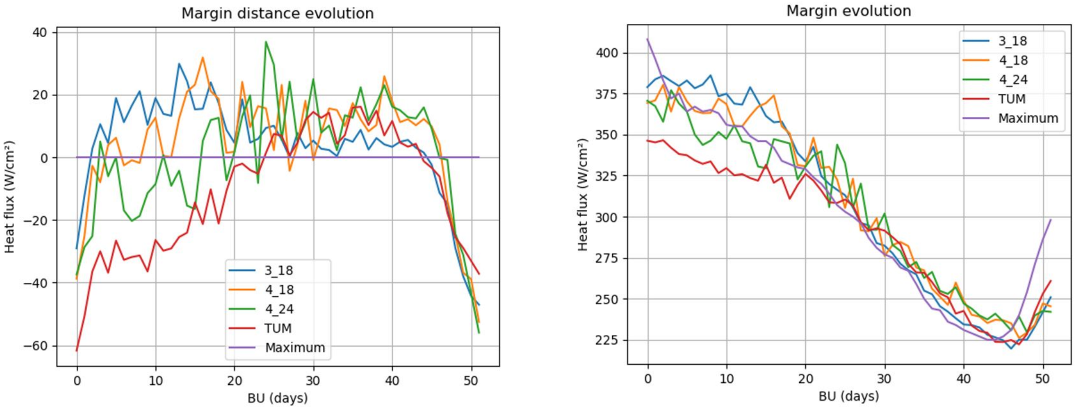

Figure 4.7: Relative (left) and absolute (right) margin to the maximum heat flux experienced during plate irradiation

around day 25.

As shown in Figure 4.8, around day 25-30, the boron at the top of the element disappears in all the considered slender configurations, leading the heat flux to behave rather similarly from that point onwards. On the other hand, the fewer captures on the bottom belt lead to a slower disappearance.

Looking back at Figure 4.7, it is possible to notice how after day 25 roughly, configuration 3_18 seems to lead to a slightly reduced power peak with respect to the other ones. Since the belt has virtually disappeared at this point, the neutron fluxes should be comparable and the reason must necessarily lie in the different levels of burnup reached in the hot spot, which would lead to different fission cross-sections. A comparison between the neutron flux sustained by the hot spot in configuration 3_18 and TUM is shown on the left axis in Figure 4.9, while the fission cross-section behavior is marked with a dotted line referring to the right axis.

From Figure 4.9 we can see how the higher flux experienced initially by the smaller 3_18 belt would lead to a higher burnup around day 20 with respect to the TUM configuration, hence the switch in cross-sections (the 3_18 cross-section is initially higher because of a higher thermal flux component in the energy integral). The maximum in the neutron flux is due to the tradeoff

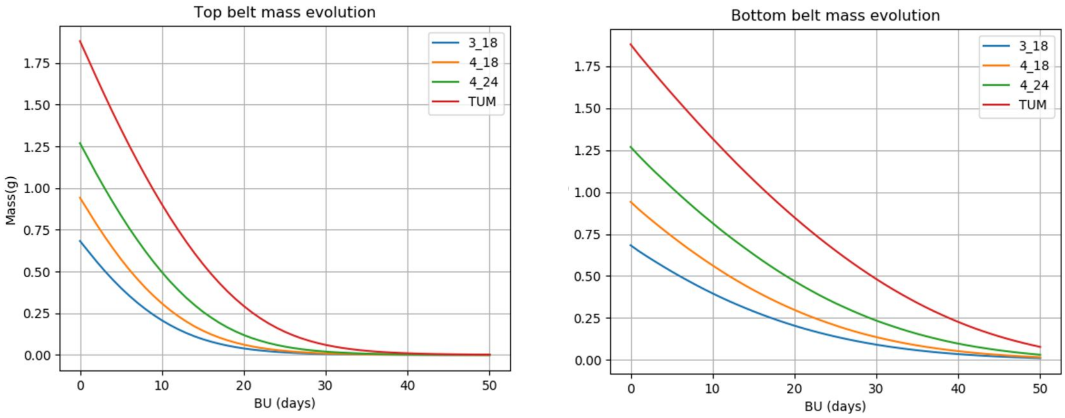

Figure 4.8: Boron concentration evolution in the top (left) and bottom (right) belt

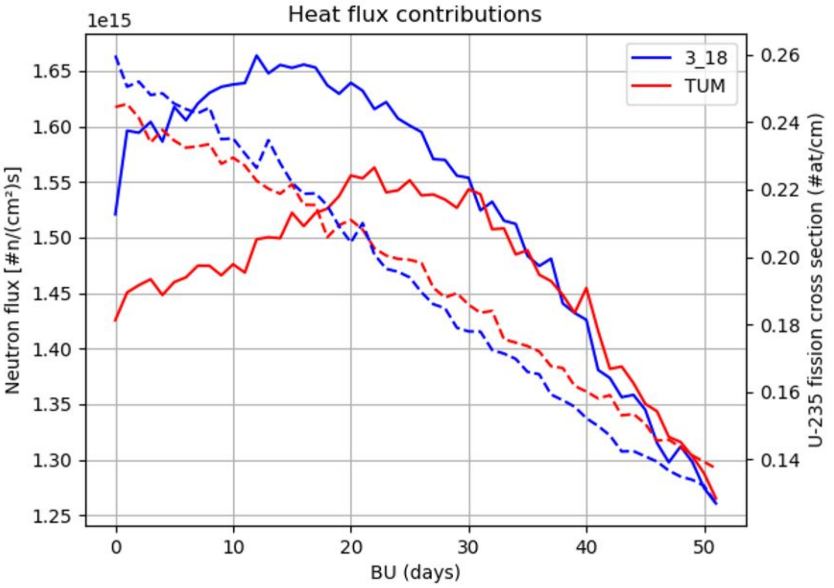

Figure 4.9: Top corner neutron flux (left) and macroscopic cross-section (right)

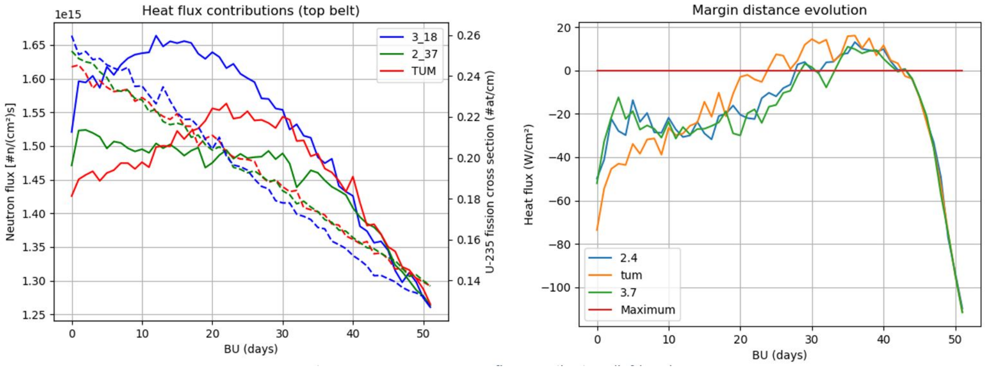

Figure 4.10: Top corner neutron flux (left) and macroscopic cross-section (right)

between the disappearance of boron (increasing flux) and the lowering of the control rod (decreasing flux). In order to study the beneficial effect of a higher flux at BOC, that would sit closer to the maximum in order to promote the burnup, an even more compact configuration has been studied for the top belt:

- 2 cm length, 2mm thickness, 3.7% B10 at. fraction, 30000x300 neutron histories (Config. 2_37)

- 2 cm length, 3mm thickness, 2.4% B10 at. fraction, 30000x300 neutron histories (Config. 2_24)

These 2_37 and 2_24 configurations carry the same boron loading as the TUM one, but the self-shielding already highlighted in Figure 5, allows for a flatter behaviour of the heat flux margin (Figure 4.10, right picture)

Adding configuration 2_37 to the Figure 4.9 plot onto Figure 4.10, it's clear how the flatter heat flux behavior all comes from the flatter neutron flux, while the cross-section roughly follows the TUM configuration. In configuration 2_37 and 2_24, the top boron, completely disappears around day 40, ten days after TUM, as it is evident also from the heat flux and neutron flux plots in Figure 4.10. Concerning the bottom corner, the boron burnup is much slower and the neutron flux has an increasing monotonous behavior (4.11, left picture), since both boron disappearance and lowering of the

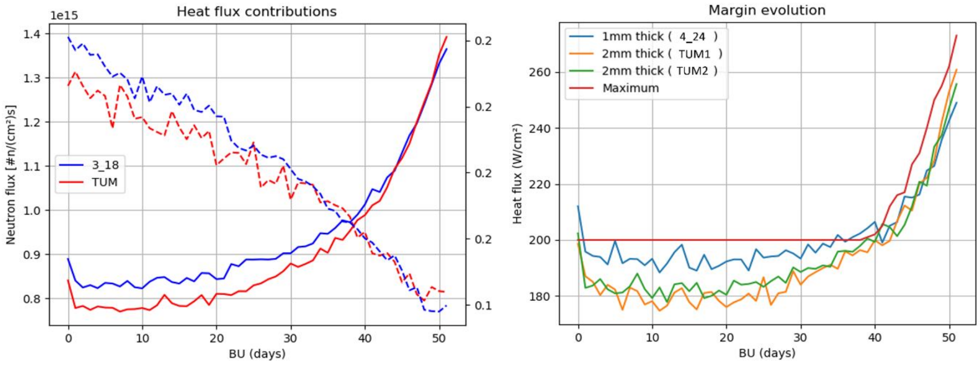

Figure 4.11: Bottom corner heat flux contributions (left) and Heat flux relative margin to the maximum one (right)

control rod play in the same direction.

The TUM configuration allows the heat flux to stay below the maximum one for the whole cycle, regardless of the top belt configuration (TUM1 and TUM2 in Figure 11, right picture). While 4_24 exceeds the maximum at day 0, the lower boron loading leads to a smaller leftover at EOC (Figure 8) and allows for a total length of the cycle of 49 days, against the 48 days obtained with TUM (bearing an uncertainty of 1 day due to the control rod position)

Results recap

The most important configurations, along with their Figures of merit, are summaryzed in Table 1. Only TUM grants some margin to the 200 W/cm maximum heat flux of the bottom corner, while the smaller ones exceed the limit. As shown in the previous sections, the optimal configuration would mean combining the TUM belt at the bottom with a self-shielded one at the top. The uncertainty on the cycle length is about 1 day, and the one on the heat flux margin is usually between 5 and 15 W/cm depending on the simulation. While a lower B-10 charge in the lower belt usually allows for a longer cycle, the gain of the 49th day of cycle is affected by statistical uncertainty and hence not completely trustworthy.

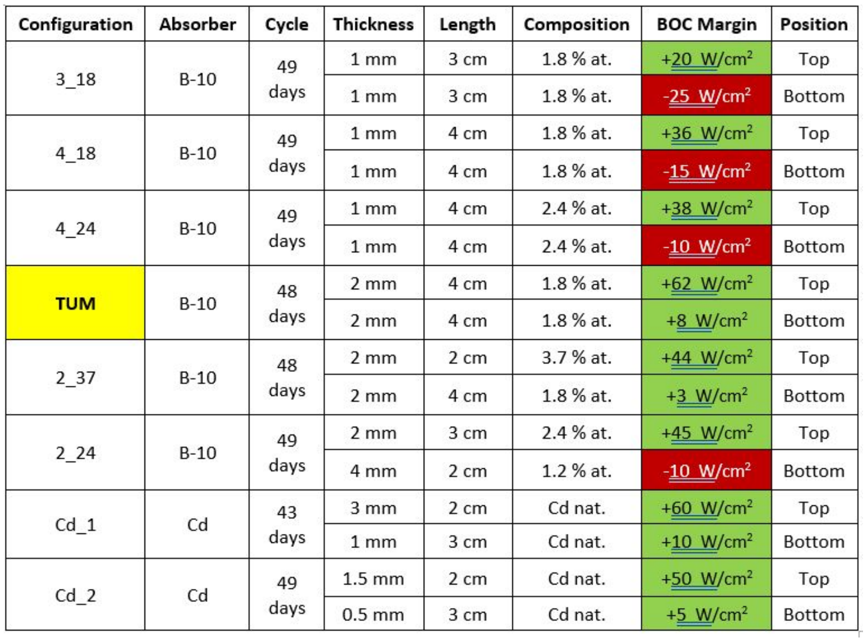

Configuration	Absorber	Cycle	Thickness	Length	Composition	BOC Margin	Position
3_18	B-10	49 days	1 mm	3 cm	1.8 % at.	+20 W/cm^2	Top
			1 mm	3 cm	1.8 % at.	-25 W/cm^2	Bottom
4_18	B-10	49 days	1 mm	4 cm	1.8 % at.	+36 W/cm^2	Top
			1 mm	4 cm	1.8 % at.	-15 W/cm^2	Bottom
4_24	B-10	49 days	1 mm	4 cm	2.4 % at.	+38 W/cm^2	Top
			1 mm	4 cm	2.4 % at.	-10 W/cm^2	Bottom
TUM	B-10	48 days	2 mm	4 cm	1.8 % at.	+62 W/cm^2	Top
			2 mm	4 cm	1.8 % at.	+8 W/cm^2	Bottom
2_37	B-10	48 days	2 mm	2 cm	3.7 % at.	+44 W/cm^2	Top
			2 mm	4 cm	1.8 % at.	+3 W/cm^2	Bottom
2_24	B-10	49 days	2 mm	3 cm	2.4 % at.	+45 W/cm^2	Top
			4 mm	2 cm	1.2 % at.	-10 W/cm^2	Bottom
Cd_1	Cd	43 days	3 mm	2 cm	Cd nat.	+60 W/cm^2	Top
			1 mm	3 cm	Cd nat.	+10 W/cm^2	Bottom
Cd_2	Cd	49 days	1.5 mm	2 cm	Cd nat.	+50 W/cm^2	Top
			0.5 mm	3 cm	Cd nat.	+5 W/cm^2	Bottom

Figure 4.12: Recap Table of the most interesting configurations features

Taking into account all the reported constraints and trade-offs, the final decision favored the adoption of a TUM configuration boron belt both at the top and at the bottom of the plates. This gives the highest priority to the margins at BOC, while keeping a cost-oriented mindset towards the belt manufacturing as well.

4.2.2 Nuclide concentrations sensitivities

The extensiveness of the Boron Belt engineering study, where almost 6 months were spent iterating configurations and performing simulations spanning several weeks, justified the methodological development of Perturbation Theory. It was believed that opening the access to time-dependent sensitivity coefficients would expedite some design optimisation, while also anticipating most results of the uncertainty analysis that is usually performed on the finalized design. The sensitivity coefficients S_α calculated by PTERODAx, obtained as a function of different adjoint quantities, comprise direct and indirect contributions, that provide physical insight on the perturbations themselves. Without retracing the whole theory, it is still possible to split the sensitivities into three terms from Williams [3]:

$$S_\alpha = \sum_i \left(\int_{t_i}^{t_{i+1}} \underbrace{\boldsymbol{N}_i^* \frac{\partial(\boldsymbol{M}_i \boldsymbol{N}_i)}{\partial\alpha}}_{\text{at. evolution}} dt - \underbrace{< \Gamma_i^* | \frac{\partial B_i}{\partial\alpha} \psi_i >}_{\text{flux spectrum}} - \underbrace{< P_i^* | \frac{\partial(\boldsymbol{\sigma}_f \boldsymbol{N}_i)}{\partial\alpha} \phi_i >}_{\text{power level}} \right) \tag{4.1}$$

- Atomic evolution: accounts for direct transmutation into Pu-239
- Flux spectrum: accounts for indirect effects on flux shape and spectrum (e.g. hardening), that impact Pu generation and disappearance
- Power level: accounts for indirect effects on flux normalization, according to the power constraint, that impact Pu generation and disappearance

In order to test the performance of PTERODAx, multiple SIBYL direct calculations, in which some parameter α is perturbed, are used to obtain EOL plutonium densities, which are then compared with the sensitivities coming from a single nominal PTERODAx run. Figure 4.13 shows the accuracy of these coefficients and breaks them down into the three contributions. The red bar refers to the direct results obtained from different perturbed SIBYL calculations, while the blue bar refers to the PTERODAx estimation of the Pu mass change coming from sensitivity coefficients. A small label displaying the relative error between SIBYL and PTERODAx can be seen next to these columns. The remaining three colored bars represent the different contributors in Eq. 4.1. This histogram will be the most common mean of representation of PTERODAx results in this Chapter.

A 1% perturbation in fresh fuel density of U-235 or U-238 has different ways of affecting the Pu-239 density in EOL spent fuel. The red bar refers to the direct results obtained from different perturbed SIBYL calculations, while the blue bar refers to the PTERODAx estimation (sensitivity multiplied by relative density perturbation). The remaining three colored bars represent the different contributors in Eq. 4.1. U-238 has a preponderant evolution contribution (in green), since it can directly transmute into Pu-239

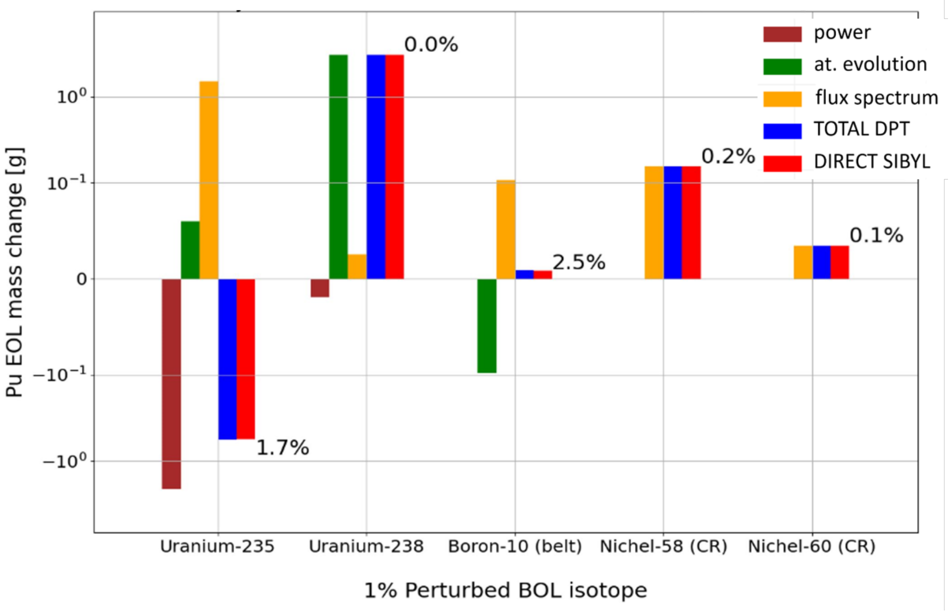

Figure 4.13: PTERODAx results for EOL Pu-239 mass sensitivity to different BOL perturbations, compared with SIBYL direct calculations (the relative error is reported on top of the histograms)

by absorbing a neutron. U-235, on the other hand, can not transmute directly into Pu-239 and will only contribute indirectly to Pu generation. For example, a 1% increase in U-235 mass will increase k, decreasing the total flux for the same fixed total power, which causes U-238 to absorb fewer neutrons due to the lower flux. This is why the brown bar brings a negative contribution to the Pu sensitivity to U-235. On the other hand, a 1% increase in U-235 mass will also increase thermal absorptions. Leading to a slight shift of the flux spectrum towards the epithermal region, where U-238 capture cross-section is higher and less in competition with U-235 absorptions. Since the main perturbed isotopes are all thermal absorbers, they have similar indirect contributions to the flux shape and spectrum (positive orange bars).

Furthermore, the reason why some isotopes have a relevant "atomic evolution contribution", while it is impossible for them to directly transmute into Pu, lies in the DPT algorithm. The adjoint atomic evolution N^* is in fact updated at each Bateman time step by PTERODAx, in order to take into account indirect contributions. This fictitious contribution to the atomic evolution ultimately accounts for the depletion of the perturbed isotope during burnup. While this is detecTable for U-235, it is predominant for B-10, which has a burnup of 100% and an almost perfect compensation of the two contributions. This is because, as it was mentioned in section 2, the burnable poison density was optimized in order to maximize the shielding of the hot spot at the beginning of life, while minimizing the impact on the fuel element reactivity worth and the reactor cycle length. This compensation phenomena are most common of many sensitivity contributions, and it is impossible to see employing only direct calculations.

On a final note, the evolution of Pu-239 sensitivity coefficients with time is shown in Figure 4.14 for a U-235 perturbation. The final condition sets N^*=0 and with it the total sensitivity. Then the adjoint Bateman equation is solved backwards in time and the indirect contributions stack up the different terms, including the atomic evolution one. The values at day 0 are the ones shown in Figure 4.13, connecting a BOL perturbation to an EOL output such as Pu density. The peculiarity of this plot lies in the sign swap of the power constraint contribution: as explained before, an increase in U-235 decreases the flux and U-238 absorptions with it. While this is true at day 0 and through most of the cycle, by approaching the EOL, the decay constant of Np-239 (2.3 days) prevents the U-239 decay chain from getting to Pu-239 in time for day 50, which is EOL. This ultimately means that, after day 43, a decrease in flux is not preventing Pu-239 production (negative sensitivity), but rather preventing absorptions from the Pu-239 already generated (positive sensitivity). The red "pert" line refers to the perturbed SIBYL calculation.

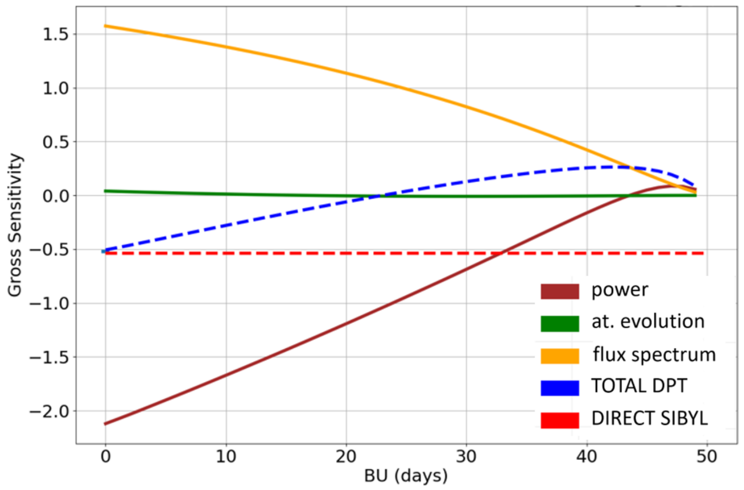

Figure 4.14: PTERODAx sensitivity evolution at different burnup points for an EOL Pu-239 density response to a perturbation in BOL U-235 density.

4.2.3 Multiplication factor sensitivities

PTERODAx is also capable of estimating k sensitivities. The k sensitivity results are shown in Figure 4.15: the bilinear definition of the multiplication factor brings an additional "adjoint flux spectrum" contribution (yellow bar) to the total sensitivity, as discussed in Section 2.2.4.

The sensitivity S_k of each nuclide at end of cycle (purple bar) is often the main contributor to the sensitivity. This is because, for a multiplication factor response, the final condition on the adjoint nuclide field is $N^* = S_k$. While B-10 perturbations had a small impact on EOL Pu-239 mass, the impact on EOL k is zero. This is because, even though boron is completely burned at EOL, the lag in Pu production caused by Np-239 decay causes the "backlog" effect of a few days mentioned in the previous section, which is not true for k.

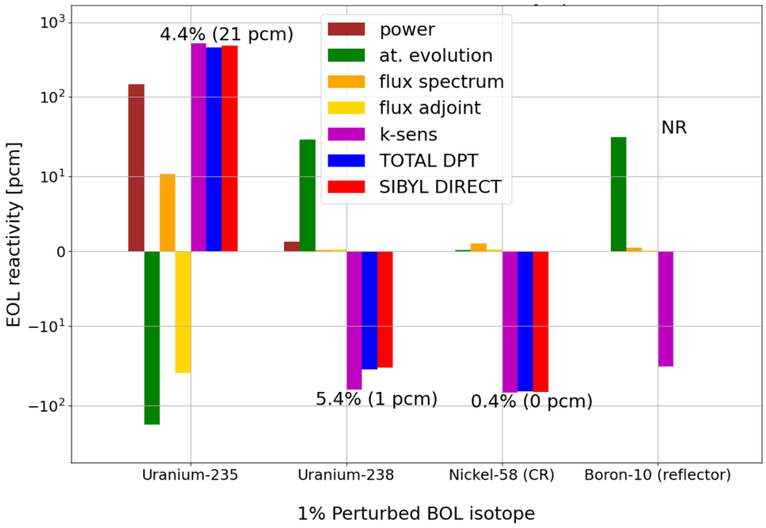

Figure 4.15: PTERODAx results for EOL k sensitivity to different BOL perturbations, compared with SIBYL direct calculations

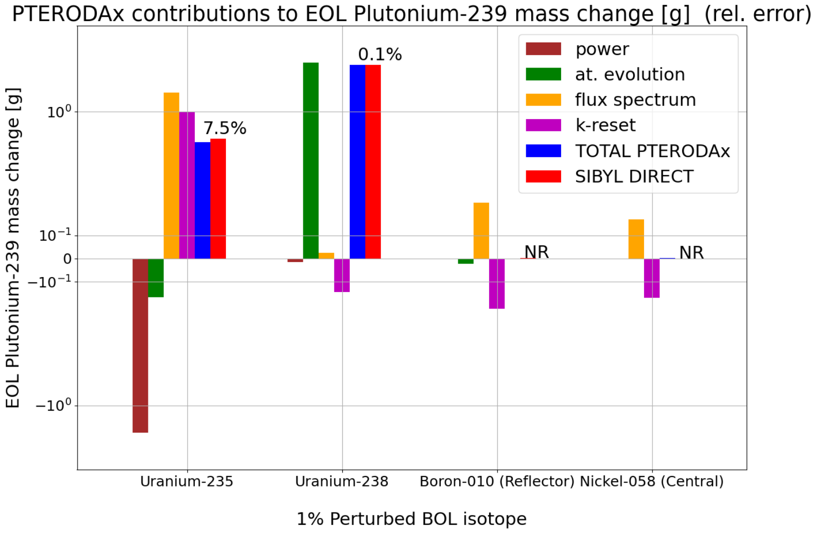

Figure 4.16: PTERODAx results for EOL Pu-239 sensitivity to different BOL perturbations, compared with SIBYL direct calculations performed with criticality reset

4.2.4 Criticality reset

The same analysis performed on these nuclide density sensitivities can be repeated while also imposing a criticality reset to SIBYL. The way the reset is handled by SIBYL is shown in section 3, while the adaptation to the DPT algorithm adjustments is outlined in section 2. The additional k-reset contribution in PTERODAx comes from the reactivity weighed contribution of the control nuclides with respect to the perturbed one. The most relevant result highlighted in Figure 4.16 is the sign swap on the Pu-239 sensitivity for U-235 with respect to Figure 4.13. This is a consequence of the important Nickel increase imposed by a 1% positive perturbation in U-235, which has a positive sensitivity on Pu-239 (as shown in Figure 4.13). The increase in U-235 gets completely "translated" in a Nickel sensitivity of equal reactivity weight.

4.3 UAM benchmark

Similar studies to the ones performed on the RHF have successively been carried out on the UAM benchmark. In particular, a detailed propagation of nuclear data uncertainties, fully employing DPT, has been successfully compared to Total Monte Carlo methods developed by the other benchmark participants.

4.3.1 Nuclide concentrations sensitivities

In order to verify the performance of PTERODAx on this second test case, multiple SIBYL direct calculations, in which some parameter α is perturbed, are used to obtain EOL plutonium densities, which are then compared with the sensitivities coming from a single nominal PTERODAx run.

Figure 4.17 shows the accuracy of these coefficients and breaks them down into the three contributions. The red bar refers to the direct results obtained from different perturbed SIBYL calculations, while the blue bar refers to the

PTERODAx estimation of the Pu mass change coming from sensitivity coefficients. The remaining three colored bars represent the different contributors in Eq. 4.1. A +1% perturbation in fresh fuel number densities of U-235 or U-238 has different ways of affecting the Pu-239 density in EOL spent fuel. U-238 main contribution is due to its direct evolution into Pu-239, while U-235 pertburbations carry two indirect competing effects.

The first one is the normalization of the fission source according to the power constraint, leading to a more effective neutron economy and fewer absorptions on U-238 (hence the negative brown bar). The second effect is a hardening of the flux caused by the increase in thermal U-235 absorptions, which leads to more epithermal neutrons available for U-238 resonances (hence the positive yellow bar). Lastly, the negative green bar in U-235 perturbations is related to its 50% depletion at EOL, which reduces the total value of its sensitivity.

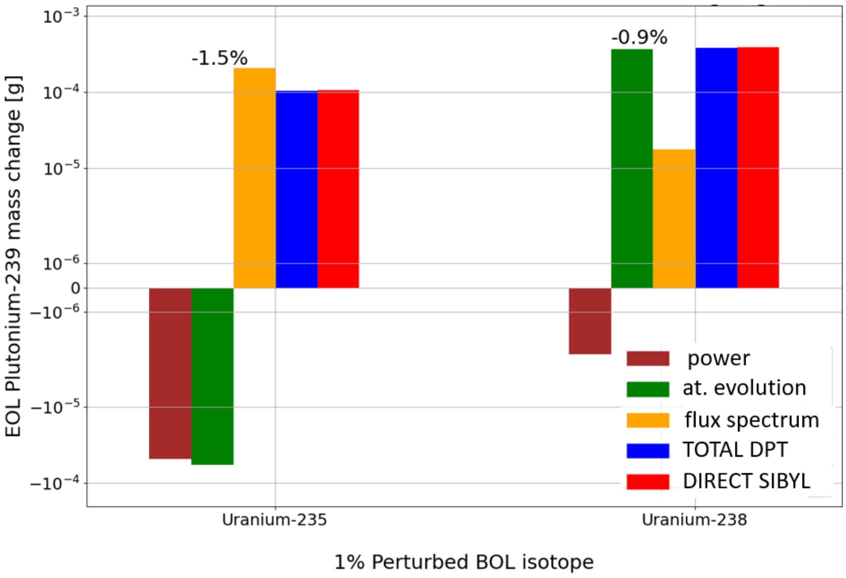

Figure 4.17: PTERODAx results for EOL Pu-239 mass sensitivity to different BOL perturbations, compared with SIBYL direct calculations (the relative error is reported on top of the histograms)

4.3.2 Multiplication factor sensitivities

Some examples of sensitivity vectors estimated by PTERODAx are displayed in Figure 4.18, and compared with SIBYL.

In order to compare SIBYL results with PTERODAx in Figure 4.18, 44 calculations have been performed, carrying a 1% perturbation for each individual energy group. Then, the associated final residual reactivity has been recorded and compared with the PTERODAx sensitivity estimation. While only one adjoint calculation replaces all the 44 perturbed ones (and more, if for example different reaction perturbations are envisaged for the same nuclide), one single adjoint calculation presently requires around 5 to 10 times the calculation time of a direct forward one, encouraging further optimization in the algorithm. The sensitivity results obtained by PTERODAx have been employed in combination with SCALE 5.1 covariance matrices via the "sandwich rule" [36]. Elastic and inelastic perturbations are not taken in consideration due to the scattering matrix that was implemented in the SIBYL model. This implementation does not include a separation of the scattering matrix terms between different nuclides. Furthermore, only perturbations coming from 3 nuclides have been considered at this stage: U-235, U-238 and Pu-239. And only 3 perturbations in nuclear data: fission cross-section, capture cross-section, and average number of emitted neutrons.

4.3.3 Evolution of uncertainties

The results in Table 4.5 refer to different end of life k uncertainties associated to a perturbation in the 44 groups cross-sections of the listed reactions. As already outlined by most benchmark participants, the average relative standard deviation (RSD) for plutonium covariance matrices makes it the main contributor to the uncertainty at high burn up. The resonance capture cross-section for U-238 is also a well established contributor to the total uncertainty. All the uncertainties in Table 4.5 can be obtained from one standard calculation (nominal + adjoint) over 100 time steps, presently requiring

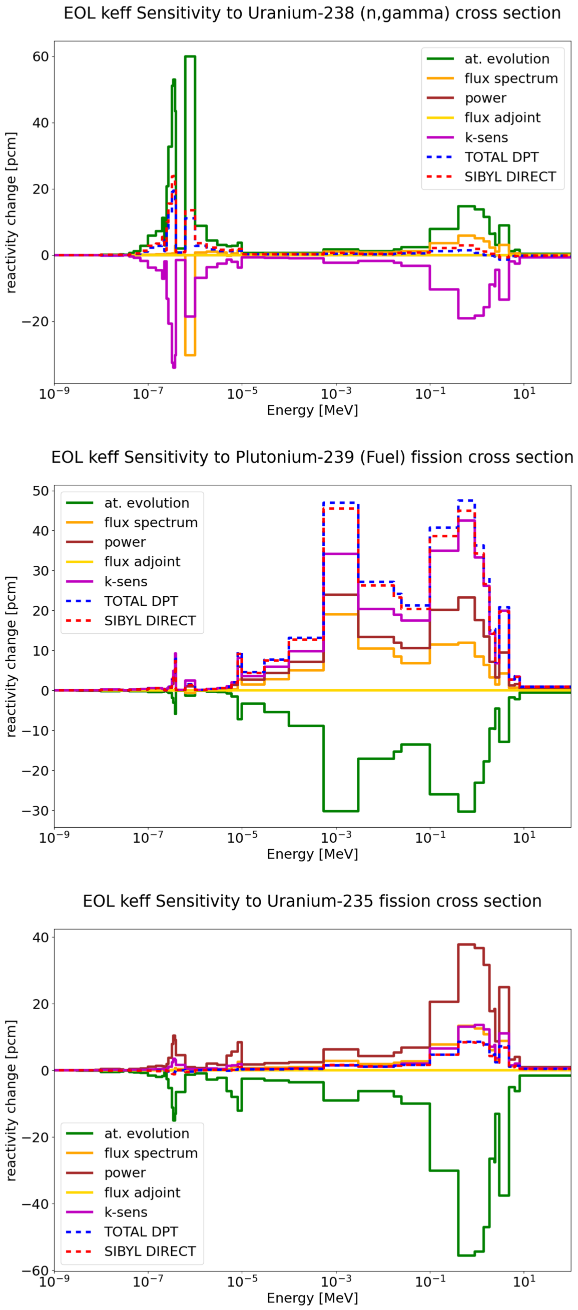

Figure 4.18: End of life k sensitivities to different cross-section perturbations.

Table 4.5: EOL k uncertainty contributors (results in pcm)

Nuclide	**Nuclear Data**	**Uncertainty**
Pu-239	nubar	512
U-238	capture	480
Pu-239	fission	260
Pu-239	capture	203
U-238	nubar	55
U-235	fission	30
U-235	capture	29
U-235	nubar	21
U-238	fission	3
Total		**779**

around 90 minutes on a Linux machine with 8 GB of RAM.

In order to facilitate the comparison with the UAM benchmark results for exercise I-1b, the uncertainty evolution all along the burn up has been reproduced in Figure 4.20. It has to be noted that, while the different uncertainty points are easily retrievable at different steps of the sampling chain, the DPT algorithm works differently. An example of the k time dependent sensitivity to a perturbation in Pu-239 concentration is shown in Figure 4.19. The final sensitivity corresponds to the k sensitivity, and then converges to the SIBYL DIRECT perturbation at the beginning of life. In a standard forward problem, the sensitivities obtained at any time t of the cycle represent the effect of a BOL perturbation on an output parameter at time t. On the other hand, The DPT sensitivity results, retrieved at a certain time t of Figure 4.19, actually represent the effect of a perturbation at time t (injection of a burnable poison for example) on the EOL parameter. This follows from the final condition imposed on the adjoint nuclide field and the backward solver for the adjoint Bateman equation, meaning that a single nominal DPT simulation has to be allocated to each burn up point of Figure

4.20. The uncertainty results propagated by PTERODAx are consistent at high burn-up with other participants employing SCALE5 data. At beginning of life, on the other hand, the uncertainty results are underestimated. This is most probably because of the missing contributions by some lighter nuclides, such as hydrogen, oxygen, poisons, and scattering reactions. These minor contributions, similarly to the ones coming from U-235, become even less relevant as plutonium keeps building up.

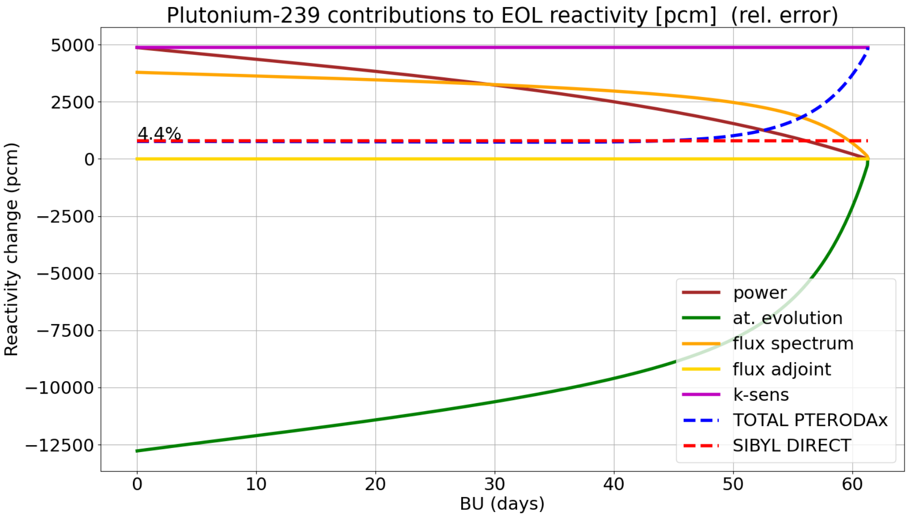

Figure 4.19: Time dependent sensitivity to a perturbation in Pu-239

4.3.4 Time discretization

A particularly interesting feature of the implementation of DPT into PTERODAx, has proven to be the time discretization choice for both the forward and the adjoint Bateman equation. As it is well established that the build-up of xenon and other poisons calls for smaller time steps in the very first days of the depletion calculation, the same thing is demanded by the adjoint equation. The steep derivative of the nuclides adjoint field in proximity of the final condition calls for a higher discretization at EOL as well, as

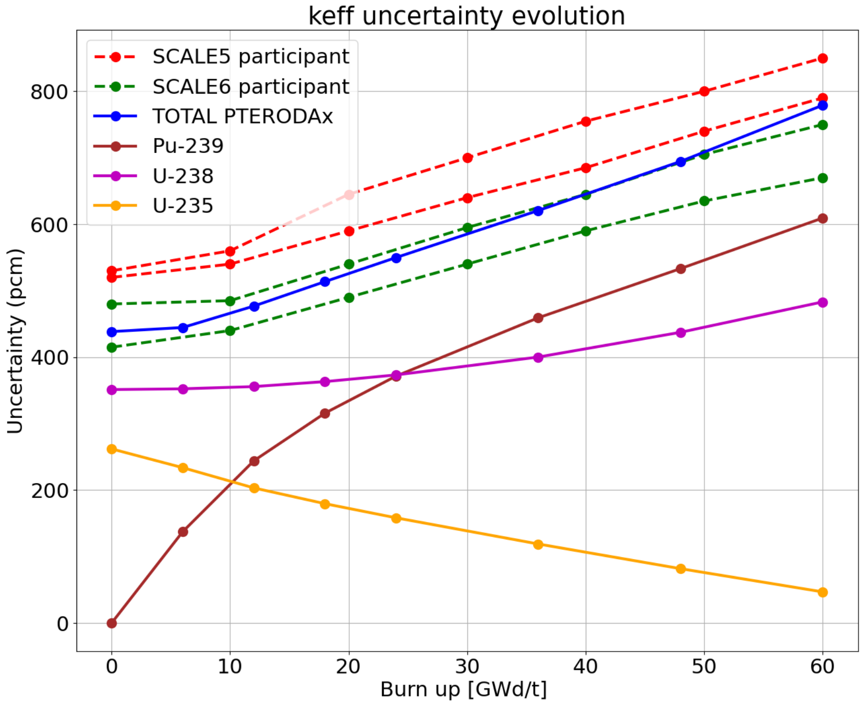

Figure 4.20: k uncertainty evolution with BU, compared to other contributors in the UAM benchmark

it visible in Figure 4.19. In particular, if the discretization were to be carried out only at BOL (heterogeneous 1 in Figure 4.21 and 4.22), it would show an even worse DPT convergence with respect to the fully homogeneous time grid. A tailored discretization at both ends of the calculation (heterogeneous 2 in Figure 4.21 and 4.22) is crucial to obtain satisfying results within step lengths employed in common practice. While U-238 k sensitivities have the slowest convergence, due to the atomic evolution effect raised by the Pu-239 production, all sensitivities show errors below 10% when employing 25 days of average step length.

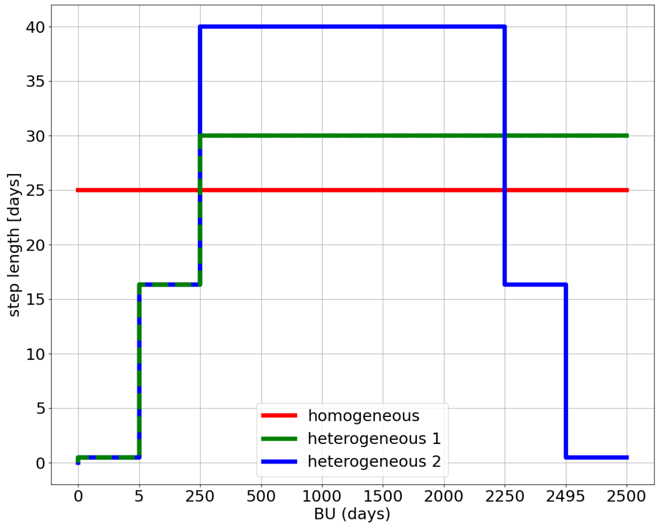

Figure 4.21: Different time discretizations, accounting for 100 total steps

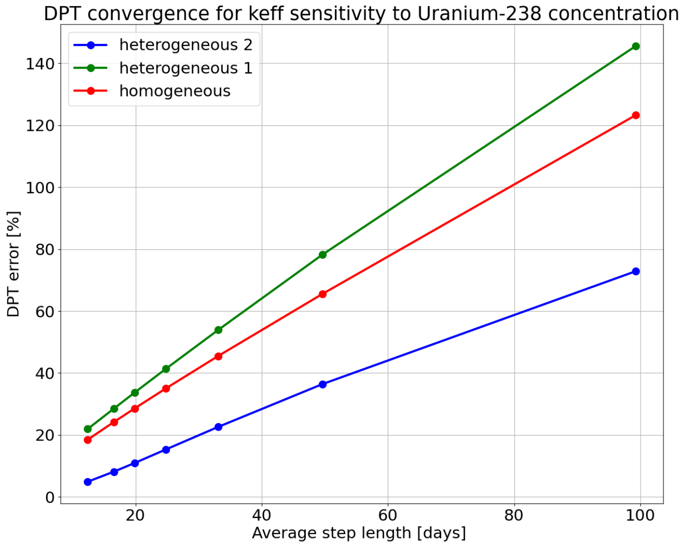

Figure 4.22: Error convergence for different time discretizations

Chapter 5

Conclusions

In this work, a wide set of cutting-edge sensitivity tools has been put to test in different contexts. Static and time-dependent sensitivities have been employed both in the design phase and in the licensing phase of an ongoing core configuration study such as the LEU fuel for the RHF. For validation purposes, a similar study has also been performed on the UAM fuel pin benchmark of an LWR, propagating nuclear data uncertainties all along the fuel burnup.

First, the capability of Generalized Perturbation Theory to assess experimental uncertainties in the Monte Carlo code SERPENT has been tested. Sensitivity coefficients confirmed to be an important tool that allows to calculate k_{eff} uncertainties with good accuracy and within the same criticality calculation. Of course, tolerances on compositions and densities are much easier to be assessed with this methodology, but it was successfully shown that uncertainties on geometry specification, like the thickness of the coolant channel, can be estimated as well with a careful homogeneous approximation. For the RHF, the large amount of scattering in D_2O dominates both experimental and nuclear data uncertainties, with the statistics being affected as well.

This approach allowed to perform relevant comparisons of different scenarios uncertainties, showing how sTable the RHF uncertainties are with respect to the flooding of the most relevant beam tube and with respect to the conversion to a new LEU fuel. In this latter case, the only minor novelty was detected in the uncertainty related to the burnable poison, since the manufacturing of a single boron belt component foregoes the normalization for fuel plates independence.

The boundaries of the project have subsequently been extended to time-dependent sensitivities, with a focus on depletion perturbation theory. The unavailability of these coefficients in SERPENT, called for the development of an ad hoc modeling tool. A three-regions model was developed in Python to capture the evolution of the main parameters of the HEU and LEU core configurations of the RHF and their sensitivities. SIBYL has proved to be an accurate surrogate model for solving the coupled Boltzmann-Bateman equations in this three regions scenario. The possibility to perform multiple fast evolution calculations proved to be a key step in the refinement of the DPT algorithm. While SIBYL was initially conceived for describing the High Flux Reactor behaviour, its replication on the LWR-UAM international benchmark could be essential in providing the international community with a set of results that could be easily reproduced.

Depletion perturbation theory, as implemented in PTERODAx coupled with SIBYL, proved to be very accurate in estimating nuclide density and multiplication factor sensitivities. This feature is most definitely enriched by the physical insight these coefficients can provide on the physical contributors to the desired output, broadening the application of sensitivity analysis from uncertainty propagation to design optimization and refinement. The strength of the boron belt optimization analysis, has in fact been enriched by DPT sensitivities, demonstrating how its impact on the length of the cycle has been reduced to zero, while preserving its main safety features. The PTERODAx results have also proven to be consistent with reactivity uncertainties propagated with covariance matrices by the UAM-benchmark participants to exercise I-1b.

The variational approach followed in Chapter 2 for Depletion Perturbation Theory, has been used to unify different approaches presented by [52], [4] and [31], where adjoint-weighed responses, and in particular criticality reset solutions, were treated in different fashions. The importance of criticality reset has been highlighted as a crucial discriminant in obtaining true physical results for reactor operation, justifying the need for a 3 regions approximation in the RHF model to purposefully reproduce the control rod behavior.

Concerning the UAM benchmark, on the other hand, a zero-dimensional approximation would probably have been sufficient to reproduce its main parameters. Suggesting that whenever a nuclear data uncertainty propagation might be needed for complicated geometries, concerning advanced reactors for example, a zero-dimensional model of a fast breeder reactor fuel pin, or a pebble bed high-temperature design, could probably be employed with DPT in order to yield satisfactory first approximation results of how nuclear data affects their parameters, without the immediate need for a high fidelity Total Monte Carlo approach.

Further spatial discretization of SIBYL is restrained by surface detectors in SERPENT. But the implementation of DPT to higher fidelity transport codes is definitely encouraged. The accuracy of integral sensitivity coefficients in reproducing direct perturbations results has been shown for the essential approximation of 2 energy groups and a few tens of nuclides, which could be interesting for the usual two-step diffusion codes employed in industrial applications. Allowing for an increase in number of regions, while still possibly obtaining satisfactory computational times and memory usage, the access to relevant information such as power distribution sensitivities could be envisaged. On the other hand, whenever the amount of energy groups and fuel nuclides is increased, the spatial discretization would probably need to be cut back.

In future developments, the agile and versatile nature of this architecture should be exploited to perform comparisons between different datasets, such as SCALE5 and SCALE6, and higher energy groups matrices. Now that the accuracy of the method has been established, the algorithm speed must also be improved and characterized by its main featured parameters: number of steps, perturbations, and energy groups. This is important in order to justify its concurring performance with direct sampling methods, at least for preliminary sensitivity analysis.

In order to facilitate the accessibility of this very investigative tool, a next step of this development could be the direct coupling with SERPENT. This could be made possible by exploiting SERPENT's established GPT routine to estimate the indirect spectrum contributions in the DPT algorithm, which might be handled either within SERPENT itself (much like it has been proved possible in SCALE [13]), or by developing a tailored open access python package.

Appendix A

Point kinetics parameters

The point knetics equation is the primary tool that is used to study the time reponse of Nuclear Reactors. Although it is obtained starting from strong assumptions, it is very handy for primary assessments of different transients of multiplication systems. For these reasons, the parameters that appear in this equation have a very strong physical meaning when describing a reactor.

Starting from the non stationary Boltzmann equation for $\Phi(\boldsymbol{r}, \boldsymbol{\Omega}, E, t)$, accounting for sources, delayed neutrons and their precursors concentration $C_j(\boldsymbol{r}, t)$:

$$\frac{1}{v}\frac{\partial \Phi}{\partial t} = (\hat{L_\Omega}+\hat{L_a}+\hat{L_s})\Phi+[1-\beta(E)]\frac{\chi(E)}{4\pi}\int \sigma_f(\boldsymbol{r}, E')\nu(E')\Phi(\boldsymbol{r}, \boldsymbol{\Omega'}, E', t)\boldsymbol{d\Omega'}dE' + \sum_j \lambda_j C_j \frac{\chi_j(E)}{4\pi} + Q$$

$$\frac{\partial C_j}{\partial t} = -\lambda_j C_j + \beta_j(E)\int \sigma_f(\boldsymbol{r}, E')\nu(E')\Phi(\boldsymbol{r}, \boldsymbol{\Omega'}, E', t)\boldsymbol{d\Omega'}dE' \tag{A.1}$$

Where $\beta = \sum \beta_j$, is the total delayed neutron fraction, while j is the index of each precursor group, based on their decay constant λ_j. The hypotheses of delayed neutron fraction and emission spectrum independence on the incoming energy of neutrons was also made.

A precursor production operator is now defined and the emission spectrum function is lumped in the precursor concentration:

$$\hat{L_\beta} = \sum_j \beta_j \frac{\chi_j(E)}{4\pi} \int \sigma_f(\boldsymbol{r}, E')\nu(E')\boldsymbol{d\Omega}' dE' \tag{A.2}$$

$$\tau_j(\boldsymbol{r}, E, t) = C_j(\boldsymbol{r}, t)\chi_j(E)\frac{1}{4\pi} \tag{A.3}$$

Since $(1-\beta)\chi = \chi - \sum \beta_j \chi_j$, it is possible to write:

$$\frac{1}{v}\frac{\partial \Phi}{\partial t} = (\hat{L} - \hat{L_\beta})\Phi + \sum_j \lambda_j \tau_j + Q \tag{A.4}$$

$$\frac{\partial \tau_j}{\partial t} = -\lambda_j \tau_j + \hat{L_{\beta_j}}\Phi \tag{A.5}$$

The follwing identities from critical reactor (0 subscript) configuration are introduced:

$$\hat{\Delta L} = \hat{L} - \hat{L_0} \tag{A.6}$$

$$< \Phi|\hat{L_0^\dagger}\Phi_0^\dagger > = < \hat{L_0}\Phi|\Phi_0^\dagger > = 0 \tag{A.7}$$

$$< \hat{L}\Phi|\Phi_0^\dagger > = < \hat{\Delta L}\Phi|\Phi_0^\dagger > \tag{A.8}$$

Which show the only the non-critical component of the Boltzmann operator keeps the equation non-stationary. Now the power $P(t)$ is defined as the separated and scaled time behavior of the neutron flux:

$$\Phi(\boldsymbol{r}, \boldsymbol{\Omega}, E, t) = \Psi(\boldsymbol{r}, \boldsymbol{\Omega}, E)P(t) \tag{A.9}$$

Multiplying the Boltzmann equation by $\Phi_0^\dagger$, the identities A.8 can be exploited:

$$\frac{d}{dt} < \frac{1}{v}\Psi|\Phi_0^\dagger > = [< \hat{\Delta L}\Psi|\Phi_0^\dagger > - < \hat{L_{\beta_j}}\Psi|\Phi_0^\dagger >]P(t) - \sum_j \lambda_j < \tau_j|\Phi_0^\dagger > + < Q|\Phi_0^\dagger > \tag{A.10}$$

$$\frac{d}{dt} < \tau_j|\Phi_0^\dagger > = < \hat{L_{\beta_j}}\Phi|\Phi_0^\dagger > - \lambda_j < \tau_j|\Phi_0^\dagger > \tag{A.11}$$

Which can finally be written as the point kinetics equations:

$$\frac{dP(t)}{dt} = \frac{\rho - \beta}{\lambda} P(t) + \sum_j \lambda_j R_j(t) + q \tag{A.12}$$

$$\frac{dR_j(t)}{dt} = \frac{\beta_j}{\lambda} P(t) - \lambda_j R_j(t) \tag{A.13}$$

Where each parameter is defined as a bi-linear ratio. The reactivity ρ is the fundamental parameter of this equation and determines the multiplication ($\rho > 0$) or extinction ($\rho < 0$) of the neutron population.

$$\rho = \frac{< \hat{\Delta L} \Psi | \Phi_0^\dagger >}{< \hat{F} \Psi | \Phi_0^\dagger >} \tag{A.14}$$

The $\beta_{eff} = \sum_j \beta_{eff,j}$ is the fraction of neutrons that comes from the decay of the precursors. Being weighed on the flux it accounts for the lower emission spectrum of the precursors with respect to the fissile, making this parameter slightly higher than the nominal β.

$$\beta_{eff,j} = \frac{< \hat{L_{\beta_j}} \Psi | \Phi_0^\dagger >}{< \hat{F} \Psi | \Phi_0^\dagger >} \tag{A.15}$$

The neutron lifetime λ_{eff} defines the time constants of the reactor response, ranging from milliseconds for graphite reactors to microseconds for fast reactors:

$$\lambda_{eff} = \frac{< \frac{1}{v} \Psi | \Phi_0^\dagger >}{< \hat{F} \Psi | \Phi_0^\dagger >} \tag{A.16}$$

Finally, R_j and q are related to the j_{th} precursor group concentration and to the the source term.

$$R_j(t) = \frac{< \tau_j | \Phi_0^\dagger >}{< \frac{1}{v} \Psi | \Phi_0^\dagger >} \tag{A.17}$$

$$q = \frac{< Q | \Phi_0^\dagger >}{< \frac{1}{v} \Psi | \Phi_0^\dagger >} \tag{A.18}$$

Appendix B

GPT in SERPENT

The results obtained in chapter 2 can be further extended to reaction rate ratios and kinetic parameters, while generalizing the formula with covariance ratios.

Reaction rate ratios

A reaction rate is a linear functional of the forward flux, and can be regarded as the number of scores per second of a detector with a certain cross section Σ. The knowledge of the ratio between two reaction rates Σ_1 and Σ_2 can therefore provide relevant neutronics information in a specific location. The following response function is defined:

$$R = \frac{< \Sigma_1 | \Phi >}{< \Sigma_2 | \Phi >} \tag{B.1}$$

Introducing a perturbation in these cross sections, the altered response function will be:

$$R' = \frac{< \Sigma_1 + \Delta\Sigma_1 | \Phi + \Delta\Phi >}{< \Sigma_2 + \Delta\Sigma_2 | \Phi + \Delta\Phi >} = \frac{< \Sigma_1 | \Phi > + < \Sigma_1 | \Delta\Phi > + < \Delta\Sigma_1 | \Phi >}{< \Sigma_2 | \Phi > + < \Sigma_2 | \Delta\Phi > + < \Delta\Sigma_2 | \Phi >} \tag{B.2}$$

Where the second order term has been neglected. In order to retrieve the sensitivity as it was done for k_{eff}, the normalized variation is written:

$$\frac{R'-R}{R}=\frac{dR}{R}=\left[\frac{(<\Sigma_1|\Phi>+<\Sigma_1|\Delta\Phi>+<\Delta\Sigma_1|\Phi>)<\Sigma_2|\Phi>}{(<\Sigma_2|\Phi>+<\Sigma_2|\Delta\Phi>+<\Delta\Sigma_2|\Phi>)<\Sigma_2|\Phi>}+\right.$$
$$\left.-\frac{(<\Sigma_2|\Phi>+<\Sigma_2|\Delta\Phi>+<\Delta\Sigma_2|\Phi>)<\Sigma_1|\Phi>}{(<\Sigma_2|\Phi>+<\Sigma_2|\Delta\Phi>+<\Delta\Sigma_2|\Phi>)<\Sigma_2|\Phi>}\right]\cdot\frac{<\Sigma_2|\Phi>}{<\Sigma_1|\Phi>}$$

From this, the unperturbed terms disappear from the numerator, as expected, while they dominate the denominator, meaning that the higher order terms can be neglected:

$$\frac{dR}{R}=\frac{(<\Sigma_1|\Delta\Phi>+<\Delta\Sigma_1|\Phi>)<\Sigma_2|\Phi>}{<\Sigma_2|\Phi><\Sigma_1|\Phi>}+$$
$$-\frac{(<\Sigma_2|\Delta\Phi>+<\Delta\Sigma_2|\Phi>)<\Sigma_1|\Phi>}{<\Sigma_2|\Phi><\Sigma_1|\Phi>} \tag{B.3}$$

At this point, it is possible to split the result in two terms coming from direct perturbations on the cross section and other two terms coming from indirect perturbations on the flux:

$$\frac{dR}{R}=\frac{<\Sigma_1|\Delta\Phi>}{<\Sigma_1|\Phi>}+\frac{<\Delta\Sigma_1|\Phi>}{<\Sigma_1|\Phi>}-\frac{<\Sigma_2|\Delta\Phi>}{<\Sigma_2|\Phi>}-\frac{<\Delta\Sigma_2|\Phi>}{<\Sigma_2|\Phi>} \tag{B.4}$$

Finally, by formalizing the perturbations as the response to a relative change in parameter x, the sensitivity coefficient of the reaction rate R is defined:

$$S_x^R=\frac{<\Sigma_1|\frac{\delta\Phi}{\delta x/x}>}{<\Sigma_1|\Phi>}+\frac{<\frac{\delta\Sigma_1}{\delta x/x}|\Phi>}{<\Sigma_1|\Phi>}-\frac{<\Sigma_2|\frac{\delta\Phi}{\delta x/x}>}{<\Sigma_2|\Phi>}-\frac{<\frac{\delta\Sigma_2}{\delta x/x}|\Phi>}{<\Sigma_2|\Phi>} \tag{B.5}$$

The direct terms (2nd and 4th in the above equation) can be estimated by standard detector definition, in fact, when a detector is defined in SERPENT, the filling material can be specified a priori, hence its cross section is flexible. In particular, track length estimators r are introduced to find the interactions with the detectors. Each ℓ_t, that is left by a neutron in the detector cell, is multiplied by the probability of interaction per unit path, which is the cross section itself, to estimate the reaction rate. Then the sum is performed over all tracks of all neutrons in generation α:

$$< \Sigma_1|\Phi >= r[\Sigma_1] = \frac{1}{q}\sum_{n\in\alpha}\sum_{t\in n} w_n \cdot \ell_t\Sigma_1 \tag{B.6}$$

The factor q can be omitted again since it appears in the denominator as well. By differentiating the reaction rate and normalizing the neutron weight w_n:

$$< \Sigma_1|\frac{\delta\Phi}{\delta x/x} >= \sum_{n\in\alpha}\sum_{t\in n} w_n \cdot \frac{\partial w_n/w_n}{\partial x/x} \cdot \ell_t\Sigma_1 \tag{B.7}$$

Finally Eq. 2.87 can be employed to estimate the weight derivative, while this time the sum over generation α is kept in order not to complicate the notation on the neutron tracks:

$$< \Sigma_1|\frac{\delta\Phi}{\delta x/x} >= \sum_{n\in\alpha}\sum_{t\in n} w_n \cdot \left[\sum_{g=(\alpha-\gamma)}^{\alpha} ACC_x^{(n,g)} - REJ_x^{(n,g)}\right] \cdot \ell_t\Sigma_1 \tag{B.8}$$

The indirect term in Eq. B.5 is obtained dividing this term by the estimator of $< \Sigma_1|\Phi >$ from Eq.B.6, and the same is done for the Σ_2 terms. Much like for equation 2.101, the indirect terms can be seen as an average of the net gain rate, but instead of being averaged over the neutron population, they are weighed over the contributions to the track length estimator of the detectors.

$$E_{r[\Sigma_1]}[{}^{(-\lambda)}ACC_x - {}^{(-\lambda)}REJ_x] = \frac{\sum\limits_{n\in\alpha}\sum\limits_{t\in n} w_n \cdot \left[\sum\limits_{g=(\alpha-\lambda)}^{\alpha} ACC_x^{(n,g)} - REJ_x^{(n,g)}\right] \cdot \ell_t\Sigma_1}{\sum\limits_{n\in\alpha}\sum\limits_{t\in n} w_n \cdot \ell_t\Sigma_1} \tag{B.9}$$

In order to compute this, the tally contributions to the detector $< \Sigma_1|\Phi >$ are saved in a buffer, while the same contributions multiplied for the net gain rate in the history of that particle are scored in a second buffer. By dividing one buffer for the other and summing the contributions coming from all detectors and perturbations, the estimator of $E_r[X]$ will yield the indirect contributions to S_x^R. As already mentioned the direct contributions will be recorded in another buffer that employs the estimator in Eq. B.6.

$$S_x^R = E_r[^{(-\lambda)}ACC_x -^{(-\lambda)} REJ_x] + \frac{r\left[\frac{\partial\Sigma_1}{\partial x/x}\right]}{r\left[\Sigma_1\right]} - \frac{r\left[\frac{\partial\Sigma_2}{\partial x/x}\right]}{r\left[\Sigma_2\right]} \tag{B.10}$$

For example, if the perturbed parameter x was to be the integral value of the fission cross section of U-235, and Σ_1 was to be its total cross section, the normalized derivative would be:

$$\frac{\partial\Sigma_{tot}}{\partial\Sigma_f/\Sigma_f} = \frac{\partial(\Sigma_f + \Sigma_a + \Sigma_s)}{\partial\Sigma_f} \cdot \Sigma_f = \Sigma_f \tag{B.11}$$

A detector will be defined filled with the nominal fission cross section material and this term is estimated as $r[\Sigma_f]$.

Bilinear ratios

The content of the previous section is here extended to bilinear functions of the forward and adjoint flux such as kinetics parameters, that are presented in Appendix A, or the void coefficient, that is studied in Appendix B. The response function will have the following form:

$$R = \frac{<\Phi^\dagger|\Sigma_1\Phi>}{<\Phi^\dagger|\Sigma_2\Phi>} \tag{B.12}$$

Following the same procedure that led to Eq. B.5, the sensitivity coefficient of this response function is retrieved:

$$\begin{aligned} S_x^R = & \frac{<\Phi^\dagger|\Sigma_1\frac{\delta\Phi}{\delta x/x}>}{<\Phi^\dagger|\Sigma_1\Phi>} + \frac{<\Phi^\dagger|\frac{\delta\Sigma_1}{\delta x/x}\Phi>}{<\Phi^\dagger|\Sigma_1\Phi>} + \frac{<\frac{\delta\Phi^\dagger}{\delta x/x}|\Sigma_1\Phi>}{<\Phi^\dagger|\Sigma_1\Phi>} + \\ & - \frac{<\Phi^\dagger|\Sigma_2\frac{\delta\Phi}{\delta x/x}>}{<\Phi^\dagger|\Sigma_2\Phi>} - \frac{<\Phi^\dagger|\frac{\delta\Sigma_2}{\delta x/x}\Phi>}{<\Phi^\dagger|\Sigma_2\Phi>} - \frac{<\frac{\delta\Phi^\dagger}{\delta x/x}|\Sigma_2\Phi>}{<\Phi^\dagger|\Sigma_2\Phi>} \end{aligned}$$

This equation presents again two direct terms and four indirect terms from perturbations of the forward and adjoint fluxes. Like in the previous section, an estimator rr for the total importance weighed scoring of the Σ_1 detector is presented:

$$< \Phi^{\dagger}|\Sigma_1\Phi >= rr[\Sigma_1] = \sum_{n\in\alpha}\sum_{t\in n} w_n \cdot \ell_t\Sigma_1 \cdot \frac{1}{w_n}\sum_{n\in d_n^{(\gamma)}} w_k \tag{B.13}$$

Where the adoint flux is estimated with IFP from Eq. 2.88. The direct terms represent the relative contribution of parameter x to this estimator, hence it can be calculated as in the previous section. Concerning the indirect terms, by deriving the forward flux with respect to parameter x it follows:

$$< \Phi^{\dagger}|\Sigma_1\frac{\delta\Phi}{\delta x/x} >= \sum_{n\in\alpha}\sum_{t\in n} \frac{\partial w_n}{\partial x/x} \cdot \ell_t\Sigma_1 \cdot \frac{1}{w_n}\sum_{k\in d_n^{(\gamma)}} w_k \tag{B.14}$$

Instead of employing Eq. 2.87 straightaway to substitute $\frac{\partial w_n}{\partial x/x}$, the other indirect term is presented:

$$< \frac{\delta\Phi^{\dagger}}{\delta x/x}|\Sigma_1\Phi >= \sum_{n\in\alpha}\sum_{t\in n} w_n \cdot \ell_t\Sigma_1 \cdot \left(\frac{1}{w_n}\sum_{k\in d_n^{(\gamma)}}\frac{\partial w_k}{\partial x/x} - \frac{1}{w_n^2}\frac{\partial w_n}{\partial x/x}\sum_{k\in d_n^{(\gamma)}} w_k\right) \tag{B.15}$$

It is clear that by summing Eq. B.14 and B.15, only the derivative on the perturbed weights w_k in generation $\alpha + \gamma$ are left, hence the indirect terms related to the $< \Phi^{\dagger}|\Sigma_1\Phi >$ scoring will simply be:

$$< \frac{\delta\Phi^{\dagger}}{\delta x/x}|\Sigma_1\Phi > + < \Phi^{\dagger}|\Sigma_1\frac{\delta\Phi}{\delta x/x} >= \sum_{n\in\alpha}\sum_{t\in n} \ell_t\Sigma_1 \cdot \sum_{k\in d_n^{(\gamma)}}\frac{\partial w_k}{\partial x/x} \tag{B.16}$$

Once both direct and indirect terms are calculated, the contributions from the numerator of the response function will have a positive sign in the calculation of the sensitivity coefficient, while the contributions from the scoring of the denominator will have a negative sign.

Effective neutron lifetime

In order to show the implementation of the GPT algorithm in SERPENT, the specific case of λ_{eff} is presented in this section. The deterministic definition of the effective neutron lifetime (Appendix A) is:

$$\lambda_{eff} = \frac{< \Phi^\dagger | \frac{1}{v} \Phi >}{< \Phi^\dagger | \hat{F} \Phi >} \tag{B.17}$$

From the discussion of the previous section, the estimator of the numerator follows from equation B.13:

$$< \Phi^\dagger | \frac{1}{v} \Phi >= \sum_{n \in \alpha} \sum_{t \in n} \ell_t \frac{1}{v} \cdot \sum_{n \in d_n^{(\gamma)}} w_k \tag{B.18}$$

Introducing $\tau_k^{-(\gamma)} = \sum_t \ell_t \frac{1}{v}$ as the total length of the ancestor tracks divided by its speed, an estimator for the lifetime of the γ_{th} ancestor of the neutrons in generation $(\alpha + \gamma)$ can be substituted in the previous equation:

$$< \Phi^\dagger | \frac{1}{v} \Phi >= \sum_{k \in (\alpha+\gamma)} w_k \cdot \tau_k^{(-\gamma)} \tag{B.19}$$

The perturbation of this term only yields indirect contributions since no parameter manipulation would cause a direct effect on the neutrons speed. Employing equation B.16 with τ_k and shifting the sum on daughter k neutrons in generation $(\alpha + \gamma)$:

$$< \frac{\delta \Phi^\dagger}{\delta x / x} | \frac{1}{v} \Phi > + < \Phi^\dagger | \frac{1}{v} \frac{\delta \Phi}{\delta x / x} >= \sum_{k \in (\alpha+\gamma)} w_k \cdot \frac{\partial w_k}{\partial x / x} \cdot \tau_k^{(-\gamma)} \tag{B.20}$$

Now equation 2.87 can be employed to estimate the weight derivative, bearing in mind that γ is the number of latent generations that were employed to estimate the adjoint flux with IFP, while λ is the number that is chosen to compute the net gain rate in the actual GPT part of the algorithm:

$$\frac{< \frac{\delta\Phi^\dagger}{\delta x/x}|\frac{1}{v}\Phi >}{< \Phi^\dagger|\frac{1}{v}\Phi >} + \frac{< \Phi^\dagger|\frac{1}{v}\frac{\delta\Phi}{\delta x/x} >}{< \Phi^\dagger|\frac{1}{v}\Phi >} = \frac{\sum\limits_{k\in(\alpha+\gamma)} w_k \cdot \left[\sum\limits_{g=(\alpha-\lambda)}^{(\alpha+\gamma)} ACC_x^{(n,g)} - REJ_x^{(n,g)}\right] \cdot \tau_k^{(-\gamma)}}{\sum\limits_{k\in(\alpha+\gamma)} w_k \cdot \tau_k^{(-\gamma)}} \tag{B.21}$$

This reminds the result obtained in Eq. B.9, where the track-length estimator r is now also weighed over the adjoint (rr from Eq. B.13) and here has more the shape of a life-length estimator. In this case though, $E_{rr}[X]$ will not be computed by the algorithm since further developments come from the denominator of λ_{eff}. Instead, both numerator and denominator are multiplied by the neutron population at generation $\alpha + \gamma$, yielding the average of the product between the net gain rate and the neutron lifetimes:

$$\frac{\sum\limits_{k\in(\alpha+\gamma)} w_k \cdot \left[ACC_x^{(n,-\epsilon)} - REJ_x^{(n,-\epsilon)}\right] \cdot \tau_k^{(-\gamma)}}{\sum\limits_{k\in(\alpha+\gamma)} w_k \cdot \tau_k^{(-\gamma)}} \cdot \frac{\sum\limits_{k\in(\alpha+\gamma)} w_k}{\sum\limits_{k\in(\alpha+\gamma)} w_k} =$$

$$= \frac{E\left[ACC_x^{(n,-\epsilon)} - REJ_x^{(n,-\epsilon)} \cdot \tau^{(-\gamma)}\right]}{E[\tau^{(-\gamma)}]}$$

In the denominator case, it is useful to group the direct term with the two indirect terms allowing for the switch between integral and derivative:

$$< \frac{\delta\Phi^\dagger}{\delta x/x}|\hat{F}\Phi > + < \Phi^\dagger|\frac{1}{k}\frac{\delta\hat{F}}{\delta x/x}\Phi > + < \Phi^\dagger|\hat{F}\frac{\delta\Phi}{\delta x/x} >= \frac{\delta}{\frac{\delta x}{x}} < \Phi^\dagger|\hat{F}\Phi > \tag{B.22}$$

In fact, the estimator of the term $< \Phi^\dagger|\hat{F}\Phi >$ is merely the neutron population at generation α [18]. Because of this simple result, it is useful to employ Eq. 2.87 on the total denominator term:

$$\frac{\frac{\delta}{\frac{\delta x}{x}} < \Phi^\dagger|\hat{F}\Phi >}{< \Phi^\dagger|\hat{F}\Phi >} = \frac{\sum\limits_{k\in(\alpha+\gamma)} w_k \cdot \left[ACC_x^{(n,-\epsilon)} - REJ_x^{(n,-\epsilon)}\right]}{\sum\limits_{k\in(\alpha+\gamma)} w_k} \tag{B.23}$$

This is clearly the expected value of the net gain rate, hence the sensitivity coefficient of the delayed neutron fraction can be written employing the expected values by adding the contributions coming from the numerator and subtracting the ones from the denominator:

$$S_x^\lambda = \frac{E\left[\sum\limits_{history} ACC_x - REJ_x \cdot \tau^{(-\gamma)}\right]}{E[\tau^{(-\gamma)}]} - E\left[\sum_{history} ACC_x - REJ_x\right] \tag{B.24}$$

Two buffers will be needed to compute this sensitivity, one that performs the average of the net gain rate over the history estimating the second term (it is the same that appears also in other parameters perturbations). While the first term will need an other buffer to perform the multiplication between the gain rate and the lifetime for each neutron history. The value $E[\tau^{(-\gamma)}]$ is automatically calculated by the IFP routine as discussed in section 2.3.2. This particular formulation of S_x^λ highlights the definition of the covariance of two variables: $COV[X,Y] = E[X \cdot Y] - E[X] \cdot E[Y]$. It follows that:

$$S_x^\lambda = \frac{COV\left[\sum\limits_{history} (ACC_x - REJ_x)\,, \quad \tau^{(-\gamma)}\right]}{E[\tau^{(-\gamma)}]} \tag{B.25}$$

In fact, for any response function $R = \frac{E[e_1]}{E[e_2}]$ comprising quantities that can be expressed as the expected value of a Monte Carlo estimator e (in the same way $E[\tau^{-(\gamma)})]$ is an unbiased IFP estimator of λ_{eff}) the following equation holds:

$$S_x^R = \frac{COV\left[\sum\limits_{history} ACC_x - REJ_x, \quad e_1\right]}{E[e_1]} - \frac{COV\left[\sum\limits_{history} ACC_x - REJ_x, \quad e_2\right]}{E[e_2]} \tag{B.26}$$

This powerful result allows for the estimation of sensitivity coefficients in the same criticality calculation without running any extra neutron cycle, making the implementation of sensitivity analysis in the code SERPENT [2] very competitive with respect to other codes. While the convergence of these sensitivities is extremely fast for total cross-section perturbations (i.e. number densities), multi-group sensitivities can show a much slower convergence, especially for low scoring reactions or small target volumes.

Bibliography

[1] A. Gandini, "A generalized perturbation method for bi-linear functionals of the real and adjoint neutron fluxes," *Journal of Nuclear Energy*, vol. 21, pp. 755–765, Oct. 1967.

[2] M. Aufiero, A. Bidaud, M. Hursin, J. Leppanen, G. Palmiotti, S. Pelloni, and P. Rubiolo, "A collision history-based approach to sensitivity/perturbation calculations in the continuous energy Monte Carlo code SERPENT," *Annals of Nuclear Energy*, vol. 85, pp. 245–258, Nov. 2015.

[3] M. L. Williams, "Development of depletion perturbation theory for coupled neutron/nuclide fields," *Nuclear Science and Engineering*, vol. 70, no. 1, pp. 20–36, 1979.

[4] T. Takeda and T. Umano, "Burnup sensitivity analysis in a fast breeder reactor—part i: Sensitivity calculation method with generalized perturbation theory," *Nuclear Science and Engineering*, vol. 91, no. 1, pp. 1–10, 1985.

[5] Y. Calzavara, S. Fuard, and A. Bergeron, "Evaluation of measurements performed on the French high flux reactor (HFR)," *International Reactor Physics Benchmark Experiments Project*, pp. 20–24, 2008.

[6] J. de Troullioud de Lanversin, M. Kütt, and A. Glaser, "Onix: An open-source depletion code," *Annals of Nuclear Energy*, vol. 151, p. 107903, 2021.

[7] G. R. R. Martin, "A song of ice and fire: A clash of kings," 1998.

[8] C. J. Roy and W. L. Oberkampf, “A comprehensive framework for verification, validation, and uncertainty quantification in scientific computing,” *Computer Methods in Applied Mechanics and Engineering*, vol. 200, no. 25, pp. 2131–2144, 2011.

[9] D. C. Cox and P. Baybutt, “Methods for uncertainty analysis: A comparative survey,” *Risk Analysis*, vol. 1, no. 4, pp. 251–258, 1981.

[10] B. A. Worley, “Deterministic uncertainty analysis,” 12 1987.

[11] J. Kučera, P. Bode, and V. Stvpánek, “The 1993 iso guide to the expression of uncertainty in measurement applied to naa,” *Journal of Radioanalytical and Nuclear Chemistry*, vol. 245, pp. 115–122, 07 2000.

[12] R. L. Iman and J. C. Helton, “An investigation of uncertainty and sensitivity analysis techniques for computer models,” *Risk Analysis*, vol. 8, no. 1, pp. 71–90, 1988.

[13] C. M. Perfetti and B. T. Rearden, “Development of a generalized perturbation theory method for sensitivity analysis using continuous-energy monte carlo methods,” *Nuclear Science and Engineering*, vol. 182, no. 3, pp. 354–368, 2016.

[14] J. A. Favorite, “Adjoint-based sensitivity analysis and uncertainty quantification for keff: Using the mcnp ksen card,” 8 2018.

[15] H. Brooks, “Perturbation theory for boltzmann equation,” 2 1950.

[16] G. Palmiotti and M. Salvatores, “Developments in sensitivity methodologies and the validation of reactor physics calculations,” *Science and Technology of Nuclear Installations*, vol. 2012, 01 2012.

[17] A. Gandini, G. Palmiotti, and M. Salvatores, “Equivalent generalized perturbation theory (EGPT),” *Annals of Nuclear Energy*, vol. 13, pp. 109–114, Jan. 1986.

[18] B. C. Kiedrowski and F. B. Brown, "Adjoint-Based k-Eigenvalue Sensitivity Coefficients to Nuclear Data Using Continuous-Energy Monte Carlo," *Nuclear Science and Engineering*, vol. 174, no. 3, pp. 227–244, 2013.

[19] B. C. Kiedrowski, "Review of early 21st-century monte carlo perturbation and sensitivity techniques for k-eigenvalue radiation transport calculations," *Nuclear Science and Engineering*, vol. 185, no. 3, pp. 426–444, 2017.

[20] J. Leppanen, M. Aufiero, E. Fridman, R. Rachamin, and S. van der Marck, "Calculation of effective point kinetics parameters in the Serpent 2 Monte Carlo code," *Annals of Nuclear Energy*, vol. 65, pp. 272–279, Mar. 2014.

[21] M. Aufiero and M. Fratoni, "A new approach to the stabilization and convergence acceleration in coupled monte carlo–cfd calculations: The newton method via monte carlo perturbation theory," *Nuclear Engineering and Technology*, vol. 49, no. 6, pp. 1181 – 1188, 2017. Special Issue on International Conference on Mathematics and Computational Methods Applied to Nuclear Science and Engineering 2017 (M&C 2017).

[22] D. Kotlyar, M. Aufiero, E. Shwageraus, and M. Fratoni, "A perturbation-based substep method for coupled depletion monte-carlo codes," *Annals of Nuclear Energy*, vol. 102, pp. 236–244, 04 2017.

[23] A. Bidaud, x. doligez, P. Olbratowski, E. Autino, M. Aufiero, B. Leniau, O. Meplan, and S. David, "Understanding total monte carlo uncertainty propagation in burn up calculations with generalized perturbation theory," *The European Physical Journal Conferences*, 09 2016.

[24] E. Greenspan, M. L. Williams, and J. H. Marable, "Time-dependent generalized perturbation theory for coupled neutron-nuclide problems," *Nuclear Science and Engineering*, vol. 73, no. 2, pp. 210–218, 1980.

[25] T. Kamei, T. Yoshida, T. Takeda, and T. Umano, “Burnup sensitivity analysis in a fast breeder reactor—part ii: Prediction accuracy of burnup characteristics,” *Nuclear Science and Engineering*, vol. 91, no. 1, pp. 11–33, 1985.

[26] D. Portinari, M. Aufiero, Y. Calzavara, A. Cammi, S. Lorenzi, and A. Bidaud, “Uncertainty and sensitivity analysis of safety parameters for high flux reactor at institut laue-langevin,” *The International Conference on Mathematics and Computational Methods applied to Nuclear Science and Engineering (M&C 2019)*, 2019.

[27] B. Iooss and P. Lemaître, “A review on global sensitivity analysis methods,” in *Uncertainty management in Simulation-Optimization of Complex Systems: Algorithms and Applications* (C. Meloni and G. Dellino, eds.), Springer, 2015.

[28] A. Gandini, “Time-dependent generalized perturbation methods for burn-up analysis,” Tech. Rep. CNEN-RT/FI–75-4, Comitato Nazionale per l’Energia Nucleare, 1975.

[29] D. Portinari, Y. Calzavara, and A. Bidaud, “A 0.5 dimensional model for lwr fuel pin sensitivity analysis with depletion perturbation theory,” *International Conference on Physics of Reactors (PHYSOR 2022)*, 2022.

[30] O. Leray, D. Rochman, P. Grimm, H. Ferroukhi, A. Vasiliev, M. Hursin, G. Perret, and A. Pautz, “Nuclear data uncertainty propagation on spent fuel nuclide compositions,” *Annals of Nuclear Energy*, vol. 94, pp. 603–611, 2016.

[31] K. C. Bledsoe, J. Hite, M. A. Jessee, and J. P. Lefebvre, “Application of markov chain monte carlo methods for uncertainty quantification in inverse transport problems,” *IEEE Transactions on Nuclear Science*, vol. 68, no. 8, pp. 2210–2219, 2021.

[32] W. ZWERMANN, A. AURES, L. GALLNER, V. HANNSTEIN, B. KRZYKACZ-HAUSMANN, K. VELKOV, and J. MARTINEZ, "Nuclear data uncertainty and sensitivity analysis with xsusa for fuel assembly depletion calculations," *Nuclear Engineering and Technology*, vol. 46, no. 3, pp. 343–352, 2014.

[33] M. L. Williams, *Perturbation Theory for Nuclear Reactor Analysis.* Y. RONEN. Ed., CRC Press, Boca Raton, Florida , 1985.

[34] G. I. Bell and S. Glasstone, "Nuclear reactor theory," 10 1970.

[35] D. R. Smith, *Variational methods in optimization.* Mineola (N.Y.): Dover, 1998.

[36] K.-Y. LIANG and S. L. ZEGER, "Longitudinal data analysis using generalized linear models," *Biometrika*, vol. 73, no. 1, pp. 13–22, 1986.

[37] I. Lux and L. Koblinger, *Monte Carlo particle transport methods: neutron and photon calculations.* Boca Raton, FL: CRC Press, 1991.

[38] L. Morgan and D. Kotlyar, "Weighted-delta-tracking for monte carlo particle transport," *Annals of Nuclear Energy*, vol. 85, pp. 1184 – 1188, 2015.

[39] Y. Nauchi and T. KAMEYAMA, "Development of calculation technique for iterated fission probability and reactor kinetic parameters using continuous-energy monte carlo method," *Journal of Nuclear Science and Technology*, vol. 47, pp. 977–990, 01 2012.

[40] M. AUFIERO, "Development of advanced simulation tools for circulating fuel nuclear reactors," Mar. 2014.

[41] K. Scharmer and H. G. Eckert, "FOEHN: The critical experiment for the Franco-German High Flux Reactor," Tech. Rep. ORNL/TR–91/23, Oak Ridge National Lab., 1991.

[42] R. SANCHEZ, G. DANTE, and I. ZMIJAREVIC, "Diffusion piecewise homogenization via flux discontinuity ratios," *Nuclear Engineering and Technology*, vol. 45, no. 6, pp. 707–720, 2013.

[43] J. A. Rathkopf and W. R. Martin, "The finite element response matrix method for the solution of the neutron transport equation," *Progress in Nuclear Energy*, vol. 18, pp. 237–250, 1986.

[44] G. I. Bell and S. Glasstone, "Nuclear reactor theory," 10 1970.

[45] R. Sanchez and N. J. McCormick, "A review of neutron transport approximations," *Nuclear Science and Engineering*, vol. 80, no. 4, pp. 481–535, 1982.

[46] A. E. Johnson, D. Kotlyar, S. Terlizzi, and G. Ridley, "serpenttools: A python package for expediting analysis with serpent," *Nuclear Science and Engineering*, vol. 194, no. 11, pp. 1016–1024, 2020.

[47] Y. Calzavara, "Etude neutronique," *Rapport RHF 447*, 2013.

[48] H. Wanner, M. A. E. Östhols, and L. S. st. Germain, "Guidelines for the assignment of uncertainties," 1999.

[49] S. Valance, B. Baumeister, W. Pertry, and J. Höglund, "Innovative and safe supply of fuels for reactors," *EPJ Nuclear Sciences and Technologies*, vol. 6, p. 40, 01 2020.

[50] W. Haeck, B. Cochet, F. Bernard, and A. Tymen, "Experimental validation of vesta 2.1," 10 2013.

[51] C. Reiter, H. Breitkreutz, A. Röhrmoser, A. Seubert, and W. Pertry, "Neutronic simulations for the frm ii," *Annals of Nuclear Energy*, vol. 131, pp. 1–8, 06 2019.

[52] M. L. Williams and C. R. Weisbin, "Sensitivity and uncertainty analysis for functionals of the time-dependent nuclide density field. [origen-a]," 07 2019.